Title
INFRARED OPTICAL PROPERTIES OF THE QUASI-ONE-DIMENSIONAL CONDUCTORS NbSe3 AND (TMTSF)2Cl04

Author
Challener, W.A.

Publication Date
1983-08-01

LBL-16186

c-2

Lawrence Berkeley Laboratory

UNIVERSITY OF CALIFORNIA

Materials & Molecular Research Division

INFRARED OPTICAL PROPERTIES OF THE QUASI-ONE-DIMENSIONAL CONDUCTORS $NbSe_3$ AND $(TMTSF)_2ClO_4$

W.A. Challener IV
(Ph.D. Thesis)

August 1983

Prepared for the U.S. Department of Energy under Contract DE-AC03-76SF00098

LBL-16186
c-2

DISCLAIMER

LBL-16186

INFRARED OPTICAL PROPERTIES OF THE QUASI-ONE-DIMENSIONAL CONDUCTORS $NbSe_3$ AND $(TMTSF)_2ClO_4$

William Albert Challener IV
(Ph.D. Thesis)

Department of Physics
University of California, Berkeley
and
Materials and Molecular Research Division
Lawrence Berkeley Laboratory
Berkeley, California 94720

August 1983

This work was supported, in part, by the Director, Office of Energy Research, Office of Basic Energy Sciences, Materials Sciences Division of the U.S. Department of Energy under Contract Number DE-AC03-76SF00098 and by a graduate fellowship from the National Science Foundation.

To my mother and father,

whose love and support throughout my life

have made this possible.

Table of Contents

List of Figures

List of Tables

INFRARED OPTICAL PROPERTIES OF THE QUASI-ONE-DIMENSIONAL CONDUCTORS $NbSe_3$ AND $(TMTSF)_2ClO_4$

William Albert Challener IV

Department of Physics, University of California, Berkeley
and Materials and Molecular Research Division,
Lawrence Berkeley Laboratory
Berkeley, California 94720

ABSTRACT

The technique of far infrared Fourier transform spectroscopy has been used to study the properties of two materials, $NbSe_3$ and $(TMTSF)_2ClO_4$. These compounds are members of a novel class of materials called quasi-one-dimensional conductors. $NbSe_3$ undergoes incommensurate charge density wave (CDW) transitions and exhibits electrical transport by sliding CDW's. $(TMTSF)_2ClO_4$ undergoes order-disorder, spin density wave, and superconducting transitions at ambient pressure. It is a member of the first class of organic materials to be synthesized which exhibit superconductivity.

We have done a Kramers-Kronig analysis of the far infrared reflectance of $NbSe_3$ to obtain an estimate of the optical constants. We have used models of the frequency dependent conductivity to fit the data. General arguments show that at 2K a CDW energy gap exists between 120 and 190 cm^{-1}, the relaxation time(s) of the free carriers and CDW pinned mode is $>3 \times 10^{-12}$s, and the ratio of the free carrier

concentration to band mass is $<2 \times 10^{20}$ cm^{-3}/m_o. The strength of the pinned mode obtained from the detailed fit is inconsistent with the classical model of CDW transport.

We have also measured the far infrared reflectance of $(TMTSF)_2ClO_4$ and performed a Kramers-Kronig analysis to obtain the optical constants. A large peak in the conductivity occurs above 100 cm^{-1}, and a smaller peak occurs at ~25 cm^{-1}. We have no explanation at present for the large peak, but we believe that the small peak is a phase phonon. It occurs when the orientations of the ClO_4 anions order and thereby induce a charge density wave in the lattice. Our measurements of the temperature dependence, the effect of radiation damage, and the magnetic field dependence of this feature are in agreement with this conclusion. Our data, however, are inconsistent with an interpretation based upon a theory of quasi-one-dimensional fluctuational superconductivity.

I. Introduction

Quasi-one-dimensional conductors are materials which have one crystal axis of high conductivity and two axes of lower conductivity. The degree of anisotropy can be as large as 10^5. The optical properties of these materials are also anisotropic. Usually the highly conducting axis gives rise to a plasma edge in the near infrared for light polarized in this direction. The reflectance for light polarized perpendicular to the highly conducting axis, though, is usually very low (<20%) in the infrared with no evidence of a plasma edge. The quasi-one-dimensional nature of these materials is also evidenced by the manner in which they crystallize, which is typically in the form of long, narrow fibers, with the fiber axis being the axis of highest conductivity. These materials exhibit many novel physical properties not usually encountered in materials of higher effective dimensionality.

There are various microscopic definitions of quasi-one-dimensionality. Materials in which a large fraction of the Fermi surface is nested (i.e. in which a finite fraction of the Fermi surface can be spanned by a single k-vector) are quasi-one-dimensional. Nested Fermi surfaces in these materials often drive charge density wave (CDW) and spin density wave (SDW) transitions at low temperatures. This will be discussed in more detail in Chapter III.

Another (and not necessarily equivalent) definition of quasi-one-dimensionality is based upon the nature of the transverse electrical transport. At high temperatures, the carriers on a conducting chain

in the crystal will tend to be thermally scattered before they can jump to a neighboring chain, and therefore they are thermally localized to a single chain. At lower temperatures the thermal scattering decreases and the frequency for interchain transfer of the carriers will become larger than the scattering frequency of the carriers on a single chain. At this point the transverse electrical transport will become coherent rather than diffusive, and the material will exhibit a higher effective dimensionality. The crossover temperature is defined[1] by the relation $\hbar/\tau = t_\perp$, where τ is the scattering time of the carriers on a single chain, and $t_\perp$ is the interchain transfer integral.

A third definition concerns the significance of fluctuation effects. Fluctuations prevent long range order and hence any phase transitions in a strictly one-dimensional system. As the temperature decreases, however, the coherence length of the fluctuations in the order parameter grows and the system begins to exhibit characteristics of an ordered phase. In real materials, when the coherence length becomes large, three-dimensional ordering will occur, suppressing the fluctuations and giving rise to a real phase transition.[2]

Fluctuation effects will be significant in a quasi-one-dimensional conductor if the energy coupling correlated regions on separate chains is less than the thermal energy.[1] The total interchain coupling energy is given by the product of the coherence length for intrachain correlations, ξ, and the interchain coupling energy per unit length, $J_\perp$. For a unit cell of chain lattice constant d with z neighboring chains, fluctuations should be significant if $k_B T > z\xi J_\perp/d$. Below

this temperature, the fluctuations should be negligible. The relationship between flucutations and superconductivity in quasi-one-dimensional conductors will be discussed in more detail in Chapter VI.

Many of the transition metal trichalcogenides are quasi-one-dimensional compounds. $NbSe_3$, the most important member of this group, is generally considered to be the prototype of charge density wave systems. It is the first material known to exhibit electrical transport by sliding CDW's. Part of the research reported in this thesis concerns the infrared optical properties of this compound.

The organic charge transfer salts form a second class of quasi-one-dimensional materials. These compounds exhibit CDW, SDW, superconducting, and order-disorder transitions. The $(TMTSF)_2X$ compounds are the first organic compounds to exhibit superconducting transitions. The "X" in the chemical formula represents an inorganic anion. $(TMTSF)_2ClO_4$ is of particular interest because it undergoes a superconducting transition at ambient pressure (with a $T_c \sim 1K$). Part of the research reported in this thesis involves the infrared optical properties of this compound.

References

1. P. M. Chaikin, M.-Y. Choi, R. L. Greene, to be published in Les Editions de Physique (1983).

2. P A. Lee, T. M. Rice, P. W. Anderson, Phys. Rev. Lett. 31 No. 7, 462 (1973).

II. Apparatus

Our infrared measurements are made with a conventional step-and-integrate Fourier transform spectrometer with mylar beamsplitters.[1] Several pieces of apparatus were constructed or modified for making reflectance and transmittance measurements as a function of temperature and applied magnetic field. A diagram of the apparatus used for measuring sample transmittance as a function of temperature is shown in Fig. 1. The apparatus is immersed in a pumped liquid helium bath, and the radiation from the spectrometer enters the sample chamber through a polished brass light pipe. A sample wheel on a rotatable shaft is located inside the sample chamber. The shaft is made of nylon to minimize the thermal conductance, and it may be manually rotated at the top of the apparatus at room temperature to change samples. The sample wheel has locations for six different samples. One space is usually left vacant to measure the instrumental spectrum for normalization of the data.

The electrical leads for regulation of the sample temperature enter the sample chamber through a thin-walled stainless steel tube, and are soldered to heat sinks on the inner wall of the sample chamber. A carbon resistor, calibrated against a Lakeshore Cryotronics germanium thermometer, is used as the sample thermometer. The leads to the carbon resistor thermometer are of manganin wire to minimize the thermal conductivity. A carbon resistor or a length of manganin wire is used as the heater. The leads to the heater are of copper wire to minimize the electrical resistivity and provide maximum power

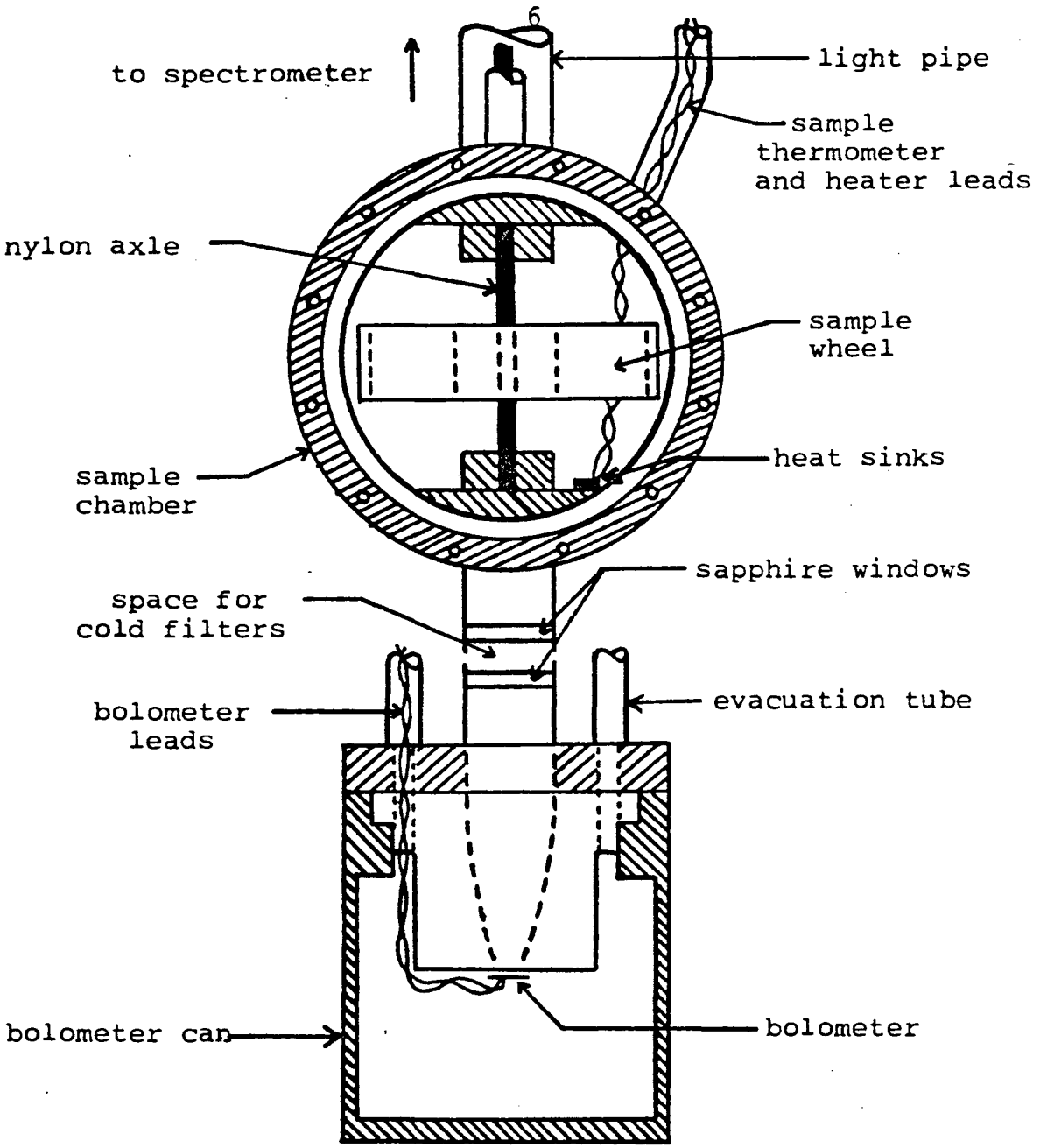

Fig. 1. Apparatus for transmittance measurements.

dissipation in the heater rather than in the leads. Both the thermometer and heater are heat sunk to the sample wheel with thermal heat sinking compound or varnish. Sample temperatures below 2K are obtained by introducing helium exchange gas into the sample chamber, thereby heat sinking the sample to the bath temperature. With the sample chamber evacuated, sample temperatures of over 100K can be obtained before radiation loading of the bolometer begins to seriously reduce its responsivity.

The radiation which is transmitted through the sample exits from the sample chamber through a sapphire window, passing into a space where filters can be kept cold through contact with the liquid helium, and then through another sapphire window into the bolometer can.

Transmittance measurements as a function of magnetic field could be made using the apparatus[2] shown in Fig. 2. This apparatus was modified slightly to include a composite bolometer.[3] The bolometer can was also modified to have an indium o-ring seal rather than a Wood's metal seal.

Reflectance measurements could be made as a function of temperature with the apparatus shown in Fig. 3. The light is incident upon the sample at 11° from the normal. The sample wheel has three locations for samples, one of which usually contains a brass mirror for normalization of the instrumental spectrum. The temperature of the sample is regulated by means of a carbon resistor thermometer and heater, as described previously.

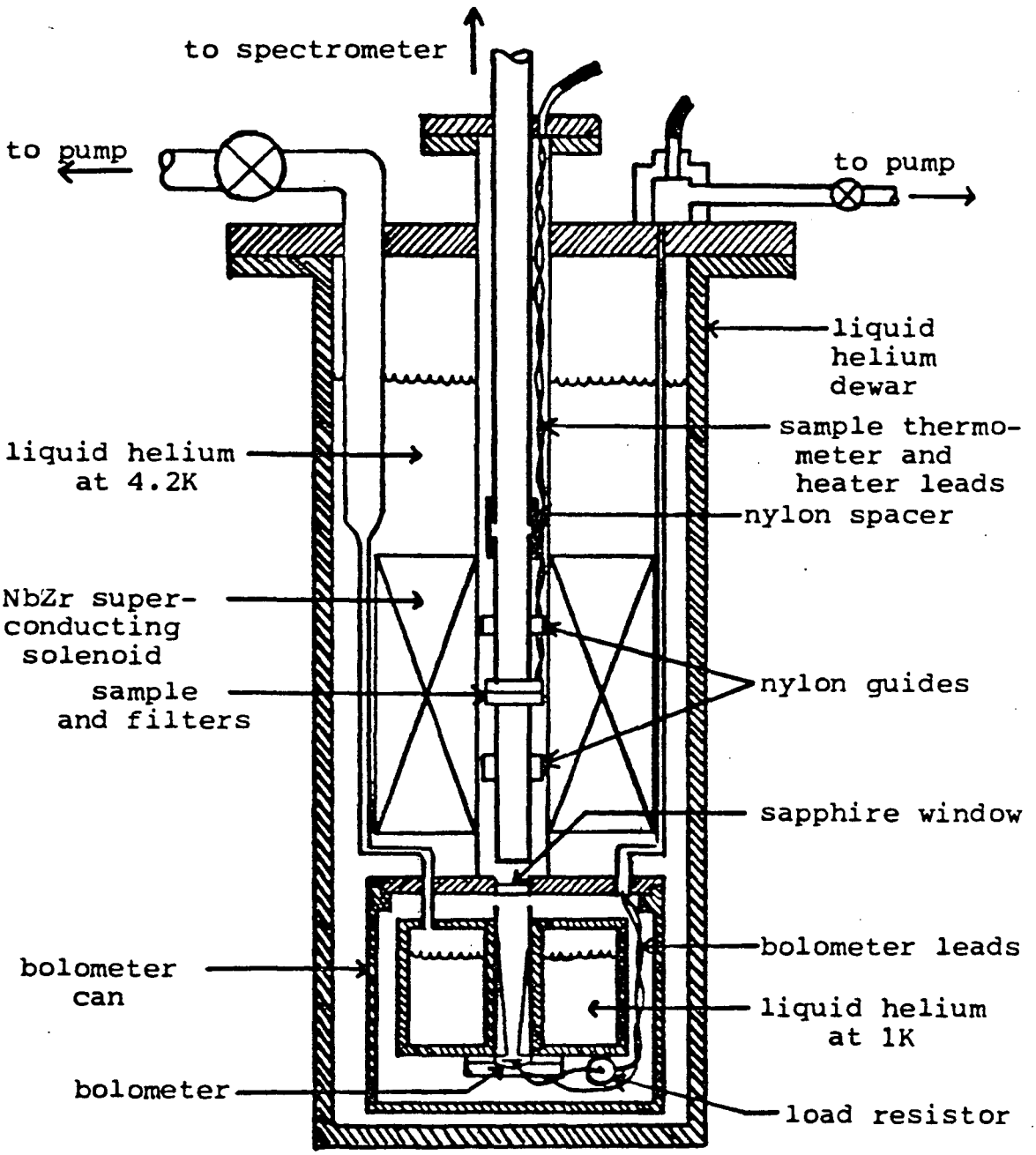

Fig. 2. Apparatus for magnetic field measurements.

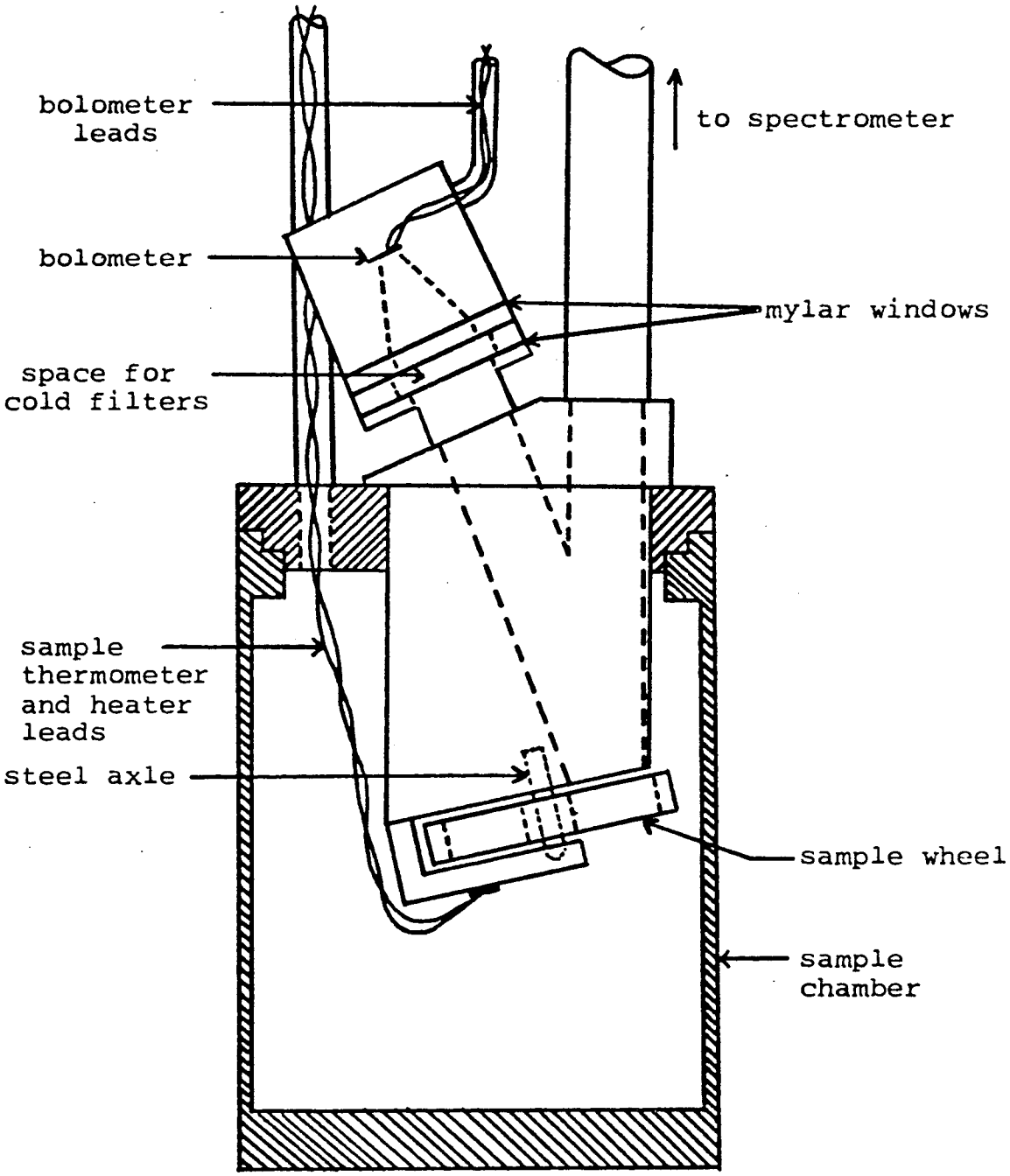

Fig. 3. Apparatus for reflectance measurements.

We use high background, composite doped-germanium bolometers[3] operated at 1.2K for infrared measurements. They have a dark electrical noise equivalent power of $\sim 10^{-14}$ $W/\sqrt{Hz}$.

A PDP 11/20 minicomputer operates the spectrometer, collects and stores the data, and performs all the data analysis. The computer is interfaced to the output of the bolometer through a lock-in amplifier and an analog-to-digital converter.

References

1. R. L. Aurbach, Ph.D. Thesis, U.C. Berkeley, 1975.

2. R.R. Joyce, P.L. Richards, Phys. Rev. 179, 375 (1969).

3. A.E. Lange, E. Kreysa, S.E. McBride, P.L. Richards, E.E. Haller, submitted to Int'l. J. Infrared Millimeter Waves.

III. Charge density waves

The charge density wave state was originally discussed by Peierls[1] and Fröhlich[2] for an idealized one-dimensional metal. The electronic energy band diagram for a one-dimensional metal at absolute zero is shown in Fig. 4. This energy band diagram, however, does not represent the ground state of the metal for this idealized example. A periodic distortion of the lattice with a wavelength of π/k_F and a wavevector of $2k_F$ will connect electronic states at $\pm k_F$ on opposite sides of the Fermi surface. Such a distortion creates new stationary states at the Fermi wavevector, and a gap is opened in the electronic density of states at the Fermi energy. This is shown in Fig. 5. At absolute zero, this periodic distortion causes filled electronic states to be lowered in energy, and empty electronic states to be raised in energy. There is a net lowering of the total electronic energy. The energy gained by opening the gap at the Fermi surface more than compensates for the energy required to strain the lattice to create the periodic structural distortion, and so at absolute zero the distorted state is the ground state. Many, but not all, of the real quasi-one-dimensional conductors evidence such a structural distortion at low temperatures.

The periodic distortion of the lattice creates a periodic density of positive charge from the lattice ions. The electronic charge density rearranges itself to maintain charge neutrality, and thus the electronic charge density acquires the periodicity of the structural distortion. This is the origin of the charge density wave.

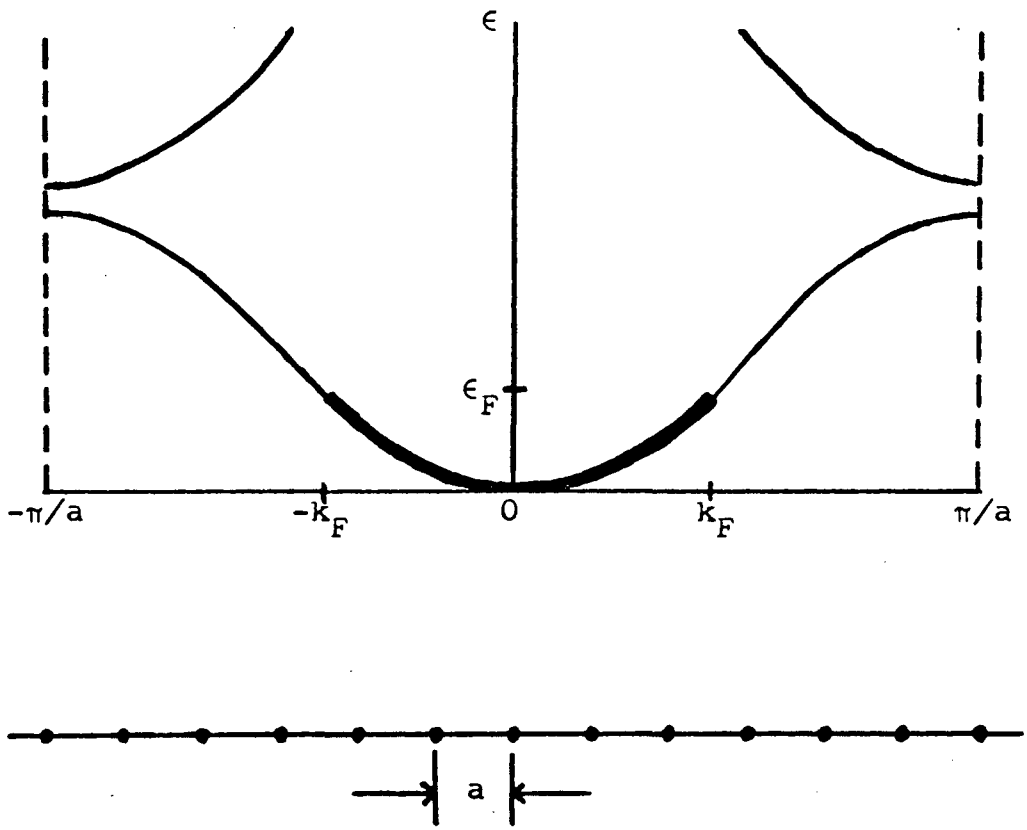

Fig. 4. Electronic energy band diagram and lattice for an undistorted one-dimensional metal at absolute zero.

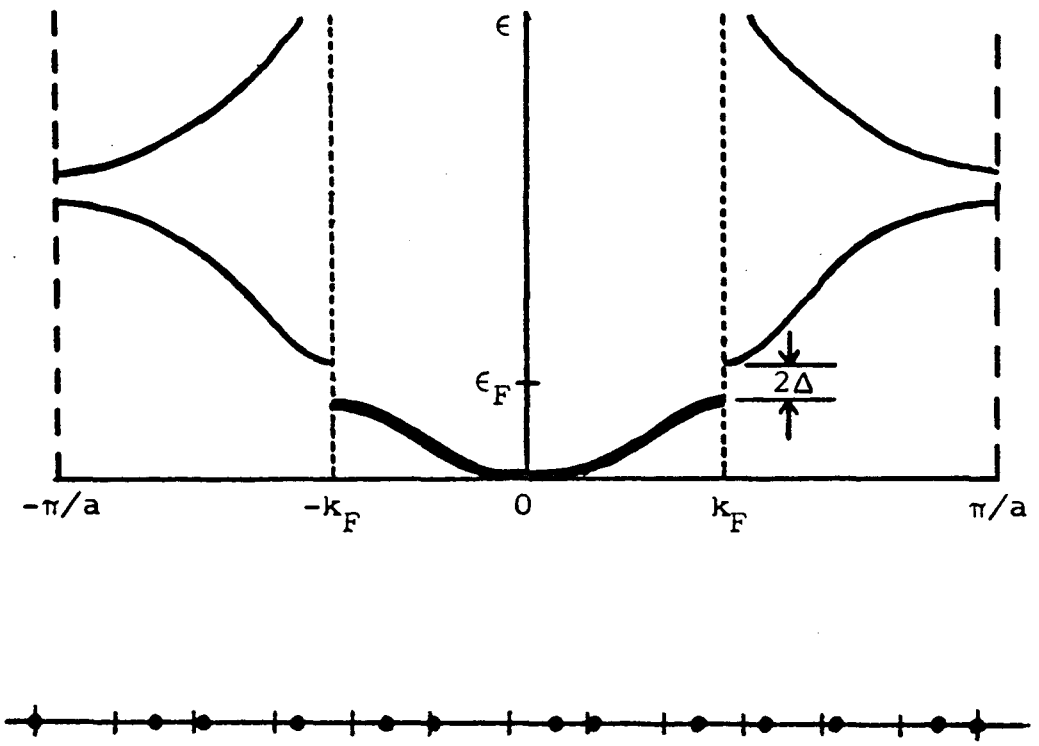

Fig. 5. Electronic energy band diagram and lattice for a one-dimensional solid in the charge density wave state at absolute zero.

The periodic structural distortion is a superlattice imposed upon the undistorted lattice. As such it can be directly measured by various diffraction and scattering techniques (x-ray, electron, or neutron) which measure either the electronic charge density or the positions of the lattice ions. Because the wavelength of the superlattice distortion is determined by the Fermi wavevector, it may or may not be related to the lattice periodicity. The CDW is commensurate with the lattice if the wavelength of the CDW satisfies the equation $m \cdot \lambda = n \cdot a$, where m and n are integers, and a is the lattice constant. In this case, the CDW sits in the periodic potential well of the lattice as well as that of the superlattice. If m and n are small integers then the position or phase of the CDW is strongly pinned to the lattice. Large values of m and n correspond to a much weaker pinning energy, as the CDW approaches incommensurability with the lattice.

The CDW may also be incommensurate with the lattice. In this case, the coupled CDW-lattice distortion is translationally invariant with respect to the lattice, and its phase is not pinned by the lattice potential. If the CDW is not pinned to the lattice, then in the jellium model considered by Fröhlich[2] it can be accelerated through the lattice with an infinitesimal applied electric field, and thus carry a supercurrent. The presence of the energy gap at the Fermi surface, as in real superconductors, prevents the creation of low energy excitations by the moving CDW, and so the CDW slides without friction, dragging the periodic lattice distortion along with it.

However, no real materials exhibit CDW superconductivity. The finite lifetime of the sliding lattice distortion is one effect which prevents infinite conductivity.[3] In addition, in all real materials the CDW's are pinned to the lattice either through commensurability with the lattice or by the presence of impurities. The CDW's can be depinned from the lattice by the application of a sufficiently large electric field, at least in some CDW materials like $NbSe_3$, but the depinned CDW's experience frictional forces and do not enhance the dc conductivity over what would be expected if the condensed carriers were instead in their normal state.

The dispersion of the acoustic phonon in the distorted and undistorted states is shown in Fig. 6. At temperatures well above the CDW transition temperature, the acoustic phonon branch is determined primarily by the dispersion of the lattice ions in the absence of any interaction with the conduction electrons. As the transition temperature is approached, however, the $\pm 2k_F$ phonons begin to soften due to their interaction with the electrons at the Fermi surface. At the transition temperature, the frequency of the $\pm 2k_F$ phonons goes to zero and hence the restoring force for longitudinal displacements of the lattice ions along the chain with wavelength π/k_F is zero. The $+2k_F$ phonon and the $-2k_F$ phonon are mixed together by the electronic interaction, both being folded back to the Brillouin zone center. As the temperature is cooled below the transition temperature, the periodic structural distortion locks in and begins to grow in amplitude. The mixed $\pm 2k_F$ phonons which are coupled to the CDW

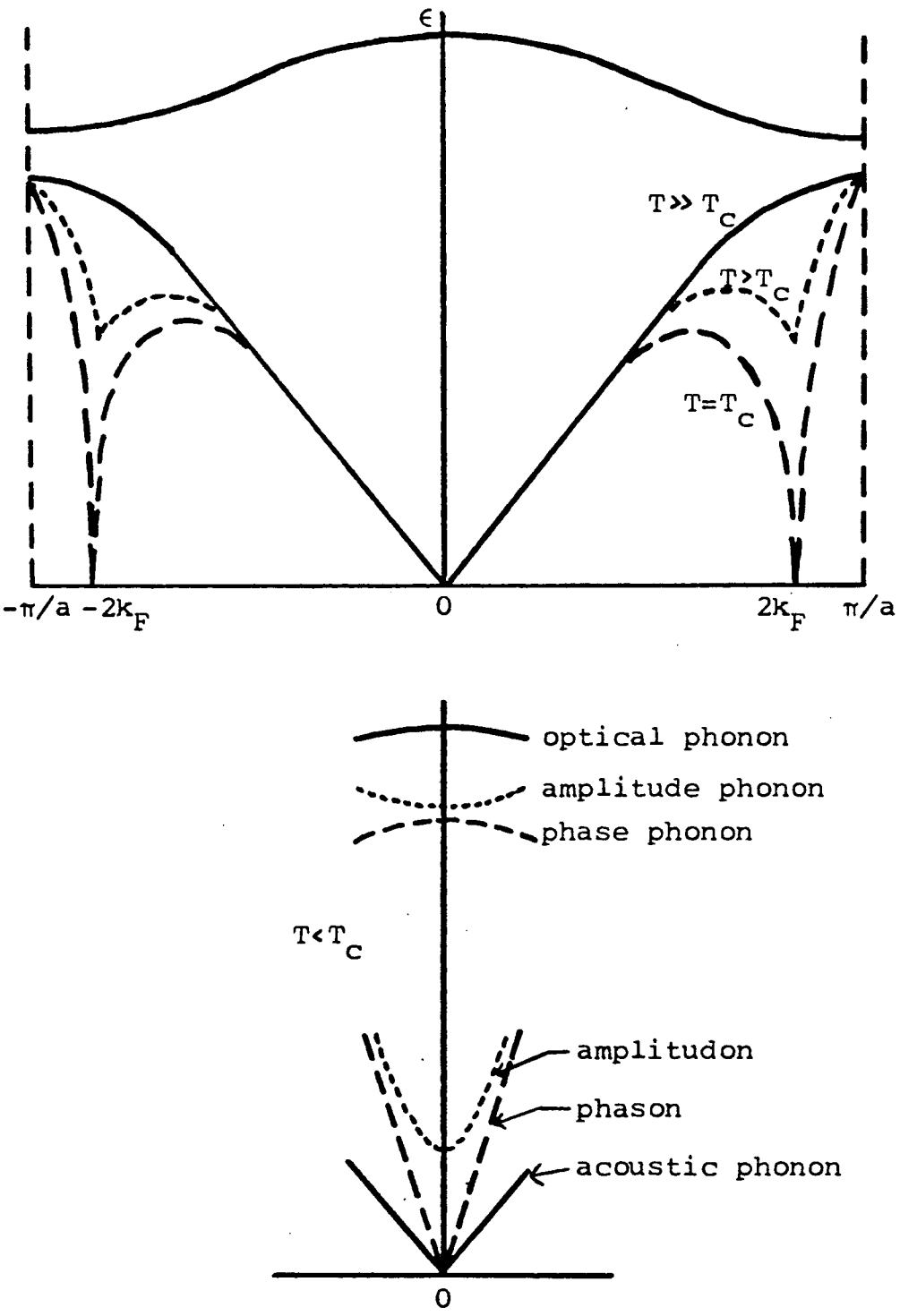

Fig. 6. Dispersion of acoustic and optical phonons in a one-dimensional solid above and below the CDW transition temperature.

carriers, give rise to two zone center collective modes called the phason and the amplitudon. The phason corresponds to phase oscillations of the coupled CDW-acoustic phonon mode, and is able to contribute to the electrical conductivity. The amplitudon corresponds to amplitude oscillations of the coupled mode, and is Raman-active. At the transition temperature both the phason and the amplitudon have zero frequency at the zone center. Below the transition temperature, the zone center frequency of the amplitudon increases with decreasing temperature. In mean field theory,[3] the frequency of the phason at the zone center remains zero below the transition temperature. However, in real materials, the phase of the CDW is pinned to the lattice either through commensurability with the lattice periodicity or through the random pinning potentials of the impurities. As a result, the phason will have a finite pinning frequency below the transition temperature.

At absolute zero, all the electronic states below the CDW energy gap are filled, and all the states above it are empty. As the temperature increases, carriers can be thermally excited across the energy gap. As a result, the electronic energy gained by opening the energy gap at the Fermi surface is reduced, and the size of the gap decreases. At a high enough temperature, the energy gap goes to zero, and the material reverts to its normal metallic state. The mathematics of the CDW transition in mean field theory is almost identical to the mathematics of the BCS theory of superconductivity, even though the physics is entirely different. In particular, the energy gap equation for the CDW transition is[2,4,5]

$$2\Delta = 3.5k_BT_c = 16\ \epsilon_F\ e^{-1/\lambda}\ .$$

In this equation, 2Δ is the CDW energy gap, T_c is the CDW transition temperature, ϵ_F is the Fermi energy, and λ is the dimensionless electron-phonon coupling constant. The main difference between this equation and the BCS result for superconductors is that the relevant energy is the Fermi energy rather than the Debye energy. Because the Fermi energy is generally one to two orders of magnitude larger than the Debye energy in the quasi-one-dimensional conductors, the energy gaps and transition temperatures of CDW materials are also one to two orders of magnitude larger than those of superconductors.

The frequency dependence of the conductivity of carriers condensed into a CDW can most conveniently be discussed in terms of the conductivity sum rule. This sum rule is the solid state analog of the f-sum rule of atomic physics, but instead of summing over the oscillator strengths of discrete atomic transitions, an integration is performed of $\sigma_1(\omega)$ over all frequencies. It can be easily shown (see Appendix A) that the sum rule is given by

$$\int_0^\infty \sigma_1(\omega)\ d\omega = \frac{1}{8}\ \omega_p^2 = \frac{\pi ne^2}{2m}\ .$$

Thus, the total area under the curve of σ_1 vs. frequency is determined by the concentration of the carriers, n, and their mass, m. Below the CDW transition temperature, the fraction of carriers condensing into the CDW increases with decreasing temperature, approximately as[6]

$$n_c/n = \sqrt{1 - T/T_c} \quad .$$

Thus, the oscillator strength of the condensed carriers increases proportionally the same amount with decreasing temperature. Because of the energy gap opening at the Fermi surface, as well as the strong coupling between the condensed carriers and the phonons, the frequency dependence of the conductivity of the condensed carriers is considerably different than that of the same carriers in their normal state. However, the total area under the conductivity curve in the two cases must be the same.

The oscillator strength of the condensed carriers appears in three different contributions. There is a single-particle continuum in the conductivity above the energy gap, a low frequency contribution to the conductivity from a pinned mode which includes the phason, and a contribution from coupled electron-optical phonon modes. We will discuss each of these three contributions in turn.

In the absence of a low frequency pinned mode, or coupling to optical phonons, all of the oscillator strength of the condensed carriers must appear in the single-particle continuum above the CDW energy gap. The frequency dependence of the conductivity[3] (see Appendix A) above the energy gap at absolute zero is shown in Fig. 7. There is a square root singularity in σ_1 at the energy gap, 2Δ.

When the effective mass of the CDW is not infinite, then some of the oscillator strength of the condensed carriers will also appear in the phason.[3] The fraction of the oscillator strength of the

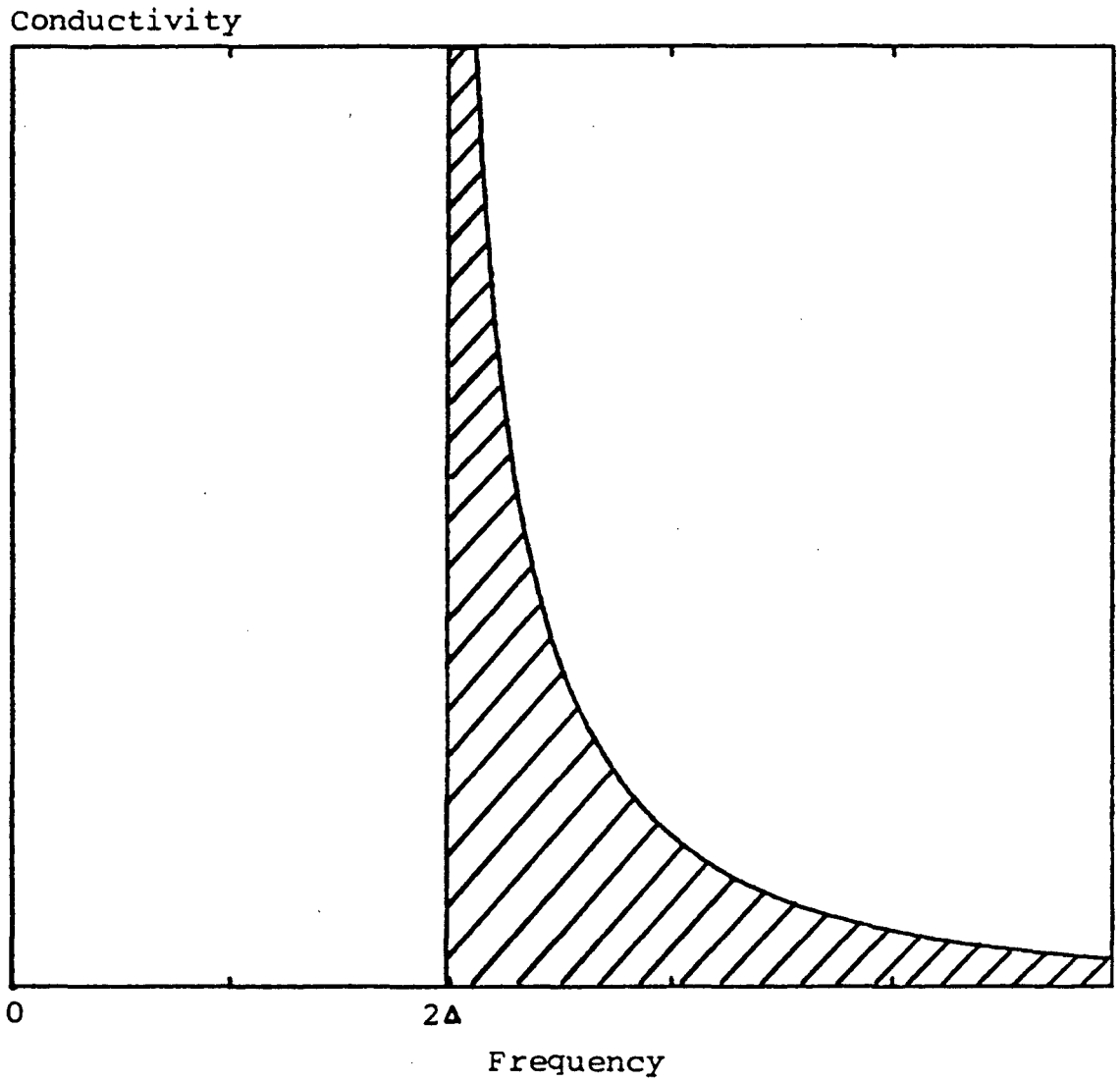

Fig. 7. Conductivity of the condensed carriers above the CDW energy gap at absolute zero in the absence of a pinned mode and phase phonons.

condensed carriers appearing in the phason is determined by the ratio of the band mass of the normal carriers to the CDW effective mass per carrier condensed in the CDW (this is also sometimes called the "Frohlich mass"). If the CDW effective mass is infinite, then no oscillator strength can appear in the phason. If the CDW effective mass is equal to the carrier band mass, then all of the oscillator strength of the condensed carriers will appear in the phason, and there will be no oscillator strength left to appear above the energy gap as a single-particle continuum. In general, the effective mass of the CDW is expected to be $\sim 10^3$ times larger than the carrier band mass. The large inertial mass of the CDW results from the fact that the moving CDW must drag the periodic lattice distortion along with it. The frequency dependence of the conductivity of the condensed carriers for a CDW effective mass equal to five electronic band masses ($M_F = 5m^*$) is shown in Fig. 8. In this case, 20% of the oscillator strength of the condensed carriers is in the phason. The oscillator strength is transferred primarily from the peak of the single-particle continuum to the phason, and the singularity in σ_1 at 2Δ is removed, leaving a square root edge.

The phason model[3] we have been discussing predicts the magnitude of the oscillator strength in the phason, but it does not correctly predict the frequency dependence of the conductivity. This model neglects pinning effects, and as a result it incorrectly predicts that all of the oscillator strength of the phason will appear in a superconducting δ-function at zero frequency. Various phenomenological

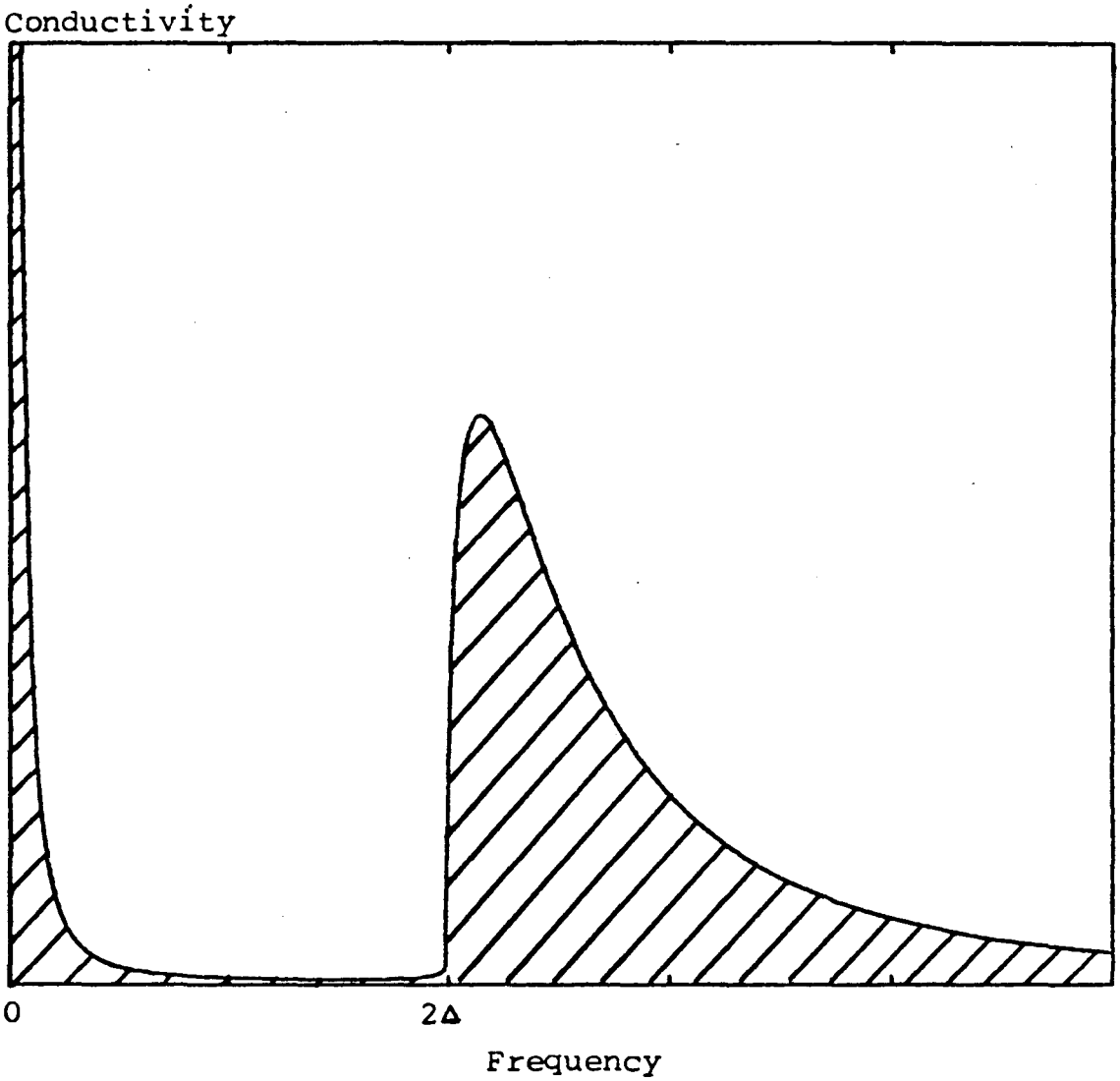

Fig. 8. Conductivity of condensed carriers at absolute zero when 20% of the oscillator strength is in the pinned mode.

models have been proposed to predict the frequency dependence of the conductivity for the low frequency pinned mode. We briefly consider the two most important models.

a. Classical model: The classical model[7] considers the CDW sitting in its pinning potential. When the CDW is translated by one wavelength, it will again be sitting in the same potential. Therefore, an alternate way of looking at the CDW is to consider it to be a particle with inertial mass M_F sitting in a periodic pinning potential. For small ac fields, the pinning potential can be approximated near the minimum as that of a harmonic oscillator. The CDW oscillates at its pinning frequency, thereby contributing to the ac conductivity. This model predicts the standard Lorentzian lineshape for the frequency dependence of the pinned mode. The total oscillator strength in the pinned mode is determined by the CDW effective mass and the number of condensed carriers, and is equal to the quantity predicted by the phason model. Therefore, this is a classical model of the pinned phason.

b. Tunneling model: An alternate approach[8] suggests that the CDW is able to tunnel through the pinning potential barrier, and thereby contribute to the dc conductivity without requiring all of the energy necessary to surmount the pinning potential. The frequency dependence of the tunneling contribution to the conductivity is given by the theory of photon assisted tunneling. A very small additional contribution to the conductivity from a classical phase mode is required in the tunneling model to fit the experimental data for $NbSe_3$.[9]

Both of these models are phenomenological, and both models have been found to give reasonable agreement with the experimentally measured frequency dependence of the conductivity of $NbSe_3$ at rf and microwave frequencies.[10]

In addition to the single-particle continuum above the energy gap and the low frequency pinned mode, the oscillator strength of the condensed carriers may also appear in coupled electron-optical phonon modes called phase phonons.[11] This case is analogous to the coupled electron-acoustic phonon which gave rise to the phason and amplitudon previously discussed. In the case of the optical phonons, the $\pm 2k_F$ optical phonons on an optical phonon branch can be mixed together by coupling to the CDW, and thereby create two new modes (see Fig. 6). Because of the periodic lattice distortion, these modes are also zone center modes. The amplitude mode occurs at a higher frequency, and corresponds to amplitude oscillations of the coupled CDW-optical phonon. It is Raman-active,[12] but not normally IR-active. The phase phonon occurs at a lower frequency and corresponds to phase oscillations of the coupled CDW-optical phonon. It is typically IR-active for light polarized parallel to the chain axis (because the CDW phase oscillations occur along this axis) even though the optical phonon may vibrate in a plane perpendicular to the chain axis.

Not all optical phonons form collective modes with the CDW carriers. The condition from group theory[13] (see Appendix B) for first-order electron-phonon coupling is

$$\Gamma e \subset \Gamma p \times \Gamma e$$

where Γ_e is the representation describing the symmetry of the electronic wavefunction, and Γ_p is the representation describing the symmetry of the optical phonon. When the crystal symmetry is such that all of the representations of the optical phonons are one-dimensional, as is the case for $NbSe_3$, then the above condition allows only the totally symmetric (A_g) optical phonon modes to couple in first-order to the CDW. These modes, however, are normally Raman-active, but never IR-active by themselves. Through coupling to the CDW, they become anomalously IR-active with an oscillator strength that can be quite large because of its electronic origin.

When the renormalized frequency of the phase phonon occurs below the CDW energy gap, the linewidth of the phonon can be quite sharp because it is simply the natural linewidth of the noninteracting phonon. However, when the phase phonon occurs above the energy gap, its linewidth becomes considerably broader because the coupled mode can decay through the creation of electron-hole pairs. Even more interesting, a phase phonon which occurs above the energy gap gives rise to a dip in the conductivity of the single-particle continuum, rather than a peak in the conductivity as seen for a phase phonon below the energy gap. This is a Fano interference effect[14-17] resulting from a discrete state interacting with a continuum of states. Examples of the frequency dependence of the conductivity for phase phonons appearing below and above the CDW energy gap are shown in Figs. 9 and 10, respectively.

CDW energy gaps, pinned modes, phase phonons, etc., which are predicted by these theories of one-dimensional solids, have been experimentally demonstrated by studies of various quasi-one-dimensional materials. Some of these materials and their properties are briefly reviewed here.

The quasi-one-dimensional conductor KCP [$K_2Pt(CN)_4Br_{0.3}$ $3H_2O$] undergoes a Peierls distortion above room temperature. The FIR spectrum of KCP reveals a sharp mode at 15 cm^{-1} which increases in strength with decreasing temperature.[18] It reaches a peak conductivity of ~1000 $(\Omega cm)^{-1}$ at 4.2K. This has been interpreted as the pinned CDW phason.[19] There is a Raman-active mode in KCP at 44 cm^{-1}, which is probably the CDW amplitudon.[20] At 300K, there is a decrease in the conductivity at frequencies below 1600 cm^{-1}. This is believed to be caused by a CDW pseudogap.[19] At lower temperatures this becomes a complete gap.

TTF-TCNQ (tetrathiofulvalene tetracyanoquinodimethane) is an organic linear chain compound which undergoes a CDW transition at 58K. Although various FIR measurements[21-24] have claimed to find evidence for a CDW pinned mode, there are large discrepancies in the reported frequency of the mode. At 100K, above the CDW transition, a pseudogap is found in the conductivity below 400 cm^{-1}.[25] The optical phonons seen in the FIR spectrum have been interpreted as phase phonons.[26]

A CDW energy gap and phase phonons have been found in the organic linear chain compound $TEA(TCNQ)_2$.[27] For light polarized parallel to the chain axis, ten phonons are seen in the CDW state of which

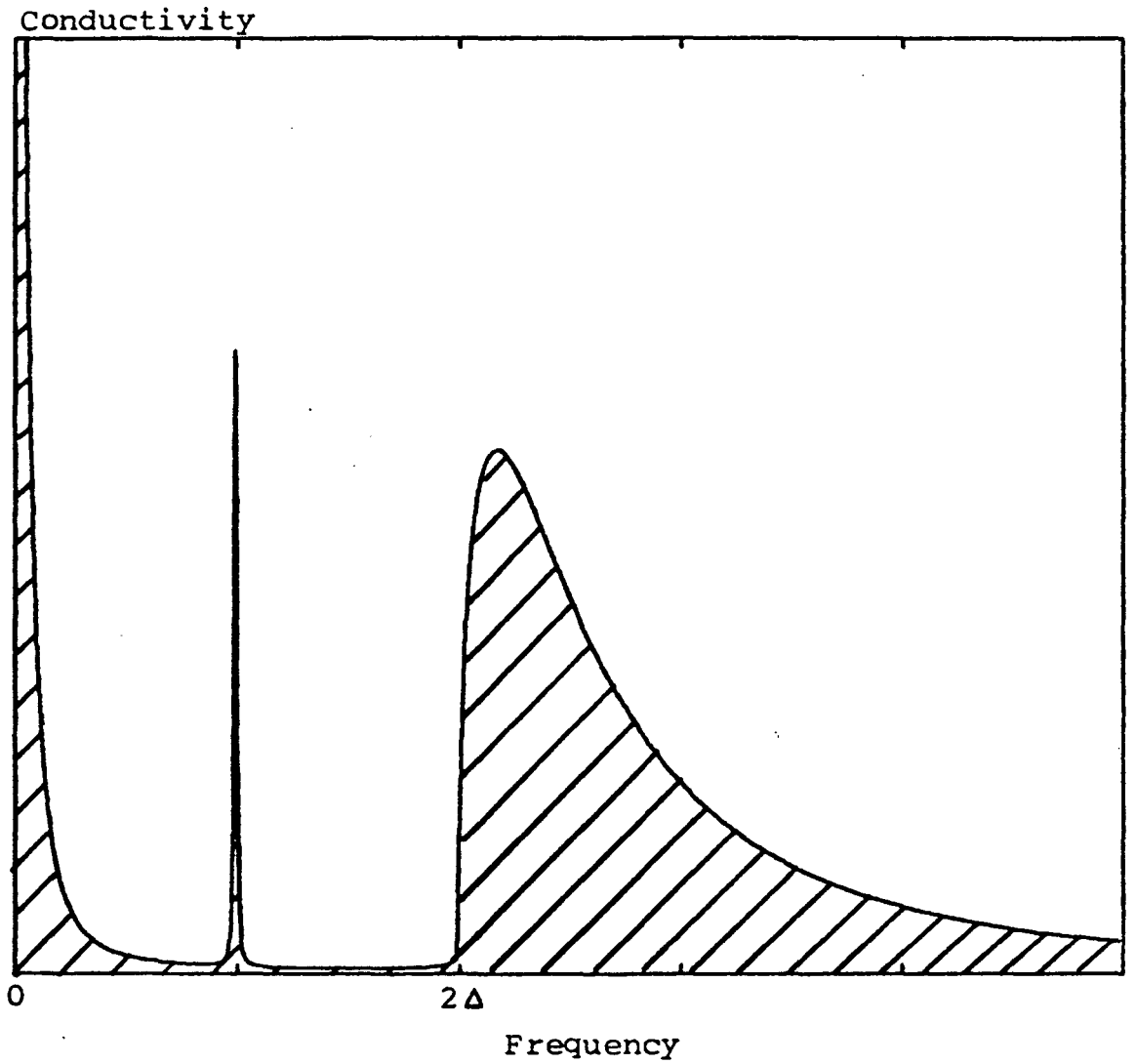

Fig. 9. Conductivity of condensed carriers for a pinned mode, a phase phonon below the energy gap, and a single-particle continuum above the energy gap.

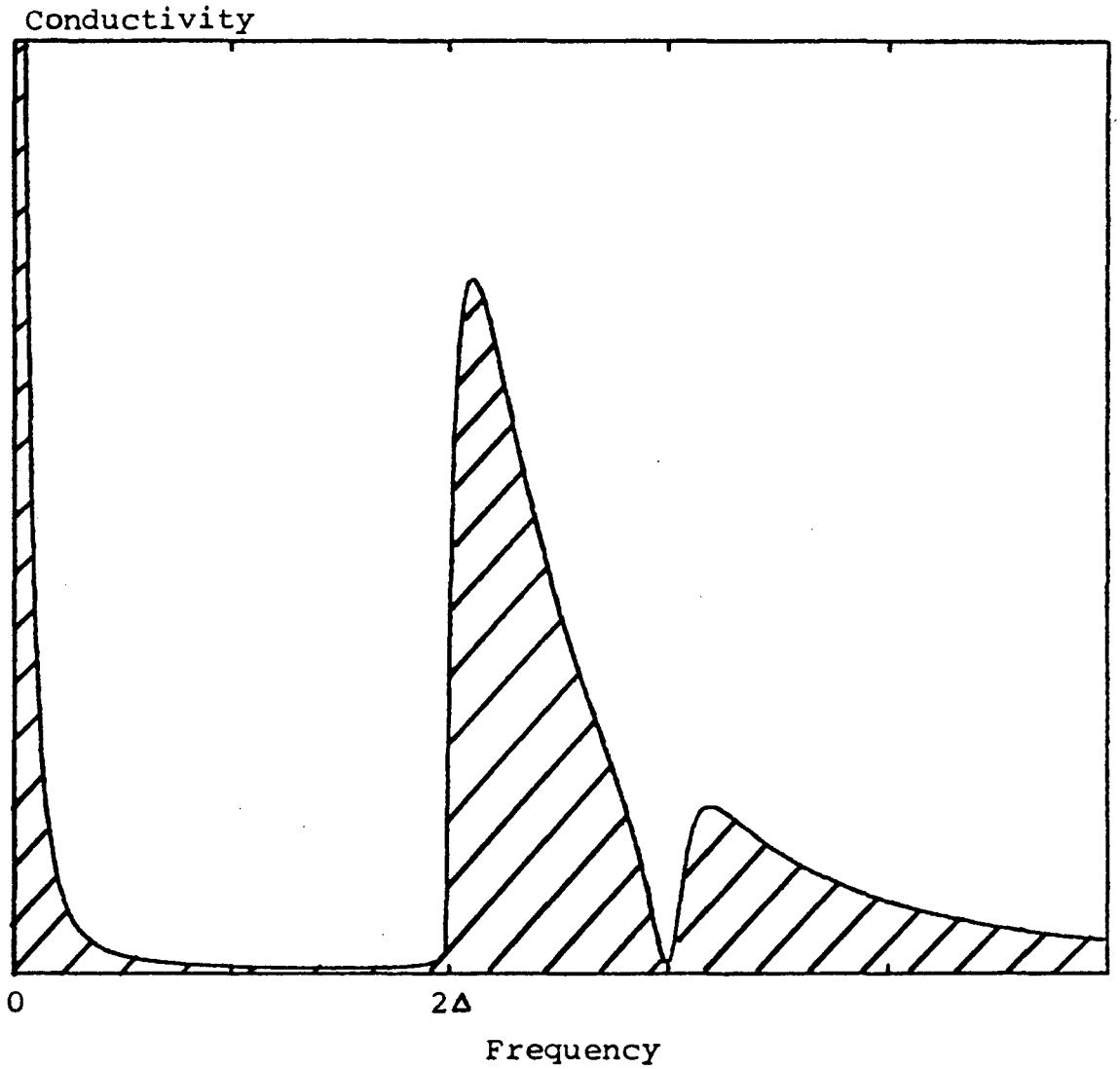

Fig. 10. Conductivity of the condensed carriers for a pinned mode, a phase phonon above the energy gap, and a single-particle continuum above the energy gap.

nearly all can be related to intramolecular vibrations of the TCNQ molecule with the appropriate symmetry to couple to the CDW electrons. The conductivity begins to increase above ~1600 cm^{-1}, and this is associated with the onset of single-particle transitions across the CDW energy gap. One of the phase phonons occurs above the CDW energy gap and gives rise to a Fano antiresonance in the conductivity.

The IR and Raman spectra have been measured for some of the transition metal trichalcogenides, including ZrS_3,[28-30] and HfS_3.[31] The Raman spectrum of $NbSe_3$ has been measured at room temperature.[32] However, none of these measurements have been made with these materials in the CDW state.

The transition metal dichalcogenides are layered (quasi-two-dimensional) compounds which are also found to undergo CDW transitions. The Raman spectrum of 2H-$TaSe_2$ reveals six phonon modes between 40 and 100 cm^{-1} which begin to appear below the incommensurate CDW transition at 122K.[33] The modes do not fully develop, however, until temperatures well below the second transition at 100K when the CDW becomes commensurate with the lattice. New Raman-active modes are found in the CDW states of 1T-TaS_2,[34] 1T-$TaSe_2$, and 1T-VSe_2.[35] New IR-active phonons are found in the CDW states of $TiSe_2$,[36,37] 1T-TaS_2, and 1T-$TaSe_2$.[38,39] A CDW energy gap of 0.25eV has been found for 2H-$TaSe_2$.[40]

References

1. R. E. Peierls, Quantum Theory of Solids, Clarendon Press, Oxford (1955) 108-112.
2. H. Fröhlich, Proc. Roy. Soc. London A223, 296 (1954).
3. P. A. Lee, T. M. Rice, P. W. Anderson, Sol. St. Comm. 14, 703 (1974).
4. C. G. Kuper, Proc. Roy. Soc. London A227, 214 (1955).
5. J. Bardeen, Sol. St. Comm. 13, 357 (1973).
6. J. Bardeen, private communication.
7. G. Grüner, A. Zawadowski, P. M. Chaikin, Phys. Rev. Lett. 46, 511 (1981).
8. J. Bardeen, Mol. Crys. Liq. Crys. 82, 1 (1982).
9. G. Grüner, A. Zettl, W. G. Clark, J. Bardeen, Phys. Rev. B24, 7247 (1981).
10. G. Grüner, L. C. Tippie, J. Sanny, W. G. Clark, N. P. Ong, Phys. Rev. Lett. 45, No. 11. 935 (1980).
11. M. J. Rice, Phys. Rev. Lett. 37 No. 1, 36 (1976).
12. B. Horovitz, H. Gutfreund, M. Weger, Phys. Rev. B17, No. 6, 2796 (1978).
13. N. O. Lipari, C. B. Duke, L. Pietronero, J. Chem. Phys. 65 No. 3, 1165 (1976).
14. U. Fano, Phys. Rev. 118 No. 2, 451 (1960).
15. U. Fano, Phys. Rev. 124 No. 6, 1866 (1961).
16. L. P. Gor'kov, E. I. Rashba, Sol. St. Comm. 27, 1211 (1978).

17. M. V. Belousov, A. M. Vaînrub, R. M. Vlasova, Sov. Phys. Sol. St., 18 No. 9, 1538 (1976).

18. P. Brüesch, H. R. Zeller, Sol. St. Comm. 14, 1037 (1974).

19. P. Brüesch, S. Strassler, H. R. Zeller, Phys. Rev. B12 No. 1, 219 (1975).

20. E. F. Steigmeier, R. Loudon, G. Harbeke, H. Auderset, G. Scheiber, Sol. St. Comm. 17, 1447 (1975).

21. D. B. Tanner, C. S. Jacobsen, A. F. Garito, A. J. Heeger, Phys. Rev. Lett. 32 No. 23, 1301 (1974).

22. J. E. Eldridge, Sol. St. Comm. 19, 607 (1976).

23. J. E. Eldrige, F. E. Bates, Sol. St. Comm. 30, 195 (1979).

24. D. B. Tanner, K. D. Cummings, C. S. Jacobsen, Phys. Rev. Lett. 47 No. 8, 597 (1981).

25. C. S. Jacobsen, Lecture Notes in Physics 95 (Springer-Verlag, NY, 1979) 223.

26. S. Etemad, Phys. Rev. B24, No. 9, 4959 (1981).

27. M. J. Rice, L. Pietronero, P. Brüesch, Sol. St. Comm. 21, 757 (1977).

28. S. Jandl, C. Deville Cavellin, J. Y. Harbec, Sol. St. Comm. 31, 351 (1979).

29. J. Y. Harbec, C. Deville Cavellin, S. Jandl, Phys. Stat. Sol. (b) 96, K117 (1979).

30. S. Jandl, M. Banville, J. Y. Harbec, Phys. Rev. B22, No. 12, 5697 (1980).

31. S. Jandl, J. Deslandes, Phys. Rev. B24, No. 2, 1040 (1981).

32. T. J. Wieting, A. Grisel, F. Levy, Ph. Schmid. Lecture Notes in Physics 95 (Springer-Verlag, NY, 1979), 354.

33. J. A. Holy, M. V. Klein, W. L. McMillan, S. F. Meyer, Phys. Rev. Lett. 37, No. 17, 1145 (1976).

34. J. R. Duffey, R. D. Kirby, R. V. Coleman, Sol. St. Comm. 20, 617 (1976).

35. J. E. Smith, Jr., J. C. Tsang, M. W. Shafer, Sol. St. Comm. 19, 283, (1976).

36. W. Y. Liang, G. Lucovsky, J. C. Mikkelsen, R. H. Friend, Philos. Mag. B39 No. 2, 133 (1979).

37. J. A. Holy, K. C. Woo, M. V. Klein, F. C. Brown, Phys. Rev. B16 No. 8, 3628 (1977).

38. D. R. Karecki, B. P. Clayman, Sol. St. Comm. 19, 479 (1976).

39. D. R. Karecki, B. P. Clayman, Phys. Rev. B19 No. 12, 6367 (1979).

40. A. S. Barker, Jr., J. A. Ditzenberger, F. J. DiSalvo, Phys. Rev. B12 No. 6, 2049 (1975).

IV. Properties of $NbSe_3$

$NbSe_3$ was first synthesized in 1975 by Meerschaut and Rouxel.[1] It is typically prepared by heating stoichiometric amounts of niobium and selenium in a sealed quartz tube under vacuum.[2] The mixture is heated to 700°C and allowed to react for about fifteen days before it is quenched. The resulting crystals are needle-like fibers with thicknesses of 3 to 10 μm and lengths of 5 to 10 mm. They have a metallic luster and are intertwined, with an appearance similar to a fine grade of steel wool.

X-ray diffraction techniques have been used[2,3] to determine the crystal structure of $NbSe_3$, which is shown in Fig. 11. The lattice is monoclinic with lattice parameters of a = 10.009 Å, b = 3.4805 Å, c = 15.629 Å, and β = 109.47°. The space group is $P2_1/m$ (C_{2h}^2), which is nonsymmorphic. It includes a screw axis $\{C_2|1/2\vec{b}\}$ along the fiber axis (which is the b-axis), and a glide plane $\{\sigma|1/2\vec{b}\}$ in the ac plane. There are six formula units per unit cell. These are arranged in six chains along the fiber axis. Each chain consists of stacked trigonal prisms which share triangular faces of selenium atoms. A niobium atom is located at the center of each prism. Covalent-ionic bonds link chains together to form slabs parallel to the bc plane. Each slab is two trigonal prisms thick. The slabs are bound to each other only through weak Van der Waals bonds. Thus, the crystal tends to cleave parallel to the bc plane between slabs, and as a result the thinnest fiber dimension is usually perpendicular to the bc plane.

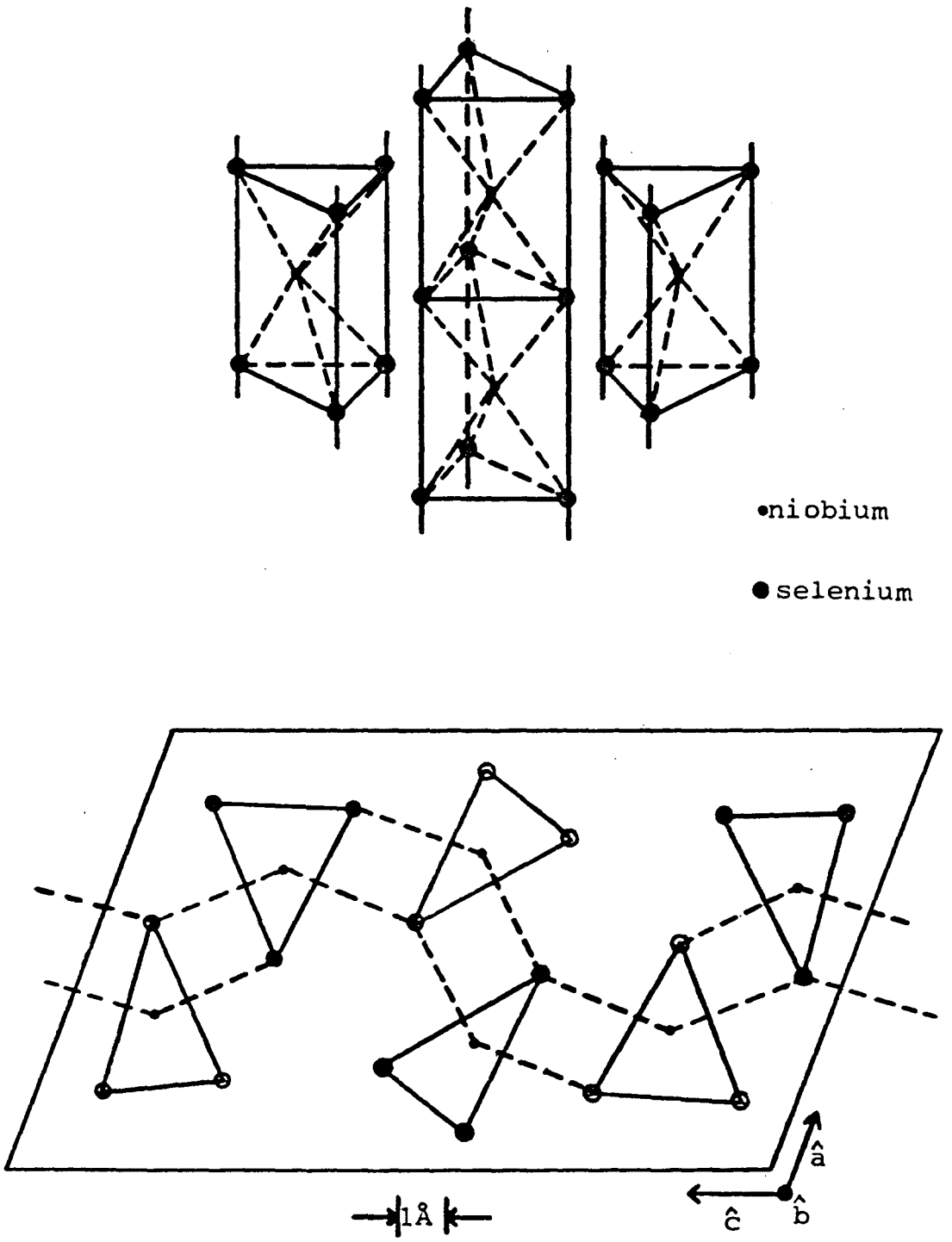

Fig. 11. Crystal structure of $NbSe_3$.

Each niobium atom is coordinated to six selenium atoms at the end faces of the prism and to two additional selenium atoms at the side faces of the prism. There are three independent niobium sites and nine independent selenium sites in the unit cell. Each prismatic chain is composed of only one type of niobium site.

The average bonding distance between niobium atoms and selenium atoms at the prism end faces is 2.65 Å. The average bonding distance between niobium atoms and selenium atoms on the side faces is 2.79 Å. The intrachain separation of niobium atoms is 3.48 Å, while the interchain separation of niobium atoms is 4.35 Å.

There are 24 atoms in the undistorted unit cell of $NbSe_3$, and therefore there are 69 optical phonons in addition to the three acoustic phonons. The irreducible representations describing the symmetry of the acoustic phonons are (see Appendix B)

$$\Gamma_A = A_u + 2B_u$$

and of the optical phonons are

$$\Gamma_o = 24A_g + 12B_g + 11A_u + 22B_u.$$

The inversion symmetry in the unit cell prevents any optical phonon from being both Raman and IR-active. The A_g and B_g modes are potentially Raman-active, and the A_u and B_u modes are potentially IR-active. For the C_{2h} point group of $NbSe_3$, all of the

irreducible representations are one-dimensional, so only the 24 A_g optical phonons can couple in first-order to the CDW carriers (see Appendix B). The A_g and B_u modes correspond to vibrations in the ac plane, perpendicular to the fiber axis, while the B_g and A_u modes correspond to vibrations along the fiber axis. Thus, the 11 A_u modes are potentially IR-active for light polarized parallel to the fiber axis, while the 22 B_u modes are potentially IR-active for light polarized perpendicular to the fiber axis.

The existence of CDW phase transitions in $NbSe_3$ was verified through the techniques of electron diffraction[2,4,5] and diffuse x-ray diffraction.[6] These techniques are sensitive to the electronic charge distribution in the crystal, rather than the positions of the lattice ions. Below 145K (T_1) a CDW superlattice appears with lattice parameters a' = a, b' = 4.1b, and c' = c. The T_1 CDW is incommensurate with the lattice and its wavevector is 0.244±0.004b*, along the fiber axis. No diffuse scattering streaks were found above the T_1 transition,[2,6] and hence fluctuation effects characteristic of materials with a very low effective dimensionality are not important in $NbSe_3$.

Below 59K (T_2) a second CDW superlattice appears[6] which is independent of the T_1 CDW superlattice. The lattice parameters for the T_2 CDW superlattice are a" = 2a, b" = 3.8b, and c" = 2c. The corresponding CDW wavevector is 0.5a* + 0.263±0.005b* + 0.5c*. This CDW is also incommensurate with the lattice along the fiber axis, but commensurate with the lattice along the two axes transverse to the fiber axis. It doubles the unit cell size along these axes.

Measurements of the dc electrical resistivity of $NbSe_3$ parallel to the fiber axis as a function of temperature reveal two striking anomalies.[3,7] The electrical resistivity decreases steadily with decreasing temperature until the CDW transition $T_1 = 145K$, when the resistivity begins to increase. At 125K the resistivity reaches a maximum, and then begins decreasing again until the second CDW transition $T_2 = 59K$. The resistivity again increases below this temperature, and peaks at 48K before beginning a uniform decrease with decreasing temperature. At about 10K, impurity scattering processes begin to become important, and the resistivity saturates to a fairly constant value.

At room temperature the dc conductivity is ~5000 $(\Omega cm)^{-1}$.[5,8,9] At liquid helium temperatures, the conductivity increases by a factor of 20 to 200 times the room temperature value, depending upon sample purity. The conductivity anisotropy in $NbSe_3$ is fairly low. At 5K, $\sigma_b/\sigma_c \approx 20$.[10] This small anisotropy indicates a significant two-dimensional character for $NbSe_3$.

At temperatures below the CDW transitions, the conductivity of $NbSe_3$ is a function of the applied electric field for fields exceeding a small threshold value of 0.01 to 0.1 V/cm.[11] Field strengths about an order of magnitude larger than the threshold field greatly reduce or completely suppress the two resistive anomalies.[12] There is no observable change in the intensity of the CDW superlattice diffraction spots in the presence of electric fields large enough to substantially reduce the resistive anomalies.[6] The enhanced

conductivity is, therefore, believed to result from depinning of the CDW's, causing them to slide through the lattice and carry a current.

The electrical conductivity has been studied as a function of pressure. The transition temperatures decrease linearly with increasing pressure with a slope $dT_c/dP = 4K/kbar$.[13] At 4kbar, the amplitude of the T_1 resistive anomaly is suppressed by 30 percent. At 6kbar, the amplitude of the T_2 anomaly is suppressed by more than 95 percent. $NbSe_3$ does not become superconducting under ambient pressure down to 150mK.[14] At 6.5kbar, however, it has a superconducting transition at 2.4K, as evidenced by a Meissner effect. At 0.5kbar, the transition temperature is 0.3K.

Impurities have a strong effect upon the electrical conductivity. The threshold field scales as the square of the impurity concentration for tantalum impurities, which are isoelectronic with niobium and are therefore uncharged.[15] Titanium, which is a charged impurity, has a much larger effect. A concentration of 100 ppm of titanium is sufficient to raise the threshold field to >6V/cm.[15]

The frequency dependence of the conductivity of $NbSe_3$ in the rf and microwave regions has been measured.[7,16,17] At 40K, the conductivity increases smoothly from the dc value to about twice the dc conductivity at 100 MHz. The conductivity remains at this value to >9.3GHz. There is a peak in the imaginary part of the conductivity at ~60MHz, which corresponds to an enormous positive value, 2×10^8, for the real part of the dielectric function. The enhanced ac conductivity in this frequency region is due to the response of the CDW pinned mode.

There is an abrupt increase of noise in the potential difference across a $NbSe_3$ fiber when the applied field is raised above the threshold field.[11] At slightly higher fields, discrete frequencies with high harmonic content are present in the noise. Presumably, the depinned sliding CDW's give rise to the narrow band noise at discrete frequencies. The frequency of the noise is directly proportional to the CDW current, and hence the CDW velocity. If the frequency of the noise, ν, is inversely proportional to the CDW wavelength, λ, then a simple equation relates the CDW current and noise frequency to the concentration of carriers condensed in the CDW. This is

$$I_{CDW}/\nu A = ne\lambda \quad ,$$

where A is the cross sectional area of the fiber.[18] Estimates[19-21] of the concentration of carriers condensing in each CDW of $NbSe_3$ based upon the above equation, however, vary widely from 6.2×10^{19} cm^{-3} to 2.3×10^{22} cm^{-3}.

Although the simplest model of the narrow band noise relates the noise frequency to the CDW wavelength, various other models have been proposed in which the relevant length is the lattice spacing,[22] half the CDW wavelength,[23,24] or a soliton lattice spacing.[21] The first two of these models cause the estimates of condensed carrier concentrations to increase by a factor of four and two, respectively. The third model causes estimates of the condensed carrier concentration to decrease by a factor of twenty or more, depending on which CDW is being considered.

The differential resistance of $NbSe_3$ has been measured[25] in the presence of a constant electric field greater than the threshold field, while an rf current of constant amplitude was passed through the crystal and the frequency was varied from 1 to 10 MHz. There is a resonant response in dV/dI whenever the rf frequency is equal to one of the narrow band noise frequencies. The resonant frequencies are proportional to the CDW current density.

Extensive magnetotransport measurements have been made on $NbSe_3$. Hall effect measurements demonstrate that electrons are the majority carrier at room temperature, but below 15K holes become the majority carrier, as the Hall constant changes sign.[26] Very large carrier mobilities of ~40,000 cm^2/Vs at 4.2K are inferred from magneto-resistance measurements.[10] At 55K, the mobility is ~200 times smaller, and at room temperature it is only ~30cm^2/Vs.[27]

Shubnikov-de Haas measurements on $NbSe_3$ at liquid helium temperatures give evidence of closed orbits on the Fermi surface with cross sectional areas of only 10^{-3} to 10^{-1} of the cross sectional area of the Brillouin zone.[28,29] The carrier effective masses estimated[28,30] from the Shubnikov-de Haas data vary from $0.236m_o$ to $0.30m_o$ for orbits perpendicular to the $\vec{c}$-axis. An effective mass equal to the free electron mass m_o is estimated for orbits perpendicular to the $\vec{b} \times \vec{c}$ axis.[30]

Cyclotron resonance measurements at 2K also give values for the carrier band masses.[27] From these measurements there is evidence for two types of carriers with effective masses of $0.18m_o$ and $0.71m_o$

for orbits perpendicular to the $\vec{b} \times \vec{c}$ axis. Lifetime estimates for these carriers are $>10^{-11}$s and 2.5×10^{-11}s, respectively.

It is possible that carriers with much larger effective masses may also be present in $NbSe_3$, because these would be difficult to detect by magnetotransport measurements.[28] An effective mass of $6m_o$ has been suggested[9] because this is the effective mass of d electrons in niobium.

A two-band model[31] has been proposed to interpret the magnetotransport data and the conductivity anisotropy data. A reasonable fit can be obtained to the data below T_2. The model predicts that $\sim 2 \times 10^{19}$ cm^{-3} holes condense into the T_2 CDW, and that at liquid helium temperatures the remaining concentration of free electrons is 1.09×10^{18} cm^{-3} and of free holes is 6.0×10^{18} cm^{-3}. The concentration of carriers condensing into the T_2 CDW predicted by this model is much smaller than the result obtained from the analysis of the narrow band noise data when the CDW wavelength is assumed to be the relevant periodicity in the analysis.

Hall effect measurements at room temperature give a free carrier concentration of $\sim 1.4 \times 10^{21}$ cm^{-3}.[8] Band structure calculations[32] have been used[25] to estimate a room temperature carrier concentration of 3.9×10^{21} cm^{-3}. If this latter number is used to estimate[20] the concentration of free carriers remaining below both CDW transitions on the basis of the narrow band noise measurements, then the result is $\sim 10^{21}$ cm^{-3}. This value is many times larger than the result from the two-band model.

CDW domains have apparently been observed directly by transmission electron dark field microscopy[33] in which the image is obtained from a single superlattice satellite reflection. Strandlike domains can be resolved which appear to twinkle, with new strands appearing and disappearing in a period of a few seconds. Typical strand dimensions are 2×10^4 Å by 200 Å. The twinkling of the domains is not due to depinning of the CDW's by the fringing fields of the electron microscope,[34] but what does cause the twinkling is at present unknown.

The Raman spectrum of $NbSe_3$ has been measured at room temperature,[35] and is shown in Fig. 12. Approximately sixteen of the A_g optical phonons are seen with frequencies between 40 and 260 cm^{-1}.

At present, the two main models of CDW transport are the classical model[19] and the tunneling model[36] discussed in the previous chapter. Neither of these two models appears to be uniformly successful in explaining the results of various experimental measurements which have been made on $NbSe_3$ and related CDW compounds. The threshold field measured for nonlinear conduction in $NbSe_3$ is predicted by both models, as is the general frequency dependence of the conductivity in the rf and microwave regions. The threshold field is predicted to scale with the square of the impurity concentration in both models[36,37] as found by experiment. Measurements of the CDW conductivity in the presence of large amplitude ac fields can be explained by both models.[38,39] Shapiro-like steps in the dc I-V characteristics, which are induced by externally applied microwave radiation, are in good agreement with both models.[40]

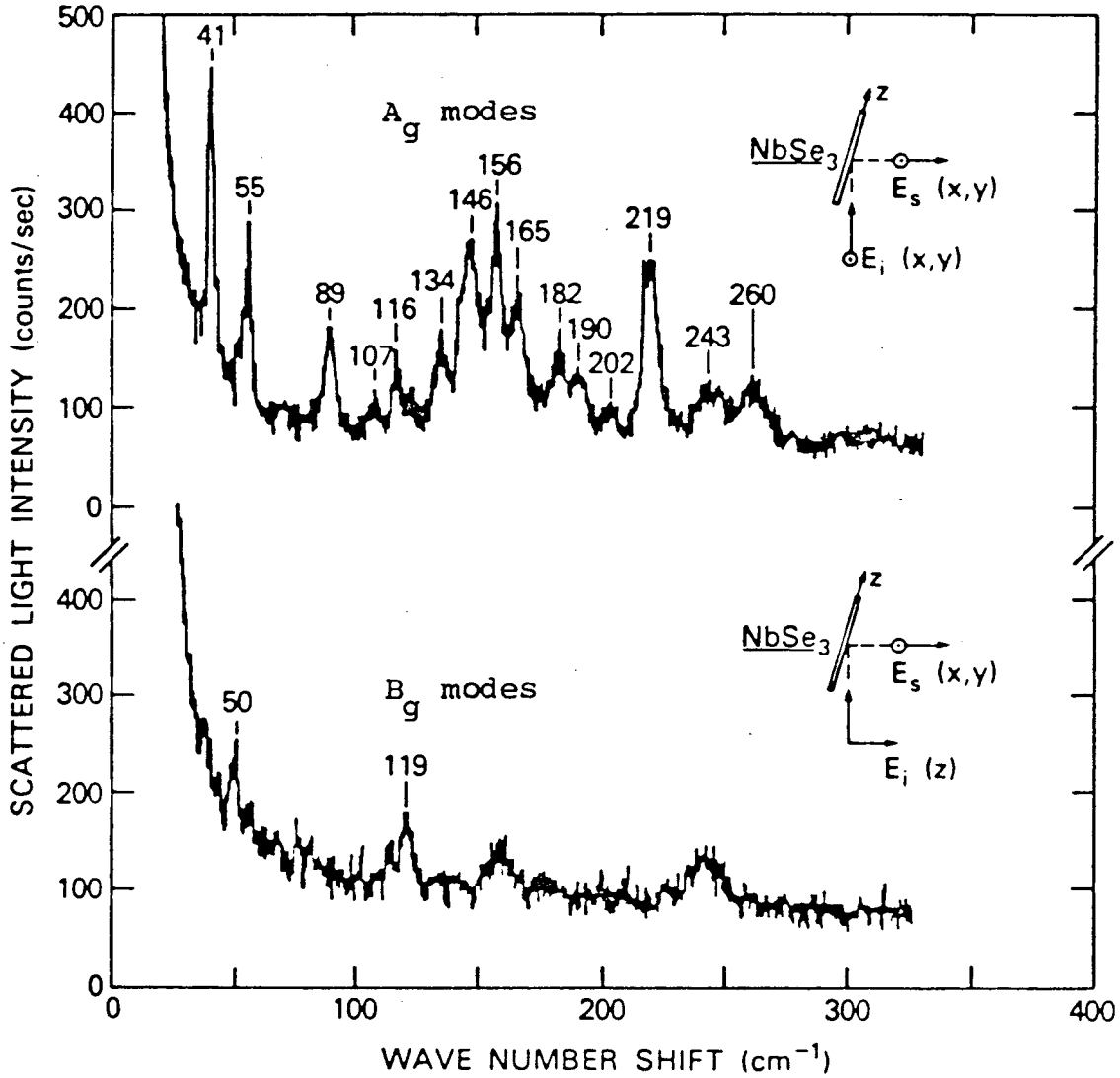

XBL 837-10697

Fig. 12. Room temperature Raman spectrum of $NbSe_3$ from ref. 44.

However, the classical model predicts that the differential conductance dI/dV should diverge at the threshold field, in direct contrast to the experimental results.[41,42] It may be necessary to assume a distribution of pinning energies[43] or of CDW domains[9] to eliminate this divergence in the classical model.

On the other hand, the tunneling model predicts that there should be a finite dc CDW current when the energy quantum of the ac field, $\hbar\omega/e^*$, exceeds the difference between the applied dc field and the threshold field, even when the classical field amplitude of the ac field is smaller than the difference. Experimentally, a finite dc CDW current is obtained only when the combined amplitudes of the ac and dc fields exceed the threshold field, as predicted by the classical model.[42] The failure of the tunneling model in this instance may be due to the oversimplified way in which the theory of photon assisted tunneling has been applied to CDW's.

References

1. A. Meerschaut, J. Rouxel, J. Less Comm. Metals 39, 197 (1975).
2. J. L. Hodeau, M. Marezio, C. Roucau, R. Ayroles, A. Meerschaut, J. Rouxel, P. Monceau, J. Phys. C 11, 4117 (1978).
3. P. Haen, P. Monceau, B. Tissier, G. Waysand, A. Meerschaut, P. Molinie, J. Rouxel, Proc. 14'th Int'l. Conf. Low Temp. Phys., Otaniemi, Finland (1975), North-Holland, Amsterdam, 5, 445.
4. K. Tsutsumi, T. Takagaki, M. Yamamoto, Y. Shiozaki, M. Ido, T. Sambongi, K. Yamaya, Y. Abe, Phys. Rev. Lett. 39 No. 26, 1675 (1977).
5. S. Nakamura, R. Aoki, Sol. St. Comm. 27, 151 (1978).
6. R. M. Fleming, D. E. Moncton, D. B. McWhan, Phys. Rev. B18 No. 10, 5560 (1978).
7. N. P. Ong, Ph.D. Thesis, U. C. Berkeley (1976).
8. G. X. Tessema, N. P. Ong, Phys. Rev. B23 No. 10, 5607 (1981).
9. P. Monceau, J. Richard, M. Renard, Phys. Rev. B25, 931 (1982).
10. N. P. Ong, J. W. Brill, Phys. Rev. B18 No. 10, 5265 (1978).
11. R. M. Fleming, C. C. Grimes, Phys. Rev. Lett. 42 No. 21, 1423 (1979).
12. P. Monceau, N. P. Ong, A. M. Portis, A. Meerschaut, J. Rouxel, Phys. Rev. Lett. 37 No. 10, 602 (1976).
13. J. Chaussy, P. Haen, J. C. Lasjaunias, P. Monceau, G. Waysand, A. Waintal, A. Meerschaut, P. Molinie, J. Rouxel, Sol. St. Comm., 20, 759 (1976).

14. P. Monceau, J. Peyrard, J. Richard, P. Molinie, Phys. Rev. Lett. 39 No. 3, 161 (1977).

15. J. W. Brill, N. P. Ong, J. C. Eckert, J. W. Savage, S. K. Khanna, R. B. Somoano, Phys. Rev. B23, 1517 (1981).

16. G. Grüner, L. C. Tippie, J. Sanny, W. G. Clark, N. P. Ong, Phys. Rev. Lett. 45 No. 11, 935 (1980).

17. S. Longcor, Ph.D. Thesis, U.C. Berkeley (1980).

18. J. Bardeen, E. Ben Jacob, A. Zettl, G. Grüner, Phys. Rev. Lett. 49 No. 7, 493 (1982).

19. G. Grüner, A. Zawadowski, P. M. Chaikin, Phys. Rev. Lett. 46 No. 7, 511 (1981).

20. J. Richard, P. Monceau, M. Renard, Phys. Rev. B25, 948 (1982).

21. N. P. Ong, C. M. Gould, Sol. St. Comm. 37, 25 (1980).

22. P. Bak, Phys. Rev. Lett. 48 No. 10, 692 (1982).

23. M. Weger, B. Horovitz, Sol. St. Comm. 43 No. 7, 583 (1982).

24. P. Monceau, M. Renard, J. Richard, M. C. Saint-Lager, H. Salva, Z. Z. Wang, preprint.

25. P. Monceau, J. Richard, M. Renard, Phys. Rev. Lett. 45 No. 1, 43 (1980).

26. N. P. Ong, P. Monceau, Sol. St. Comm. 26, 487 (1978). The c-axis is mislabelled as the a-axis in this paper.

27. R. J. Wagner, N. P. Ong, preprint.

28. R. M. Fleming, J. A. Polo, Jr., R. V. Coleman, Phys. Rev. B17 No. 4, 1634 (1978).

29. P. Monceau, A. Briggs, J. Phys. C, 11 L465 (1978).

30. P. Monceau, Sol. St. Comm. 24, 331 (1977).

31. N . P. Ong, Phys. Rev. B18 No. 10, 5272 (1978).

32. D. W. Bullett, J. Phys. C 12, 277 (1979).

33. K. K. Fung, J. W. Steeds, Phys. Rev. Lett. 45 No. 21, 1696 (1980).

34. C. H. Chen, R. M. Fleming, P. M. Petroff, Bull. Am. Phys. Soc. 28 No. 3, 426 (1983).

35. T. J. Wieting, A. Grisel, F. Levy, Ph. Schmid, Lecture Notes in Physics 95 Springer-Verlag, NY (1979), 354.

36. J. Bardeen, Mol. Crys. Liq. Crys. 82, 1 (1982).

37. P. A. Lee, T. M. Rice, Phys. Rev. B19, 3970 (1979).

38. G. Grüner, W. G. Clark, A. M. Portis, Phys. Rev. B24 No. 6, 3641 (1981).

39. J. R. Tucker, J. H. Miller, Jr., K. Seeger, J. Bardeen, Phys. Rev. B25, No. 4, 2979 (1982).

40. A. Zettl, G. Grüner, preprint.

41. J. B. Sokoloff, Phys. Rev. B23, 1992 (1981).

42. G. Grüner, A. Zettl, W. G. Clark, J. Bardeen, Phys. Rev. B24, 7247 (1981).

43. S. W. Longcor, A. M. Portis, Bull. Am. Phys. Soc. 25, 340 (1980).

44. T. J. Wieting, A. Grisel, F. Levy, Mol. Crys. Liq. Crys. 81, 117 (1982).

V. Measurements and analysis of the infrared properties of $NbSe_3$

Because the typical fiber thickness of $NbSe_3$ is ~5μm, which is much smaller than the relevant FIR wavelengths, accurate FIR measurements are difficult. In order to obtain a reflected or transmitted signal of sufficient intensity, a $NbSe_3$ sample must be composed of a large number of fibers. We have used several methods to make large area samples, none of which is ideal, but in combination the different samples provide a large amount of information.

To obtain accurate measurements as a function of temperature, a sample can was constructed as shown in Fig. 13, composed of two sapphire window mounts soldered back to back. A balled mesh of $NbSe_3$ fibers was placed inside the can, and the can was filled with helium exchange gas. A carbon resistor thermometer, calibrated by comparison with a Lakeshore Cryotronics germanium thermometer, was glued to the outside of the can, and a length of manganin wire was wrapped around the outside of the can as a heater. In this way the temperature of the $NbSe_3$ fibers could be accurately regulated to ±0.5K. The sample can was placed inside the sample chamber of the apparatus shown in Fig. 1, in place of the sample wheel. The sample temperature could be regulated from ~1.5K to ~120K.

Measurements were made of the transmittance of the fiber mesh in the can. The measured spectrum, however, is not the same as the transmittance or reflectance spectrum of bulk material, because it involves complicated scattering effects of the radiation through the mesh. Therefore, it cannot be simply analyzed to obtain the optical

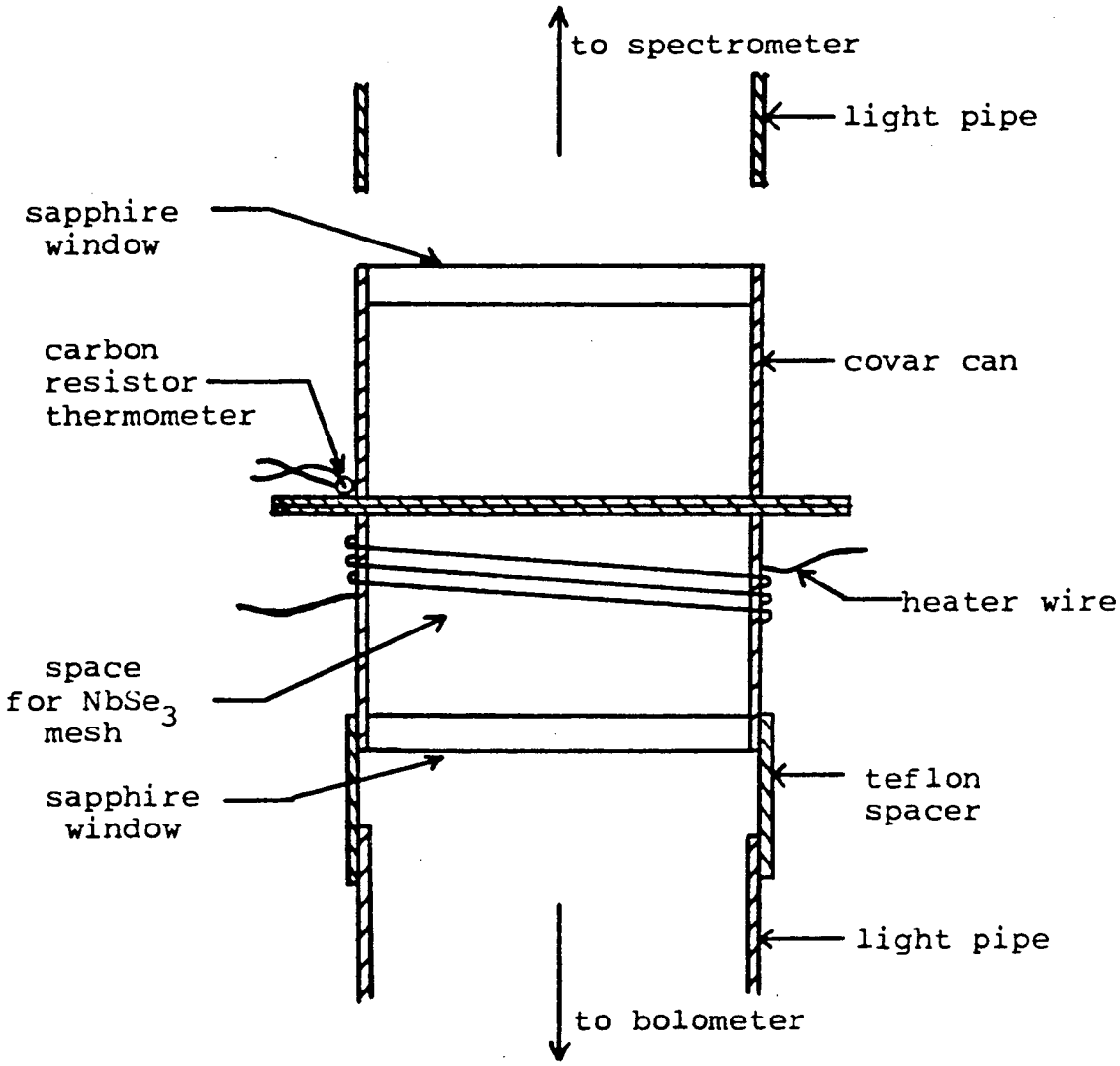

Fig. 13. Sample can for measurements on $NbSe_3$ mesh.

constants of $NbSe_3$. However, the temperature dependence of sharp features (e.g., optical phonons) in the spectrum could be accurately measured with this apparatus.

A second method to obtain a large area sample involved combing $NbSe_3$ fibers across a piece of mylar tape used as a substrate. The fibers were stuck to the tape approximately parallel to each other and packed closely enough compared to FIR wavelengths so that the sample was opaque to FIR radiation polarized parallel to the fibers (~1 percent transmittance). The sample was ~75 percent opaque to visible light, indicating that most of the surface area was covered by $NbSe_3$ fibers. The sample approximates a single-crystal surface for reflected radiation polarized parallel to the fibers, although surface roughness scatters radiation from the beam and makes normalization of the spectrum difficult. The requirement that the IR wavelength must be large compared with the characteristic surface roughness limits the frequency range over which measurements can be made. To partially correct for surface scattering effects, the data were normalized to the reflectance of the sample after it was covered with evaporated gold. In practice, it was difficult to get a good, shiny gold coating of the sample that was thick enough so that the FIR radiation would not penetrate to the $NbSe_3$, but was not too thick that it began to fill in the surface roughness. Thus, there is uncertainty in the normalization of the reflectance measurements, and therefore uncertainty in the values of the optical constants calculated from them.

The spectrum of the light polarized perpendicular to the fibers is probably not meaningful in terms of a single-crystal surface. The sample geometry is similar to that of a grid polarizer, and probably the majority of the light reflected perpendicular to the grid direction comes from misaligned fibers in the sample. The FIR radiation does not interact strongly with the fibers when polarized perpendicular to the fiber axis, because of the thinness of the fibers.

For making reflectance measurements, the tape sample was glued to a black epoxy substrate with GE varnish. The epoxy substrate was glued to the brass sample wheel. The carbon resistor thermometer and heater were attached to the brass wheel, and therefore the thermometer was separated from the sample by a layer of mylar, varnish, and epoxy. When the sample was at elevated temperatures, the sample chamber was evacuated and therefore the sample was not well heat sunk to the thermometer. Absorption of the incident radiation by the sample could raise its temperature relative to that of the thermometer, and therefore the accuracy of these temperature measurements was estimated to be only ±5K.

A third method for obtaining a large area sample involved compressing fibers into a pellet. Very large pressures could be obtained from a hydraulic press for compressing the sample into a pellet with a very smooth surface. However, measurements of the electrical conductivity of the sample as a function of temperature showed that the material was no longer metallic below T_2. By squeezing $NbSe_3$ fibers in rolling pin fashion between two brass

surfaces by hand, a pellet could be obtained in which both CDW phase transitions were present and which remained metallic at liquid helium temperatures. The surface of this sample, however, was not completely smooth. The residual resistivity ratio of this sample was ~5, and this sample was used for reflectance measurements. The typical residual resistivity ratio of the $NbSe_3$ fibers supplied to us by P. Monceau was ~20.

Surface roughness is not as much of a problem for the pellet sample as it is with the tape sample. However, the pellet is a nonoriented polycrystalline material, and therefore polarized light measurements are not useful. In addition, if the individual crystallites in the pellet are larger than or comparable to the FIR wavelengths, then they can cause unwanted light scattering.

Absorptance measurements were also made with fibers that were slightly larger (~20μm thick) supplied by N. P. Ong. The fibers were attached with vacuum grease to the sapphire substrate of a conventional composite bolometer in place of the metallic film absorber. However, because the absortance data could not be normalized, no new information was obtained by this technique.

At room temperature the FIR reflectance of $NbSe_3$ is large (>90 percent) and featureless. Below T_2 a reflectance edge begins to develop at 140 cm^{-1}, which becomes quite sharp at 2K, as is shown in Fig. 14 for measurements made on the tape sample. Approximately forty phonon lines appear in the reflectance below T_2, and by 2K about 22 of these lines are very strong as can be seen in Fig. 15.

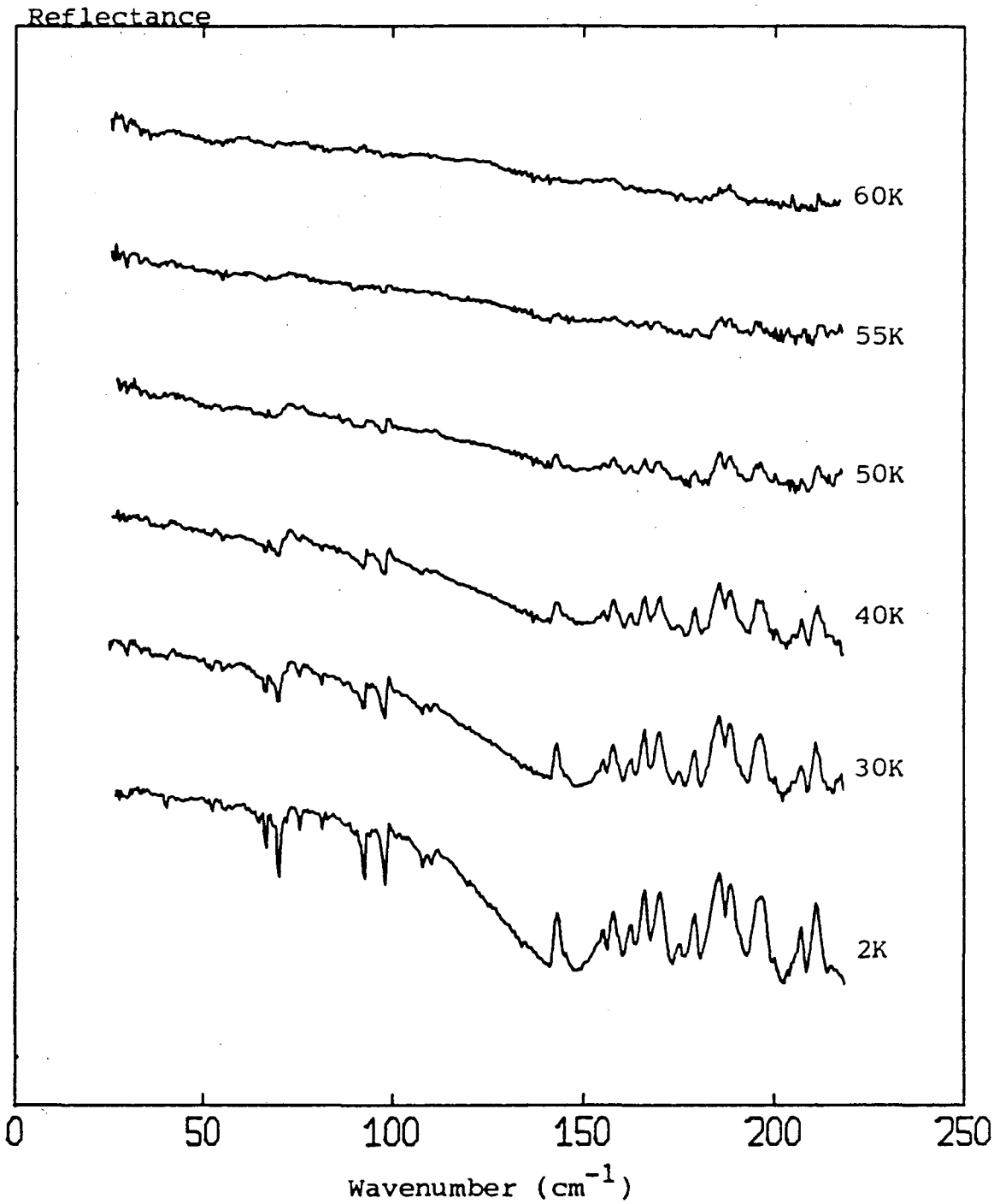

Fig. 14. Reflectance of tape sample of $NbSe_3$ as a function of temperature.

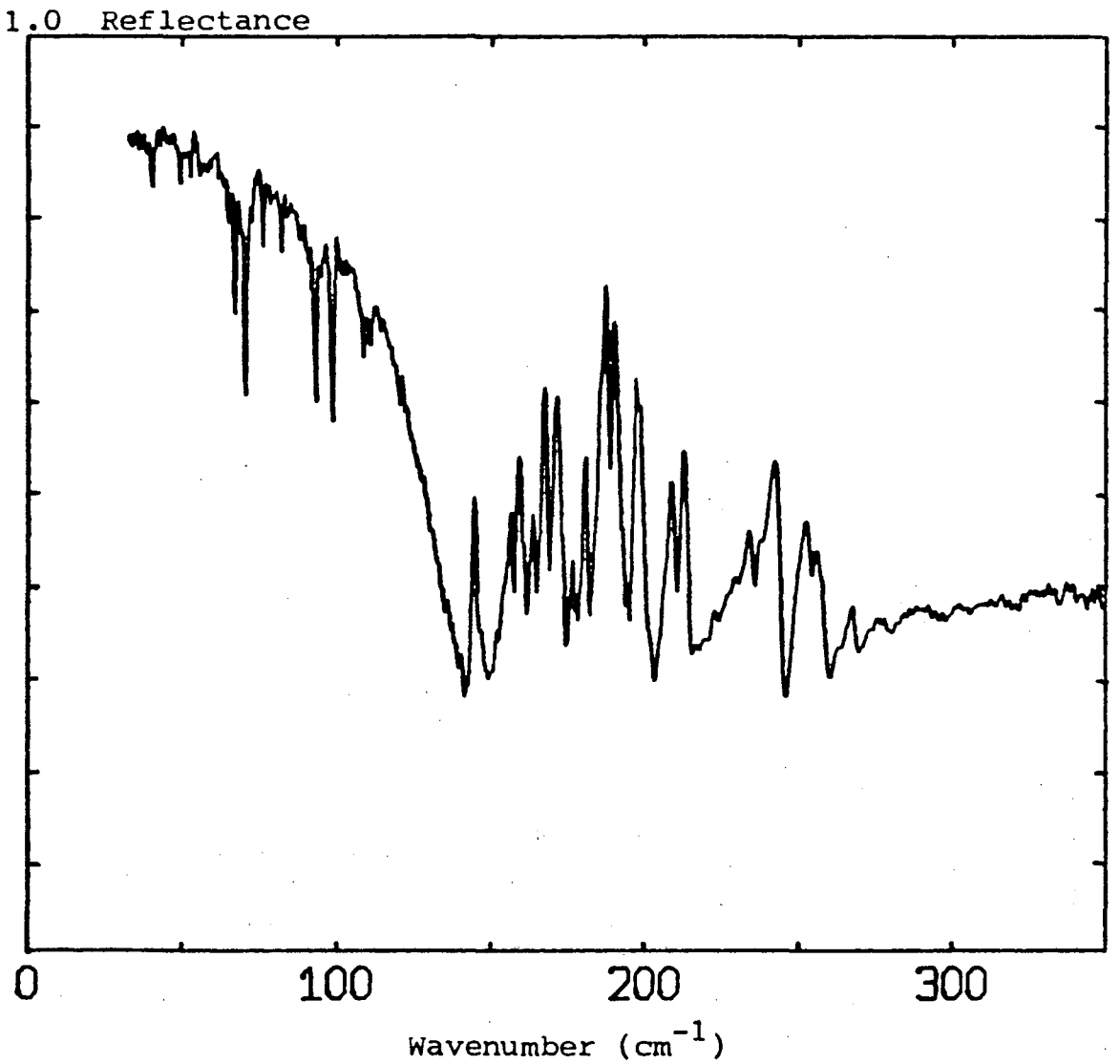

Fig. 15. Reflectance of $NbSe_3$ at 2K for radiation polarized parallel to the fiber axis.

The frequencies of these phonon lines are listed in Table 1. At frequencies below 100 cm^{-1} the lines are sharp absorptions with linewidths of ~1 cm^{-1}. Above 140 cm^{-1} the lines appear as sharp peaks and above ~200 cm^{-1} there is a noticeable broadening of the phonon linewidths. Many of the lines appear to be doublets.

Some of the phonon lines in Fig. 14 are weakly present in the reflectance spectrum at 60K above T_2. This, however, is due to inaccuracy of the measurement of the sample temperature. In the more accurate measurements of the $NbSe_3$ mesh in the sample can with exchange gas, all of the phonon lines disappear exactly at T_2. This is shown in Fig. 16. The temperature dependence of the intensity of individual phonon lines is shown in Fig. 17. The equation describing the fraction of carriers condensed in the T_2 CDW as a function of temperature[1] is also plotted.

There are eleven potentially IR-active phonons for light polarized parallel to the fiber axis in the undistorted lattice of $NbSe_3$. However, in good conductors like $NbSe_3$, phonons are generally unobservable in the FIR because of screening by the free carriers. In the distorted lattice, the optical phonons with a $\pm 2k_F$ wavevector are folded to the center of the Brillouin zone. These new zone center modes may form coupled modes with the CDW carriers called phase phonons if they satisfy symmetry requirements. In $NbSe_3$, only the 24 A_g modes of the undistorted lattice have the correct symmetry for first-order coupling to the condensed carriers. The number of the strong phonon modes we see in the FIR spectrum of $NbSe_3$ is in good agreement

Table 1: Frequencies of phonon lines in infrared spectrum of $NbSe_3$

Frequency	Amplitude	Frequency	Amplitude
35 cm^{-1}	weak (w)	152	w
39	w	155	s
41	medium(m)	158	s
51	m	162	s
53	m	166	s
61	w	169	s
63	w	175	m
66	strong(s)	180	s
67	w	185	s
69	s	188	s
75	m	195	s
81	m	200	m
92	s	206	s
93	w	209	s
97	s	215	w
100	w	232	m
107	m	236	w
109	m	240	s
119	w	251	s
124	w	254	s
126	w	266	m
142	s	300	w

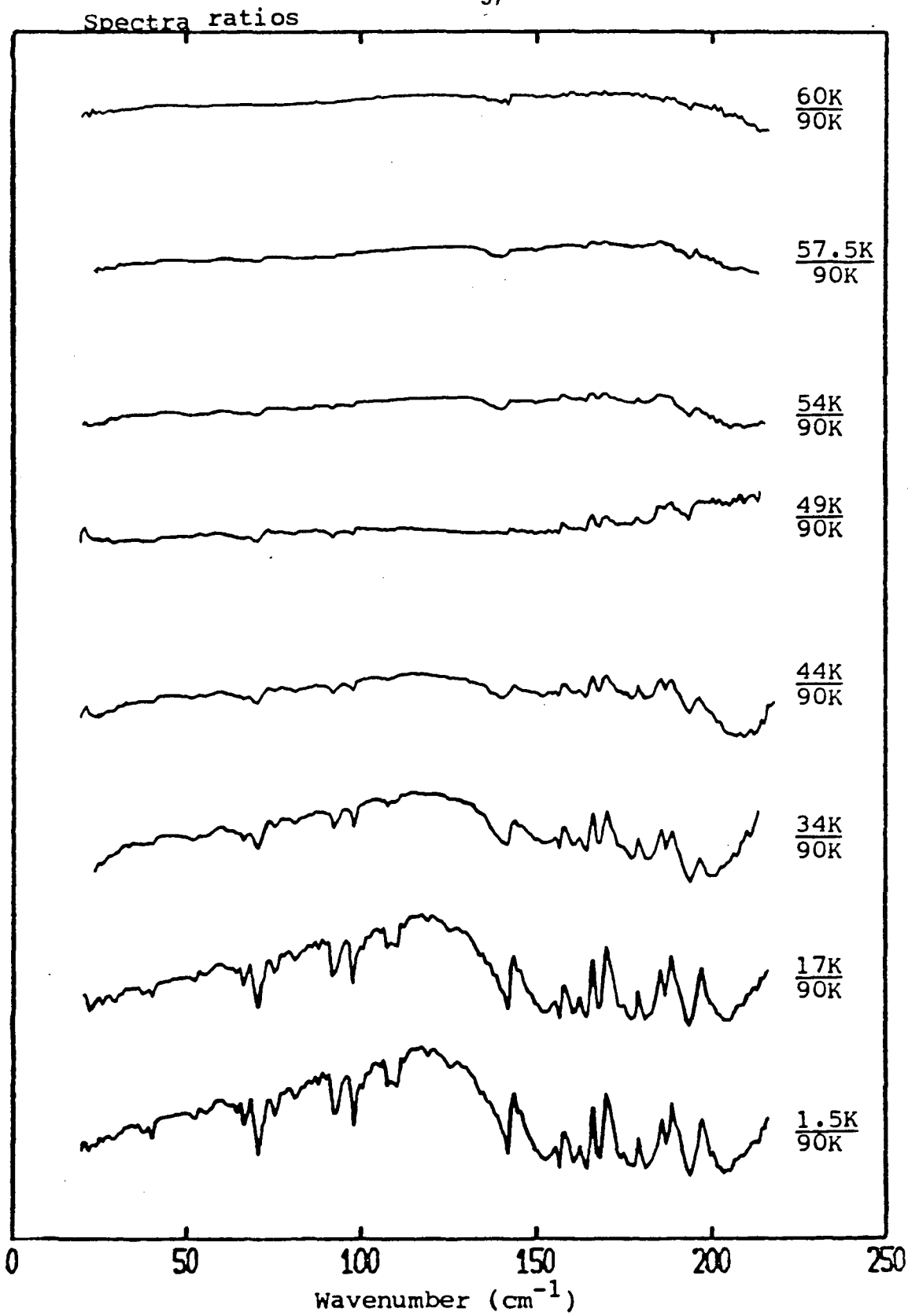

Fig. 16. Ratios of spectra of the radiation transmitted through $NbSe_3$ mesh.

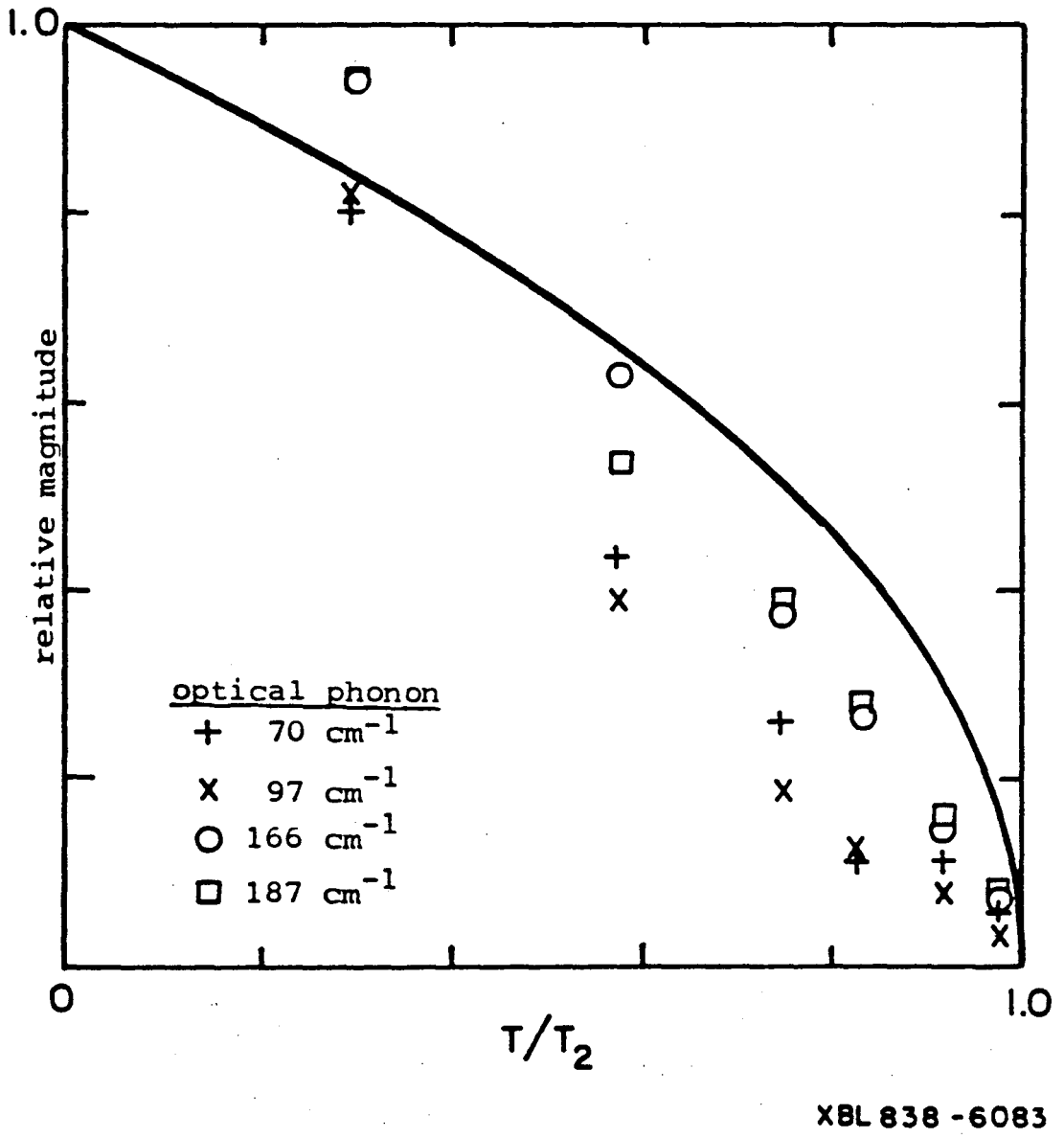

Fig. 17. Temperature dependence of the magnitude of the reflectance peaks of the optical phonons in $NbSe_3$, from the data in Fig. 16.

with this number of A_g modes. The many weaker phonons in the FIR spectrum may be due to coupling to $\pm 4k_F$ optical phonons, or to phonons which acquire A_g symmetry only in the distorted lattice. Because these phonons begin to appear in the FIR spectrum only below T_2, we believe that these are phase phonons coupled to the T_2 CDW. It is not immediately obvious why the phonons do not seem to couple to the T_1 CDW and appear in the FIR spectra above T_2 as well as below it. Perhaps this indicates that there is another symmetry relation which forbids coupling between the phonons and the T_1 CDW, or which forbids IR-activity for such coupled modes.

The optical constants for $NbSe_3$ at 2K were obtained by a Kramers-Kronig analysis of the reflectance. $\sigma_1(\omega)$ is shown in Fig. 18, and $\epsilon_1(\omega)$ is shown in Fig. 19. The high frequency extrapolation used in the Kramers-Kronig transform was of the ω^{-s}, ω^{-4} type described in Appendix A. The adjustable parameter, ω_c, was chosen equal to 100,000 cm^{-1}, although varying this parameter over three orders of magnitude was found to change the computed conductivity by a factor of ≤ 2 and make no qualitative change in its frequency dependence.

Standard models for the frequency dependence of the conductivity for free and condensed carriers were used to fit the estimate of the conductivity. A Drude function was used to model the oscillator strength of the free carriers. The oscillator strength of the condensed carriers was modelled by the theories of Lee, Rice, and Anderson,[2] and of M. J. Rice.[3] These models are discussed in detail in Appendix A. The resulting fit to $\sigma_1(\omega)$ is shown in

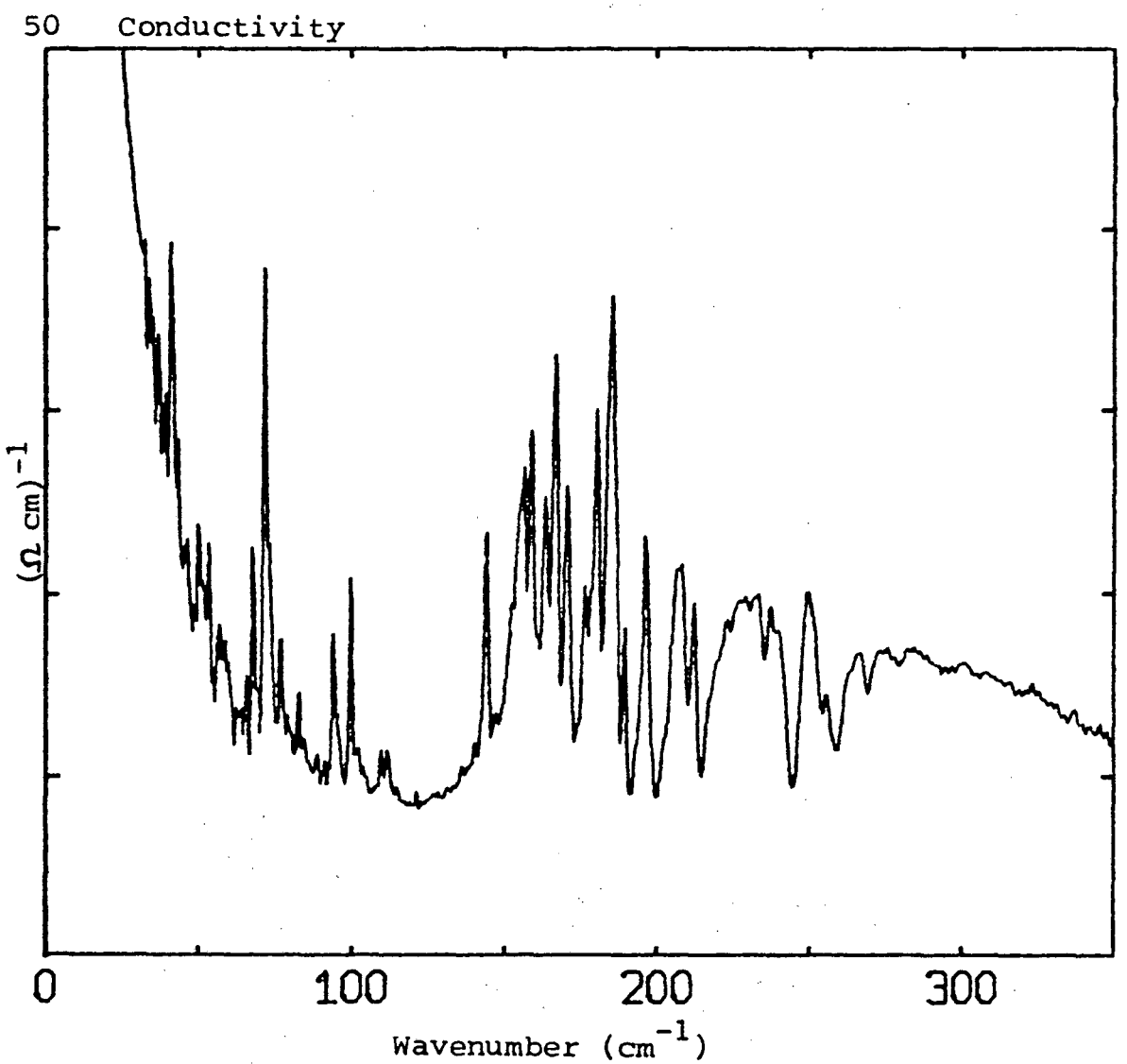

Fig. 18. $\sigma_1(\omega)$ from a Kramers-Kronig analysis of the reflectance of $NbSe_3$ at 2K for radiation polarized parallel to the fibers.

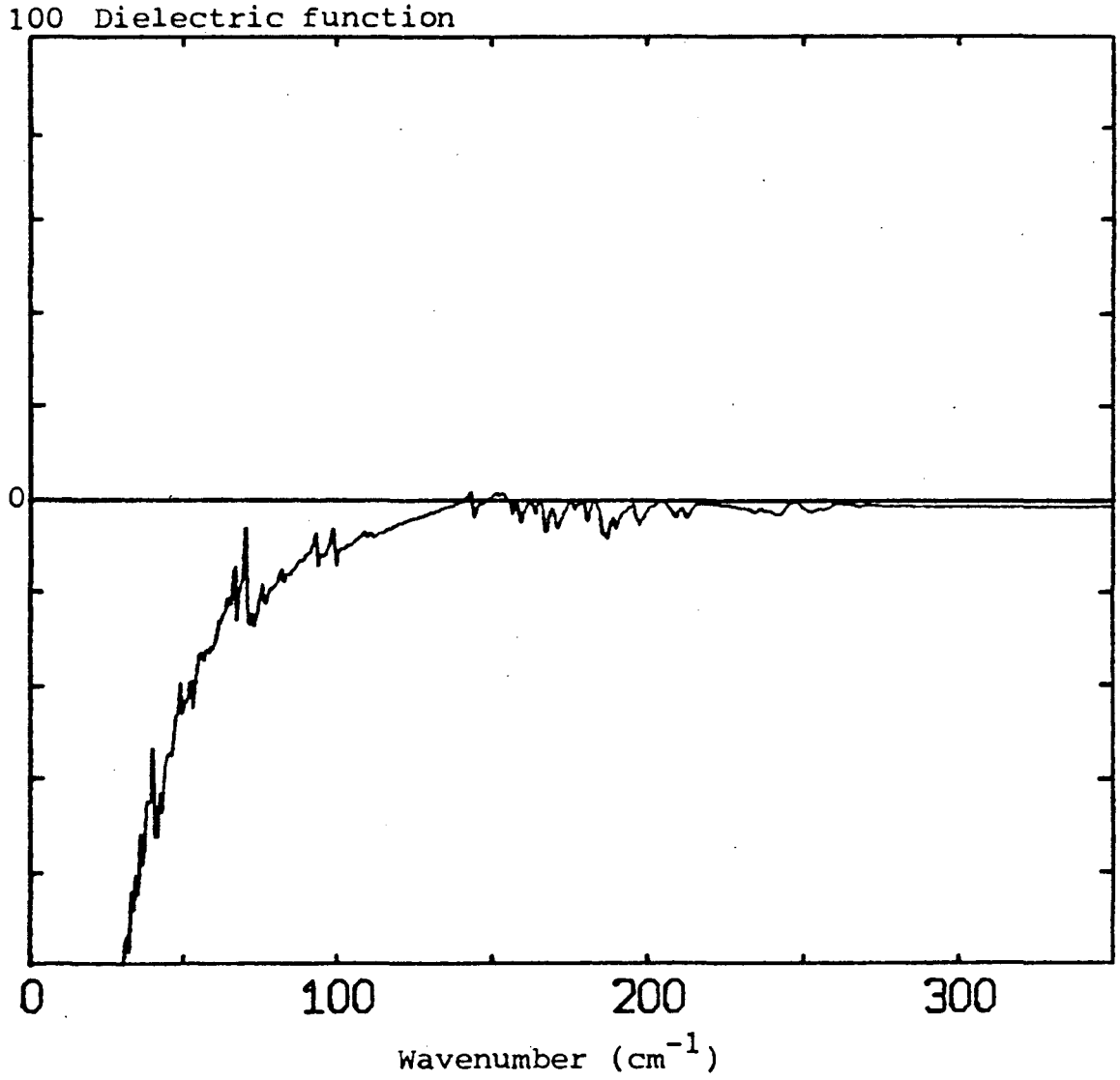

Fig. 19. $\epsilon_1(\omega)$ from a Kramers-Kronig analysis of the reflectance of $NbSe_3$ at 2K for radiation polarized parallel to the fibers.

Fig. 20, and to $\epsilon_1(\omega)$ is shown in Fig. 21. The reflectance calculated from this fit is shown in Fig. 22. The parameters used in the fit are given in Table 2, and we discuss these now in detail.

Phase phonons and CDW energy gap: The substantial broadening of phonon linewidths above ~200 cm^{-1} is evidence for a CDW energy gap occurring below this frequency, allowing the phonons to decay through creation of electron-hole pairs. These phonons also give rise to Fano-like interference dips in the conductivity, as can be seen from Fig. 18. This is additional evidence for a CDW energy gap and a single-particle continuum in the conductivity above the gap, present at ~200 cm^{-1}. Finally, there is a general rise in $\sigma_1(\omega)$ above ~120 cm^{-1}, and by ~200 cm^{-1} it is clear that this rise is not due solely to the phonon modes. We interpret this additional contribution to the conductivity as a single-particle continuum above a CDW energy gap. It could not arise from errors in our measurements due to diffuse scattering, which would have the effect of reducing the conductivity in this region. We conclude that there is a CDW energy gap with $120 \leq 2\Delta \leq 190$ cm^{-1}. This result can be compared with the mean field value $2\Delta = 3.5\ k_B T_c = 140$ cm^{-1} for the T_2 CDW.

The CDW energy gap has been chosen at 190 cm^{-1} for the conductivity fit in Fig. 20. While our choice of an energy gap at 190 cm^{-1} is not unique, fitting the data with an energy gap at lower frequencies degrades the fit. An energy gap of this size when related to the T_2 CDW leads to a prefactor in the mean field gap equation of 4.65 rather than 3.5. Various theories have been proposed which lead

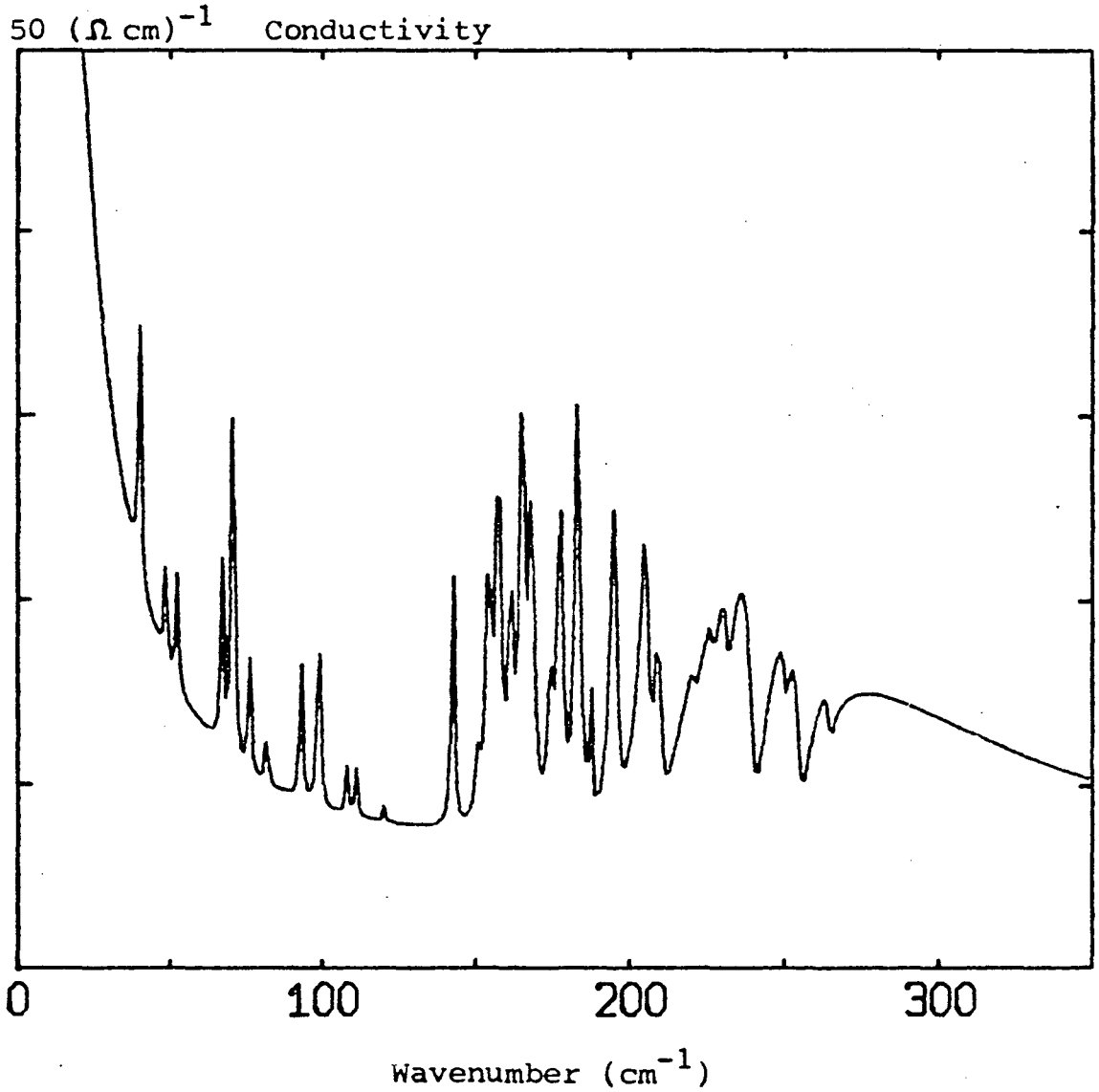

Fig. 20. Fit to the conductivity, $\sigma_1(\omega)$, of $NbSe_3$ at 2K.

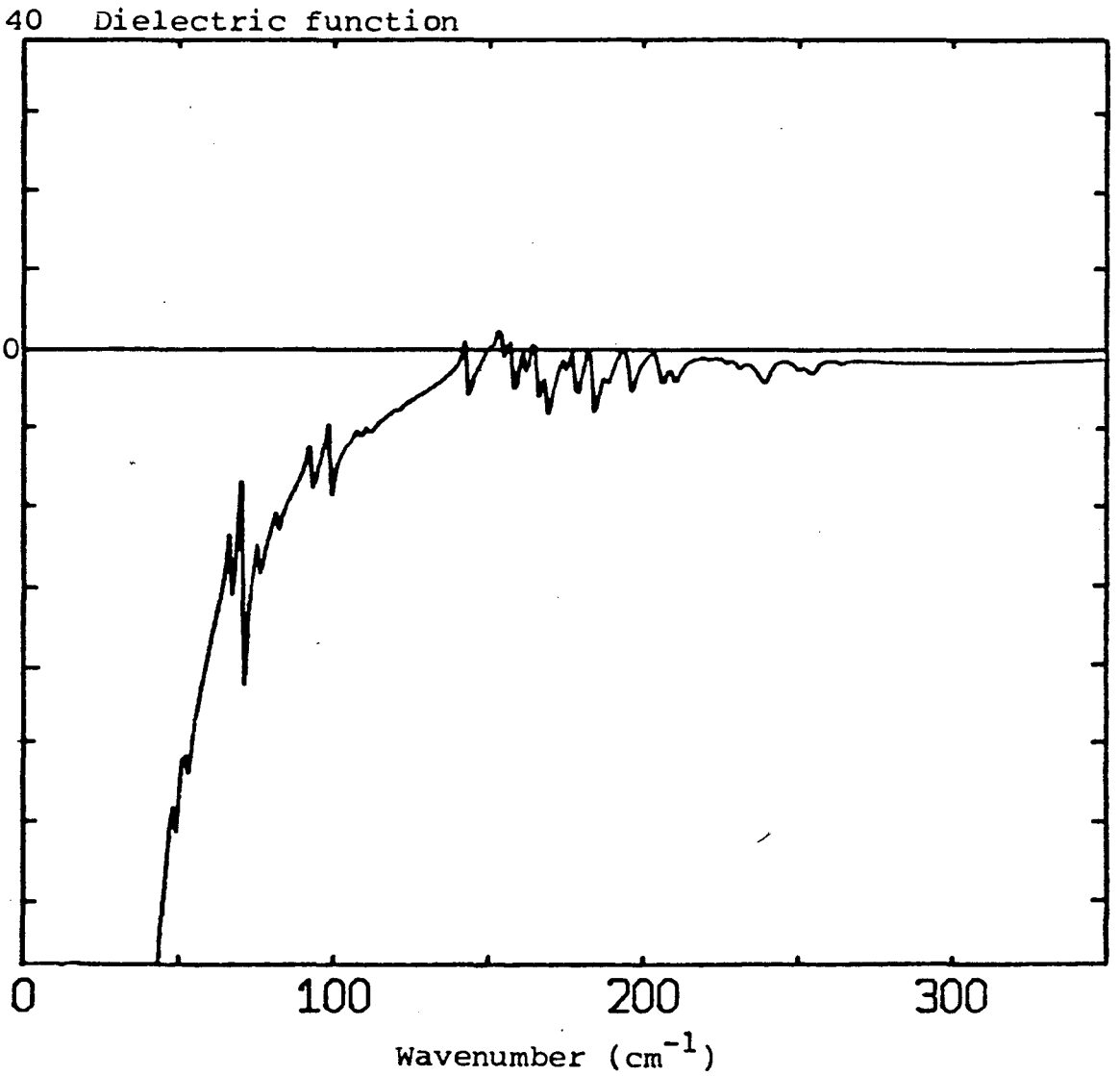

Fig. 21. Fit to the dielectric function, $\epsilon_1(\omega)$, of $NbSe_3$ at 2K.

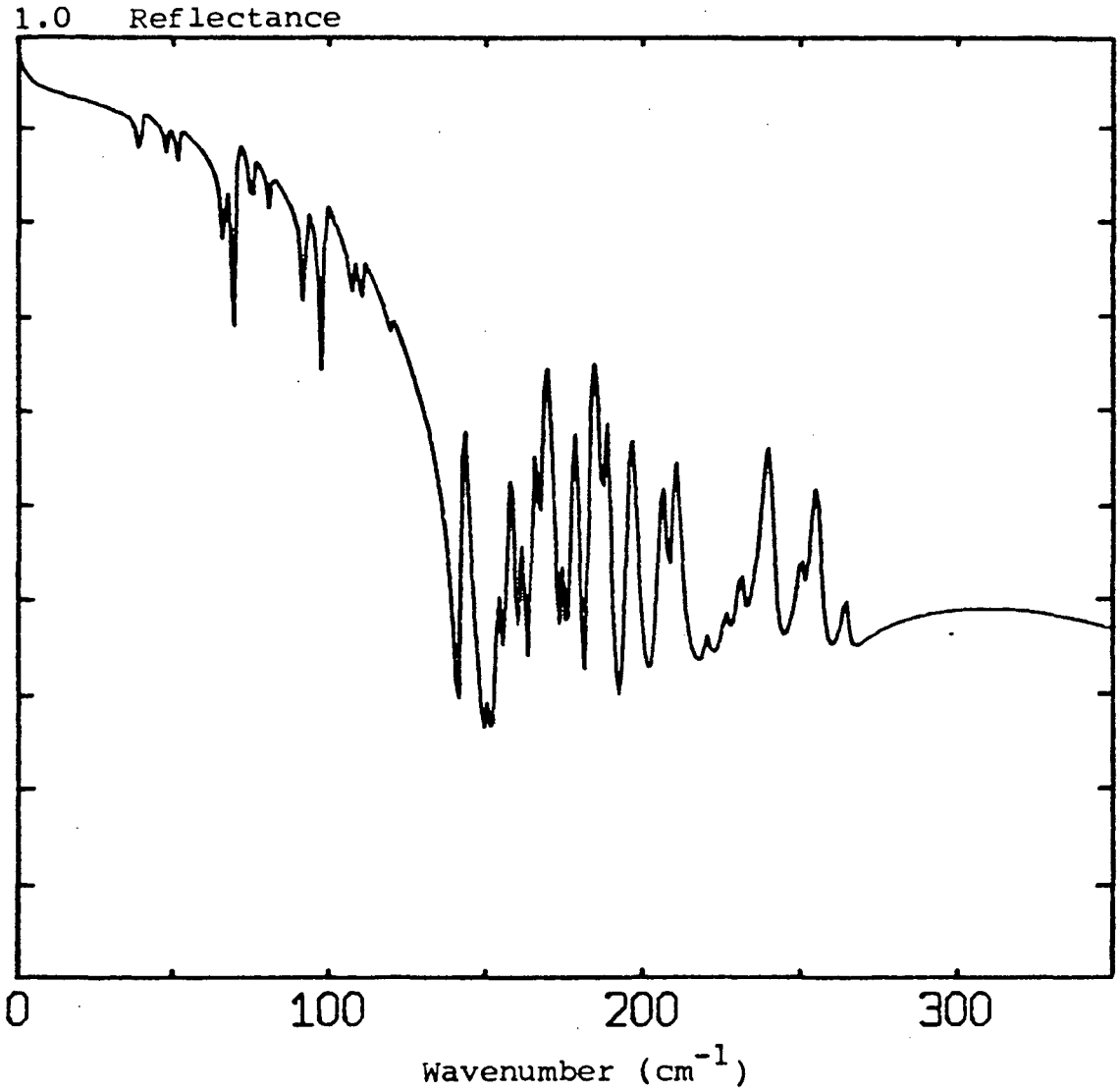

Fig. 22. Reflectance calculated from the fit to the conductivity of $NbSe_3$ at 2K.

Table 2. Parameters used for conductivity fit in Fig. 22. CDW energy gap = 190 cm^{-1}. Oscillator strengths expressed as n/m* of:

condensed carriers (pinned mode, phase phonons, and single-particle continuum) = 1.4×10^{18} cm^{-3}/m_o

pinned mode = 2.8×10^{17} cm^{-3}/m_o

free carriers = 1.2×10^{18} cm^{-3}/m_o

Relaxation time of pinned mode and free carriers = 4.4×10^{-13} s.

Background dielectric constant = 1.4.

A constant term, $\sigma_o = 6$ $(\Omega cm)^{-1}$, has been added to improve the fit slightly, but which is probably not physically significant.

Phonon Freq. ν_n	Coupling Constant λ_n	Line-Width ν_{rn}	Phonon Freq. ν_n	Coupling Constant λ_n	Line-Width ν_{rm}
40 cm^{-1}	.25	1 cm^{-1}	162	.0056	2
48	.057	1	166	.008	2
52	.057	1	170	.02	2
67	.044	1	175	.004	2
71	.141	1	179	.0017	2
76	.036	1	185	.019	2
81	.014	1	188	.006	1
93	.0216	1	197	.01	2
99	.032	1	207	.005	2
108	.0046	1	211	.0075	2
111	.0046	1	221	.0005	2
120	.001	1	227	.0005	2
143	.0075	1	232	.011	2
151	.0014	2	241	.0065	2
154	.002	2	251	.001	2
155	.0027	2	256	.005	2
158	.01	2	265	.001	2

to prefactors larger than the mean field result. A theory originally developed to describe SDW transitions,[4] which has been applied to the CDW energy gaps in $NbSe_3$,[5] predicts an energy gap equation of the form

$$2\Delta = 3.5 \left[\frac{v_e + v_p}{2\sqrt{v_e v_p}} \right] k_B T_c$$

where v_e and v_p are the velocities at the Fermi surface of the electron and hole bands, respectively. According to this theory, an energy gap in $NbSe_3$ at 190 cm^{-1} would indicate that one of the carriers has a Fermi velocity at 2K which is 2.2 times larger than the Fermi velocity of the other carrier.

Another theory[6] for materials with a two-dimensional energy band and saddle points at the Fermi level predicts a prefactor for the CDW energy gap equation of >4.4. In the absence of band structure calculations for $NbSe_3$, however, it is impossible to determine the applicability of this theory.

Electron-phonon scattering effects may also increase the prefactor[7] above that calculated from the mean field theory. Finally, mean field calculations in a tight-binding approximation[8] (which is probably not applicable to $NbSe_3$) predict a prefactor larger than 3.5 in the energy gap equation if the band is less than half-filled.

The size of the CDW energy gap is related to the size of the coupling constants between the CDW carriers and the optical and acoustic phonons. From the estimates of the CDW carrier-optical phonon coupling constants given in Table 2, we find a total coupling constant to the optical phonons of ~0.8. However, the mean field equation[9] $2\Delta = 16\ \epsilon_F e^{-1/\lambda}$ leads to an estimate of the total coupling constant which is about an order of magnitude larger. Therefore, the CDW state in $NbSe_3$ is primarily stabilized by the static lattice distortion from the soft acoustic phonon, rather than by the optical phonons. Because of this, the renormalized frequencies of the optical phonons when coupled to the CDW carriers to form phase phonons differ very little from the frequencies of the bare optical phonons.

Our identification of the phonon lines in the FIR spectrum of $NbSe_3$ as resulting from phase phonons could potentially be verified by low temperature Raman measurements. Below T_2 there should be a Raman-active amplitude phonon mode for each IR-active phase phonon (see Fig. 6). The frequency difference between a phase phonon and its associated amplitude mode is directly related to the CDW carrier-optical phonon coupling constant,[10] and could be used as an independent check of the estimates of the coupling constants from the FIR fit.

It is interesting to note that the Fano interference effect has apparently never been seen before in inorganic CDW conductors. For this effect to be seen, the CDW energy gap must lie in the frequency

range of the phonons. The required low CDW transition temperature occurs in $NbSe_3$, but in no other inorganic CDW compounds of which we are aware.

It is also interesting that most, if not all, of the phonons in the FIR spectrum of $NbSe_3$ appear as doublets. An interesting speculation, for which we are indebted to Professor N. Bartlett, is that the doublet structure might arise from the absence of the inversion center in the low temperature distorted state of the crystal lattice.

Pinned mode and free carriers: Below 100 cm^{-1} there is a rise in $\sigma_1(\omega)$ which we believe is the tail of the contribution to the conductivity from the CDW pinned mode and from the free carriers. A simple argument can be used to obtain the relaxation time and oscillator strength of free carriers and pinned mode. Assuming that the conductivity measured at microwave frequencies relaxes as $(\omega\tau)^{-2}$ in the FIR, and that the dc conductivity of our $NbSe_3$ fibers at 2K is $\sim 10^5$ $(\Omega cm)^{-1}$, then the FIR reflectance minimum of <40 percent at 140 cm^{-1} requires a relaxation time at 2K of $> 3 \times 10^{-12}$s. From this result, we can estimate the combined oscillator strength of the pinned mode and the free carriers. It is convenient to express the oscillator strength in terms of the ratio of the carrier concentration to the band mass. From the equation $n/m^* \approx \sigma_{dc}/(\tau e^2)$, we get $n/m^* < 2 \times 10^{20}$ cm^{-3}/m_o, where m_o is the free electron mass.

An alternative, and perhaps better, method for estimating the total low frequency oscillator strength is to integrate the area under

the curve of $\sigma_1(\omega)$. Errors in the reflectance normalization and Kramers-Kronig analysis lead to the major source of error in the final result, but an upper limit can be placed upon the total oscillator strength in the low frequency mode in the following way. First we assume that there is a large normalization error in the reflectance data, and that the reflectance below 60 cm^{-1} is actually ~100 percent and that the strong phonon line at 185 cm^{-1} also reaches a peak of ~100 percent. A linear correction for the normalization error can then be made in the reflectance data, and the result is shown in Fig. 23. The overall reflectance is considerably increased by this procedure, and will therefore tend to increase the oscillator strength at low frequencies. Next, the Kramers-Kronig analysis of the reflectance is performed, and an adjustable parameter is chosen which maximizes the oscillator strength at low frequencies. The result for $\sigma_1(\omega)$ with $\omega_c = 100{,}000\ cm^{-1}$ is shown in Fig. 24. The oscillator strength at low frequencies, obtained by integrating the area under the conductivity curve for this modified data, is $<2 \times 10^{19}\ cm^{-3}/m_o$. A slightly larger value for the oscillator strength at low frequencies might be possible by choosing a different reflectance extrapolation in the Kramers-Kronig analysis. Nevertheless, the total oscillator strength at low frequencies is almost certainly $<5 \times 10^{19}\ cm^{-3}/m_o$. This corresponds to a relaxation time $>10^{-11}$s.

The modelled fit to the conductivity gives a relaxation time for this low frequency mode of 4.4×10^{-13}s. This number is smaller than the limits set by the previous two estimates. The estimate of the

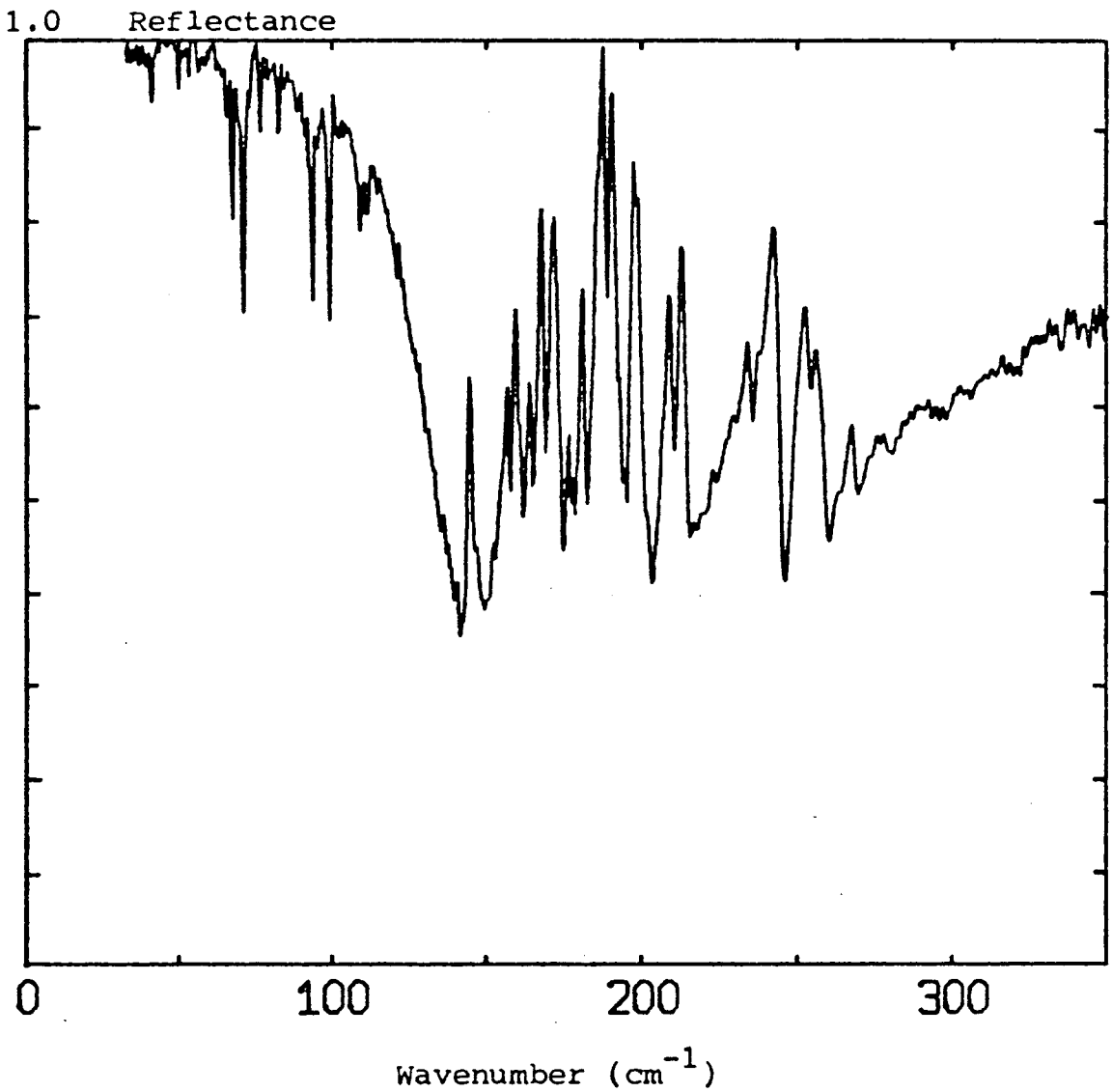

Fig. 23. Reflectance of $NbSe_3$ at 2K for radiation polarized parallel to the fiber axis. This spectrum has been corrected for an assumed large error in the normalization.

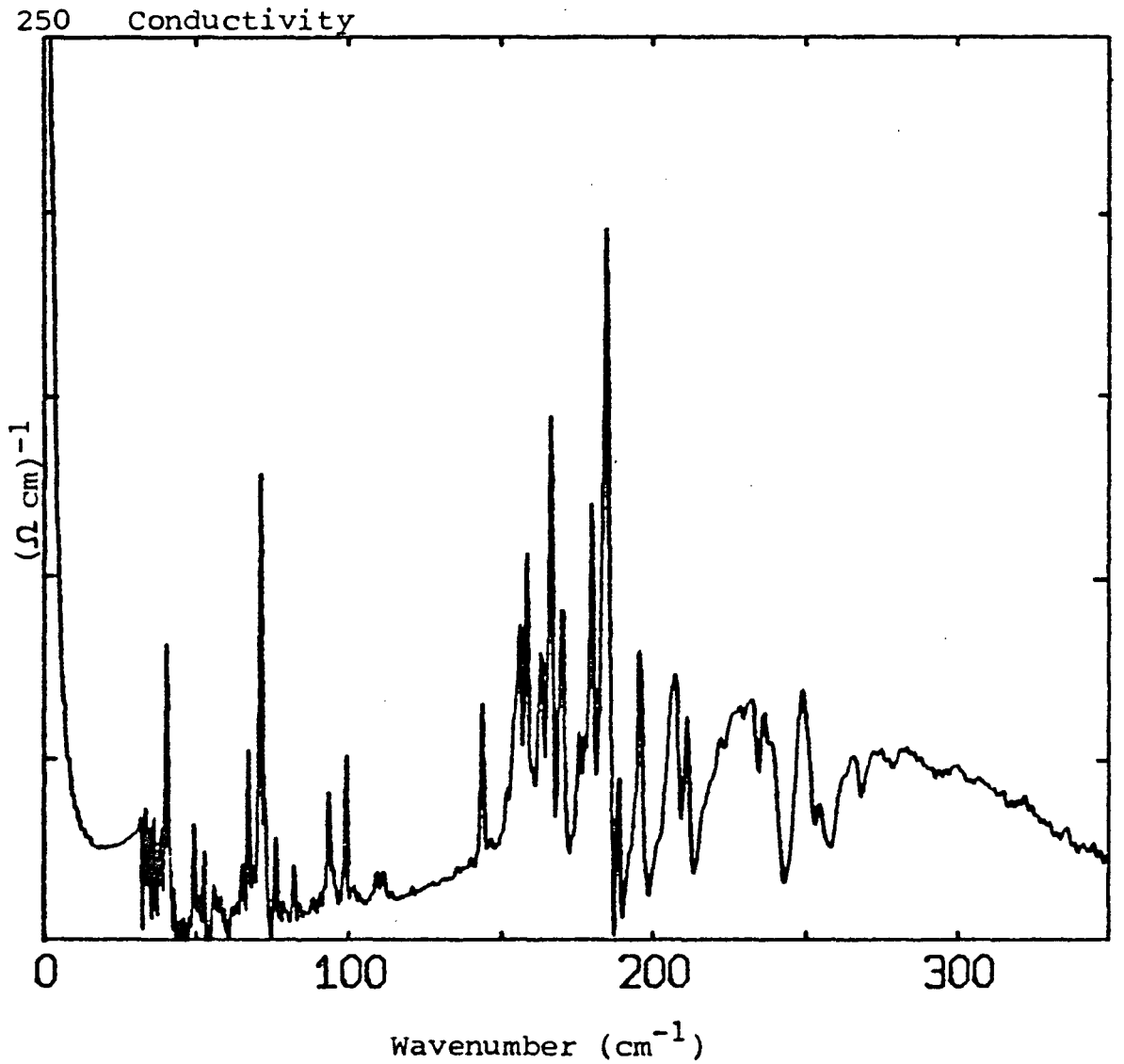

Fig. 24. $\sigma_1(\omega)$ from a Kramers-Kronig analysis of the modified reflectance of $NbSe_3$ shown in Fig. 25.

relaxation time from the fit to the conductivity, however, is sensitive to errors in the normalization of the reflectance at low frequencies. The oscillator strength which is obtained from the fit to the conductivity is 1.8×10^{18} cm^{-3}/m_o. Errors in the normalization of the reflectance could make this number too small by about a factor of five. The results of these estimates are summarized in Table 3.

These values can be compared to other estimates of the carrier concentration in the literature (see Table 3). The two-band model[11] of magnetotransport data for $NbSe_3$ estimates a total concentration of free carriers which remain uncondensed at temperatures well below T_2 to be 7×10^{18} cm^{-3}. This quantity seems to be consistent with our FIR data. However, similar estimates based upon the analysis of narrow band noise measurements,[12,13] assuming that the relevant periodicity is the CDW wavelength and that there are $\geq 10^{21} cm^{-3}$ carriers at room temperature, yield concentrations $\geq 5 \times 10^{20}$ cm^{-3}. Unless one is willing to accept band masses >10 m_o, the FIR data are inconsistent with the estimates based on the noise measurements. This disagreement suggests that the relevant periodicity in the analysis of the narrow band noise may not be the CDW wavelength as is generally, but not universally,[14-17] assumed. If the concentration of free carriers at room temperature is in fact $\sim 10^{21}$ cm^{-3}, then the relevant periodicity associated with the narrow band noise must be half of a CDW wavelength or smaller to leave a free carrier concentration of $< 5 \times 10^{19}$ cm^{-3} below T_2. On the other hand, if the CDW

Table 3. Estimates of oscillator strengths, relaxation times, and carrier concentrations discussed in the text.

basis of estimate	combined oscillator strength of pinned mode and free carriers at 2K	relaxation time at 2K
Reflectance at 140 cm^{-1}	$<2 \times 10^{20}$ cm^{-3}/m_o	$>3 \times 10^{-12}$s
sum rule	$<5 \times 10^{19}$ cm^{-3}/m_o	$>10^{-11}$s
fit to the conductivity	1.8×10^{18} cm^{-3}/m_o	4.4×10^{-13}s

basis of estimate	concentration of free carriers at 2 K	concentration of carriers condensed in T_2 CDW at 2 K
two-band model of magnetotransport measurements ref. 11	7×10^{18} cm^{-3}	2×10^{19} cm^{-3}
narrow band noise measurements: ref. 12	$\sim 10^{21}$ cm^{-3}	$1 - 1.5 \times 10^{21}$ cm^{-3}
ref. 13	$\geq 5 \times 10^{20}$ cm^{-3}	$0.62 - 1.96 \times 10^{20}$ cm^{-3}

wavelength is indeed the relevant periodicity in the analysis of the narrow band noise measurements, then the free carrier concentration in $NbSe_3$ at room temperature must be $<10^{21}$ cm^{-3}.

Pinned mode and single-particle continuum: In the CDW state, the $\pm 2k_F$ acoustic phonons form a collective mode with the CDW carriers called the phason. The phason corresponds to phase oscillations of the CDW at the pinning frequency and contributes to the ac conductivity. According to the theory of Lee, Rice, and Anderson,[2] the fraction of the oscillator strength of the condensed carriers which appears in the phason is determined by the ratio, m^*/M_F, of the carrier band mass to the effective mass per condensed carrier of the CDW. Although not explicitly discussed, the simple classical harmonic oscillator model[13] of CDW transport gives a similar result. By contrast, the tunneling model[18] of CDW transport attributes most of the ac conductivity of the pinned CDW to photon assisted tunneling. Only a very small additional contribution is required from a classical phase mode to fit the experimental data for $NbSe_3$.

If the frequency dependence of the conductivity of the condensed carriers in $NbSe_3$ can be modelled by the Lee, Rice, and Anderson[2] and M.J. Rice[3] theories, then a significant fraction of the oscillator strength of the CDW carriers must appear in the pinned mode to eliminate a strong peak in σ_1 at the energy gap, which we do not observe. If such a strong peak were in fact present, it would give rise to a Reststrahl band in the FIR reflectance spectrum, which would be obvious in our data in spite of any normalization problems. For

the conductivity fit shown in Fig. 20, 20% of the oscillator strength of the CDW carriers appears in the pinned mode. Fitting the data with an energy gap smaller than 190 cm^{-1} requires that an even larger fraction of the oscillator strength of the condensed carriers appear in the pinned mode. If the oscillator strength in the pinned mode appears in the phason as suggested by the classical model of CDW transport,[13] rather than primarily in photon assisted tunneling, then we obtain a CDW effective mass of ~5m* from the Lee, Rice, and Anderson theory.[2] This is much smaller than the effective mass usually assumed for CDW's, which is ~10^3m*.

The ratio of the total condensed carrier concentration to band mass from the fit is 1.4 x 10^{18} cm^{-3}/m_o. Errors in the normalization of the data could make this value too small by about a factor of five. The estimate of the CDW carrier concentration for the T_2 CDW from the two-band model[11] of magnetotransport data is 2 x 10^{19} cm^{-3}, while estimates from analysis of narrow band noise measurements[12,13] range from 0.62 x 10^{20} cm^{-3} to 1.5 x 10^{21} cm^{-3}. This may indicate either that there are very large carrier band masses, or that a substantial amount of the oscillator strength of the T_2 CDW carriers occurs at frequencies above 350 cm^{-1} and is not being included in our extrapolation of the available FIR data. Alternatively, the large difference between the values obtained from the FIR fit and those obtained from other methods could possibly indicate an unrecognized error in approximating our sample surface as a single crystal and analyzing our data accordingly.

However, the small condensed carrier concentration to band mass ratio obtained from the FIR fit is in reasonable agreement with an estimate of this quantity obtained from the tunneling model. Measurements of the rf conductivity of $NbSe_3$ at 32K, which have been analyzed in terms of the tunneling model,[18] can be scaled to compare with our data at 2K. Interpreting the 32K measurements using the tunneling model gives a peak conductivity for the phason which is 20% of the dc conductivity, and a relaxation frequency of the phason of $\sim 10^8$ Hz. For our $NbSe_3$ fibers at 32K, we estimate $\sigma_{dc} = 1.5 \times 10^4\ (\Omega cm)^{-1}$. For a Lorentzian form of the phason with the above parameters, the oscillator strength at 32K, expressed as a carrier concentration to effective mass ratio, is $\sim 6.7 \times 10^{15}\ cm^{-3}/m_o$. For a CDW effective mass of $10^3 m^*$, the total oscillator strength of the condensed carriers is $\sim 6.7 \times 10^{18}\ cm^{-3}/m_o$ at 32K. If we use the approximate relation[1] $n_c/n = \sqrt{1 - T/T_c}$ to scale this result for comparison to the 2K data, we obtain $\sim 10^{19}\ cm^{-3}/m_o$. This quantity is seven times larger than that obtained from the FIR fit. Considering the uncertainties in our estimates of the peak conductivity and relaxation frequency for the phase mode, as well as the uncertainties in the FIR fit, we believe that the FIR fit is in reasonable agreement with the tunneling model. Essentially exact agreement can be obtained with the FIR fit by assuming a CDW effective mass of ~140 m*, which is not unreasonable.

The detailed data analysis up to this point has involved the reflectance spectrum of the $NbSe_3$ tape sample at 2K. There are no

theories at present for modelling the conductivity of condensed carriers at finite temperatures. As the temperature increases, condensed carriers will be thermally excited out of the CDW to become free carriers. As the concentration of condensed carriers decreases, the total oscillator strength of the condensed carriers (pinned mode, phase phonons, and single-particle continuum) will also decrease. As the free carrier concentration increases, the oscillator strength in the low frequency mode from the free carriers will also increase. The relaxation time of the free carriers and pinned mode will decrease because there are more phonons and free carriers available for scattering processes. The size of the CDW energy gap also decreases with increasing temperature, and according to mean field theory it should have the same functional temperature dependence as that of a superconducting energy gap.

The reflectance of the tape sample at 40K is shown in Fig. 25. If we attempt to model this reflectance by using the equations for the conductivity of the condensed carriers (which really are only valid at absolute zero) and using the parameters obtained from the 2K fit with the changes described above, we compute a reflectance as shown in Fig. 26. Not surprisingly, the calculated reflectance at 40K is in poor agreement with the measured reflectance. In particular, the phonons with frequencies near the 160 cm^{-1} energy gap at 40K are greatly distorted in the computed reflectance. This is caused by the sharp onset of conductivity from the single-particle continuum above the energy gap in the model equations. In reality, however, at finite

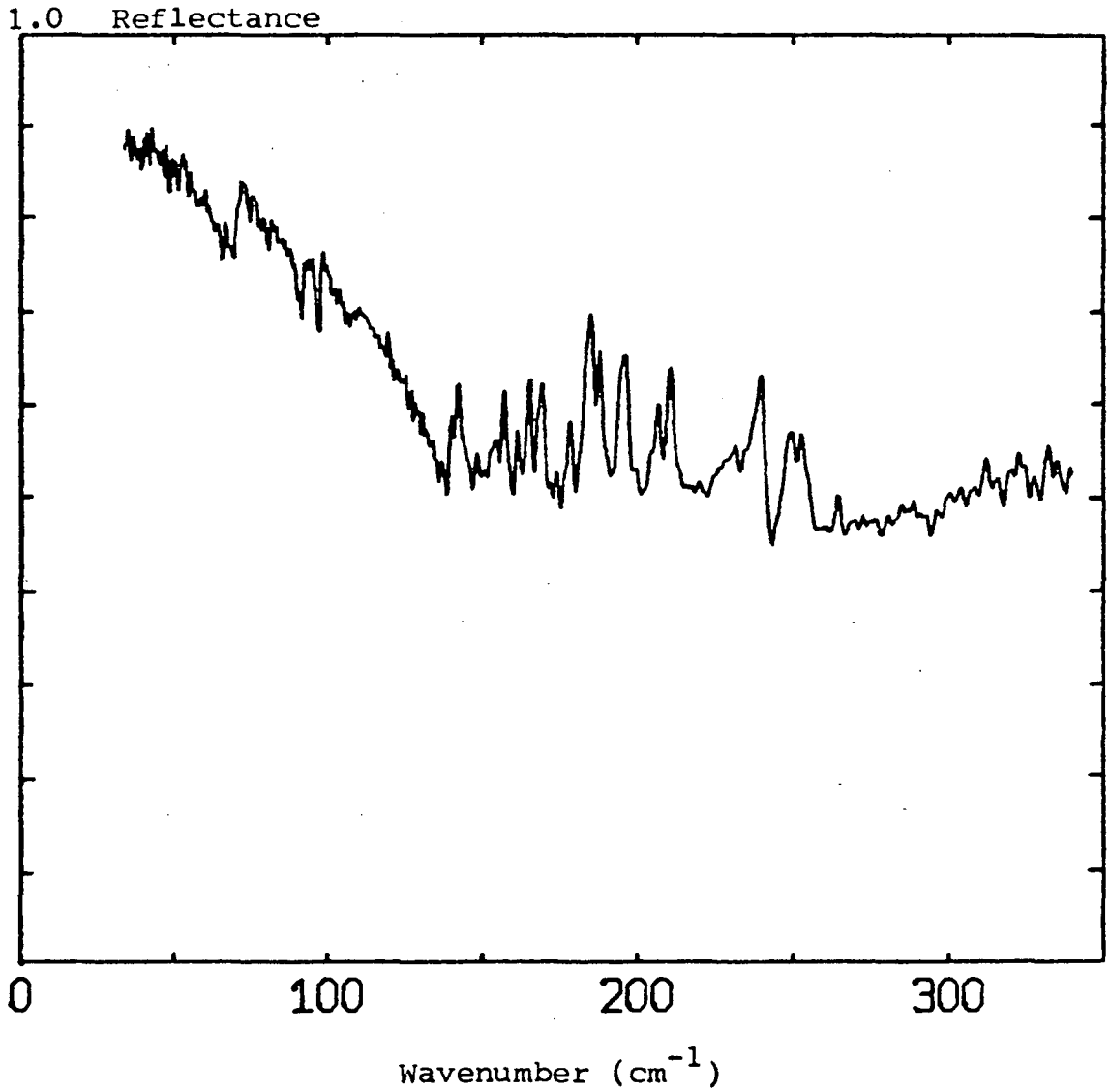

Fig. 25. Reflectance of $NbSe_3$ at 40K for radiation polarized parallel to the fiber axis.

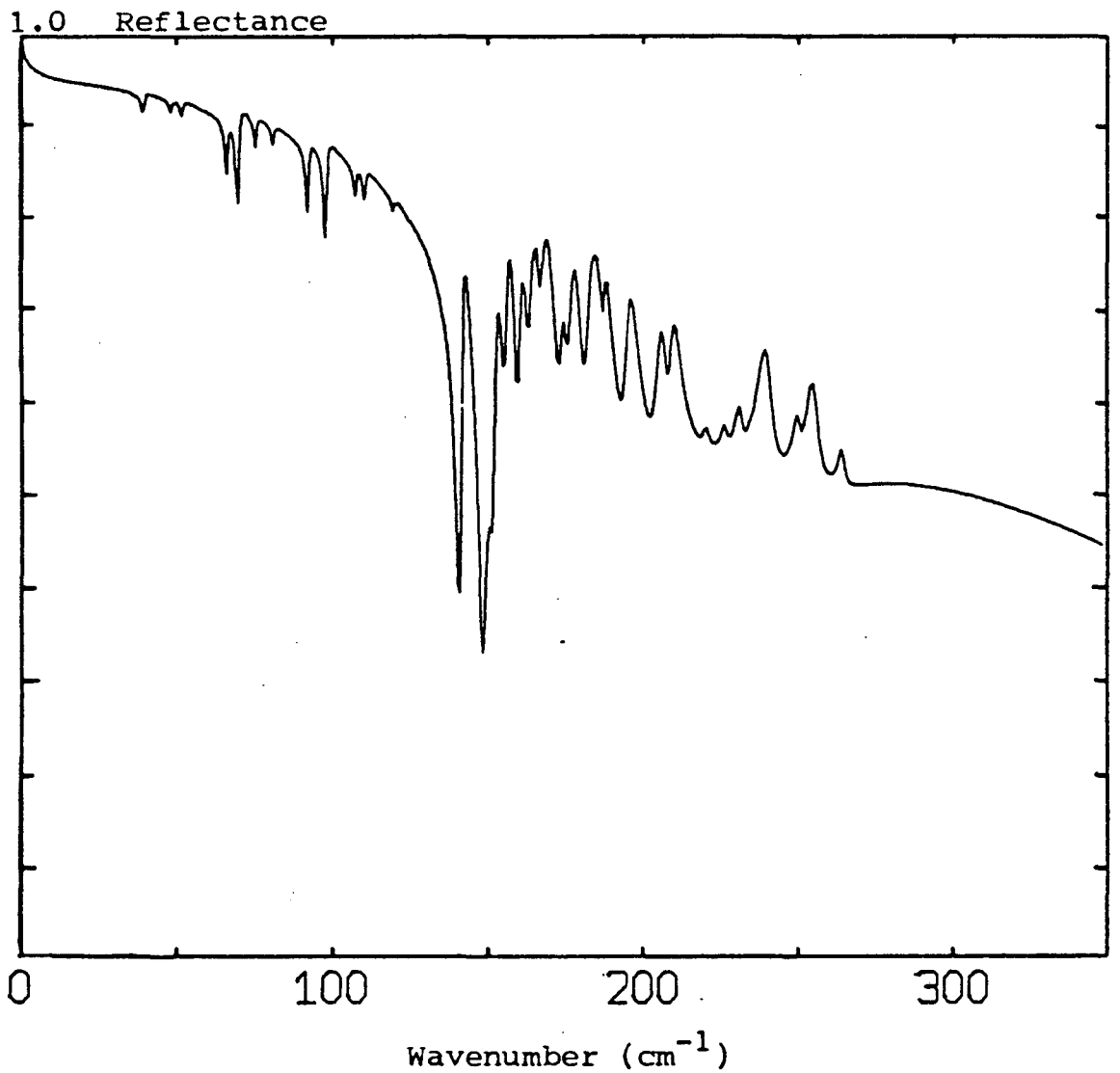

Fig. 26. Computed reflectance of $NbSe_3$ at 40K using the parameters obtained from the fit to the conductivity at 2K.

temperatures there will be a finite conductivity below the energy gap (resulting in a pseudogap rather than a true energy gap) and a more gradual onset of conductivity above the energy gap. A temperature of 40K corresponds to a frequency of 58 cm^{-1} and so thermal effects can cause a significant smoothing of the onset of the conductivity for a rather large frequency range around the energy gap. This should greatly reduce the distortion of phonons near the energy gap in the computed spectrum.

In spite of the poor fit to the measured data at 40K, it is important to note that the phonon structure in the computed spectrum at 40K does not shift in frequency from the phonon structure in the spectrum at 2K even though the energy gap has shifted to a lower frequency. This is in agreement with experiment.

The polycrystalline nature of the pellet sample prevents a simple comparison of its FIR reflectance to transport measurements. However, the general results from the analysis of the data of the tape sample are in agreement with the data from the pellet sample. The reflectance of the pellet sample in unpolarized radiation at 2K is shown in Fig. 27. The reflectance approaches unity at low frequencies, but drops to ~50% at higher frequencies. The reflectance edge at 140 cm^{-1} is still present, although not nearly as sharp as in the spectrum of the tape sample. All of the strong phonon lines in the spectrum of the tape sample are also present in the spectrum of the pellet sample, but with reduced intensity and broadened linewidths. One additional absorption line is present in the pellet spectrum at

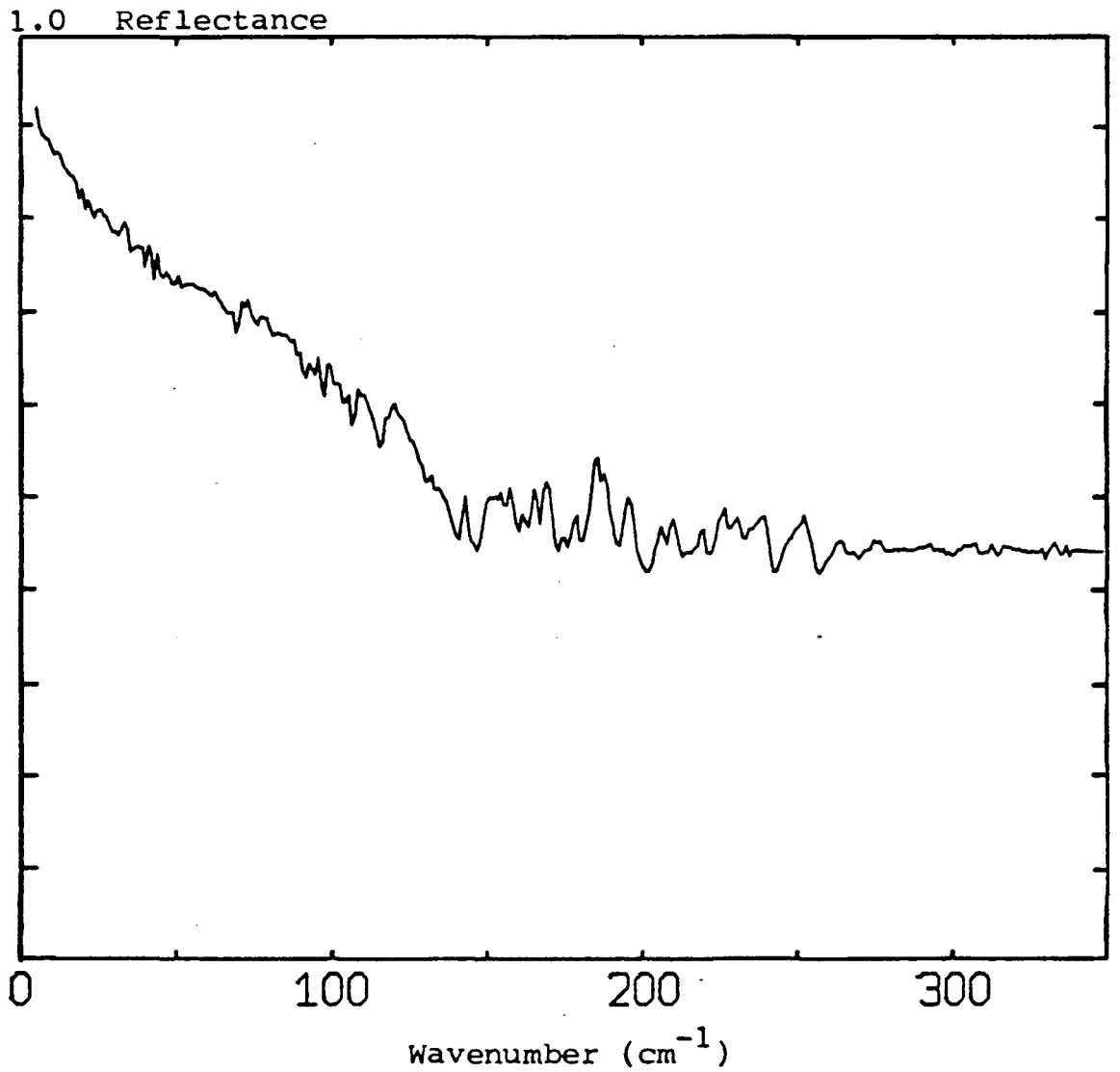

Fig. 27. Unpolarized reflectance of the pellet sample of $NbSe_3$ at 2K.

115 cm^{-1}. A Kramers-Kronig analysis of the reflectance gives values for $\sigma_1(\omega)$ and $\varepsilon_1(\omega)$ shown in Figs. 28 and 29, respectively. Because the high frequency extrapolation used in the Kramers-Kronig transform has a greater effect upon the calculation of the optical constants for the pellet sample, the results are shown for two choices of the adjustable parameter. In both cases it is clear that the conductivity increases at higher frequencies from a single-particle continuum, and that the high frequency phonons give rise to Fano interference effects in the conductivity. The oscillator strength in the low frequency mode (free carriers plus pinned mode) is very small, consistent with the results from the tape sample.

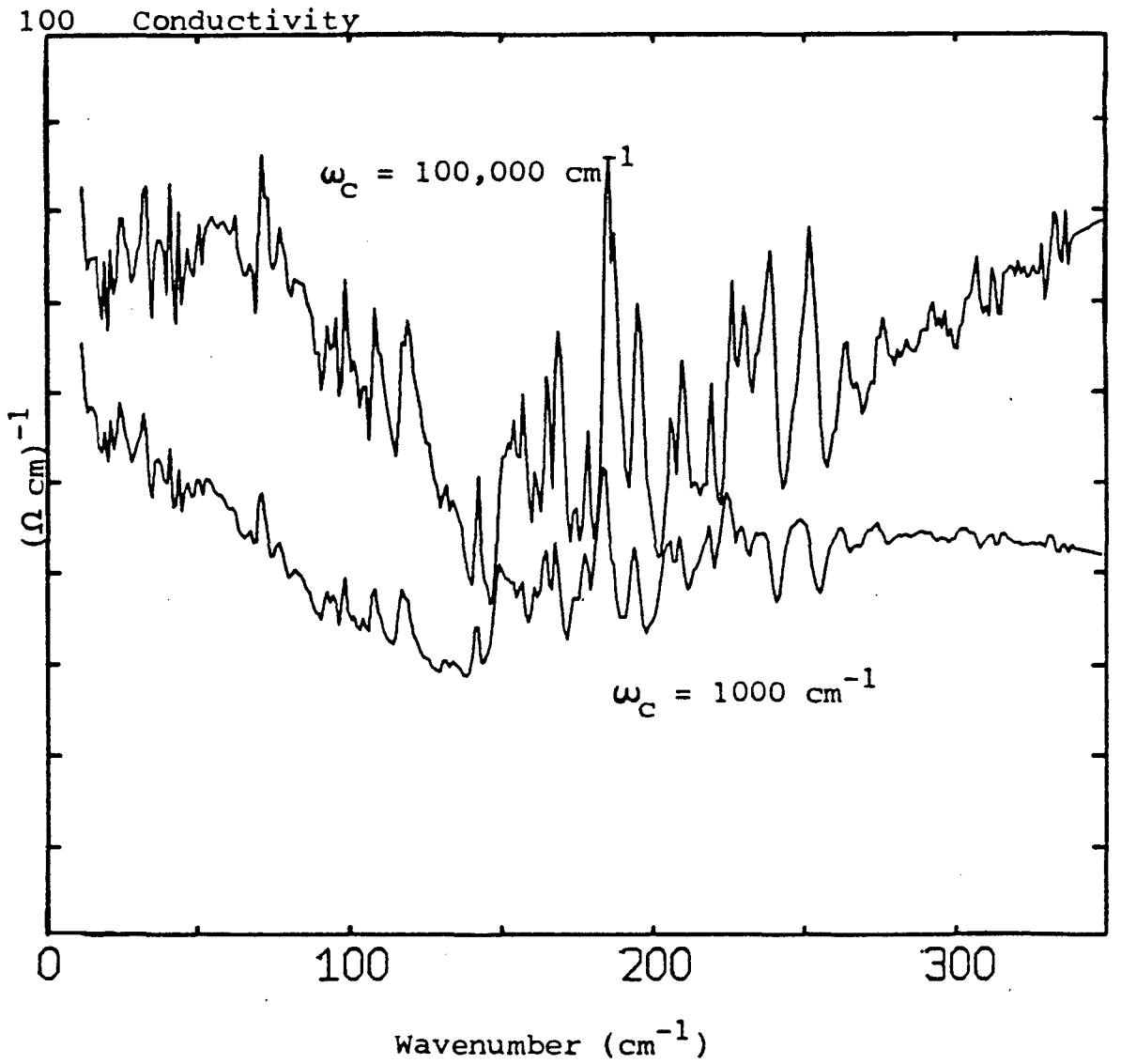

Fig. 28. $\sigma_1(\omega)$ from a Kramers-Kronig analysis of the reflectance of the pellet sample of $NbSe_3$ at 2K for two different values of the adjustable parameter.

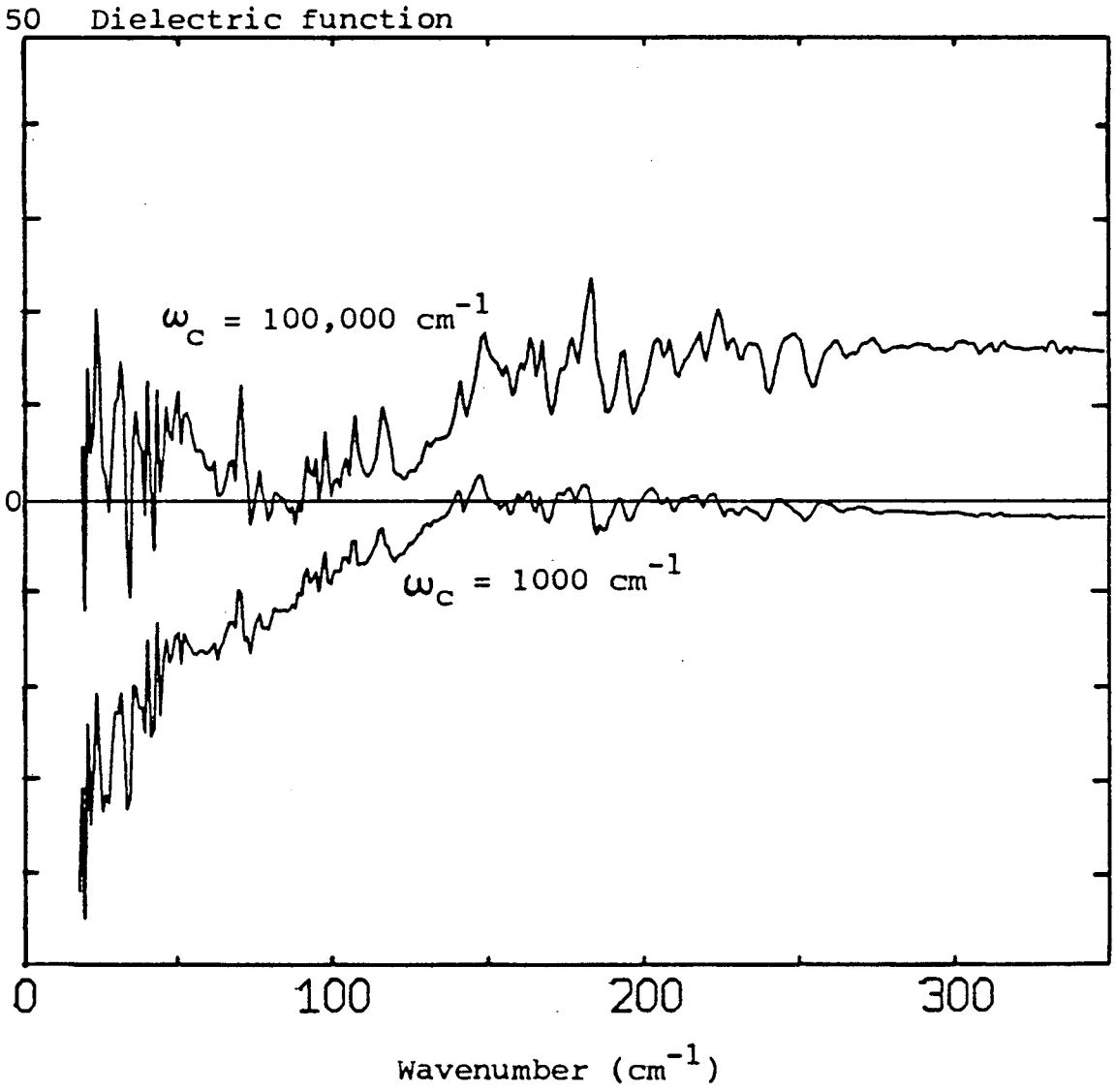

Fig. 29. $\epsilon_1(\omega)$ from a Kramers-Kronig analysis of the reflectance of the pellet sample of $NbSe_3$ at 2K for two different values of the adjustable parameter.

References

1. J. Bardeen, private communication.
2. P. A. Lee, T. M. Rice, P. W. Anderson, Sol. St. Comm. 14, 703 (1974).
3. M. J. Rice, Phys. Rev. Lett. 37 No. 1, 36 (1976).
4. P. A. Fedders, P. C. Martin, Phys. Rev. 143, 245 (1965).
5. N. P. Ong, Phys. Rev. B17 No. 8, 3243 (1978).
6. T. M. Rice, G. K. Scott, Phys. Rev. Lett. 35 No. 2, 120 (1975).
7. A. S. Barker, Jr., B. I. Halperin, T. M. Rice, Phys. Rev. Lett. 20 No. 8, 384 (1968).
8. J. B. Nielsen, K. Carneiro, Sol. St. Comm. 33, 1097 (1980).
9. J. Bardeen, Sol. St. Comm. 13, 357 (1973).
10. B. Horovitz, H. Gutfreund, M. Weger, Phys. Rev. B17 No. 6, 2796 (1978).
11. N. P. Ong, Phys. Rev. B18 No. 10, 5272 (1978).
12. J. Richard, P. Monceau, M. Renard, Phys. Rev. B25, 948 (1982).
13. G. Grüner, A. Zawadowski, P. M. Chaikin, Phys. Rev. Lett. 46 No. 7, 511 (1981).
14. N. P. Ong, C. M. Gould, Sol. St. Comm. 37, 25 (1980).
15. P. Bak, Phys. Rev. Lett. 48 No. 10, 692 (1982).
16. M. Weger, B. Horovitz, Sol. St. Comm. 43 No. 7, 583 (1982).
17. P. Monceau, M. Renard, J. Richard, M. C. Saint-Lager, H Salva, Z. Z. Wang, preprint.
18. G. Grüner, A. Zettl, W. G. Clark, J. Bardeen, Phys. Rev. B24, 7247 (1981).

VI. Fluctuational Superconductivity

When superconductivity was first discovered in quasi-one-dimensional organic compounds (the TMTSF salts), there was speculation that the low dimensionality of these materials would give rise to fluctuational superconducting effects at temperatures well above the three-dimensional superconducting transition temperature. It is the purpose of this section to briefly consider the model which has been proposed for quasi-one-dimensional fluctuational superconductivity in these materials.

A Ginzburg-Landau theory[1] has been proposed to model fluctuational superconductivity. In this theory, τ_N is the time constant for normal electrons to form virtually-bound Cooper pairs above the Fermi level, and τ_S is the time constant for these pairs to decay back into the normal state. The change in the density of states at the Fermi surface is determined by detailed balance to be $[N(\epsilon_F) - N_o]/N_o = \tau_S/\tau_N$. This gives rise to a pseudogap, or reduction in the electronic density of states at the Fermi surface. There is not a total elimination of states at the Fermi surface, however, as in a normal three-dimensional superconductor. A reduction in the electronic density of states at the Fermi surface from a superconducting pseudogap will cause a reduction in the conductivity at frequencies smaller than the pseudogap, and a gradual onset of the conductivity at frequencies larger than the pseudogap. FIR measurements can be used to determine the frequency dependence of the conductivity in this frequency range. Thus, FIR measurements can be

used to investigate the validity of applying the theory of fluctuational superconductivity to quasi-one-dimensional conductors.

In a material with superconducting fluctuations, the electrons are localized on individual chains. The material does not have zero resistance in this state, but its average dc resistnce is much smaller than it would be in the absence of the superconducting fluctuations. At lower temperatures the interchain tunneling of electrons can become coherent and establish three-dimensional transport. The material can then undergo a true superconducting transition.

Some of the TMTSF salts undergo SDW transitions, which are indicative of nested Fermi surfaces. In this sense, (see Chapter I), these materials are indeed quasi-one-dimensional. Estimates of the interchain transfer integral from band structure calculations, conductivity anisotropy measurements, optical anisotropy measurements, and other measurements indicate that transverse electrical transort in the TMTSF salts is coherent in two-dimensions below ~100K, and coherent in three-dimensions below ~10K.[2] Finally, estimates of the interchain coupling energy per unit length in the TMTSF salts lead to a coherence length at 1K (the superconducting transition temperature) for fluctuation effects of ~0.01 d, i.e. much smaller than a unit cell and therefore entirely negligible.[2] These results indicate that the quasi-one-dimensionality of the TMTSF salts is not sufficient to support fluctuational superconductivity at temperatures well above the three-dimensional superconducting transition temperature. In the next chapter we will consider in more detail the experimental evidence for and against this conclusion.

References

1. H. J. Shulz, D. Jerome, A. Mazaud, M. Ribault, K. Bechgaard, J. Phys. Lett. (Paris) 42 L313 (1981).

2. P. M. CHaikin, M.-Y. Choi, R. L. Greene, to be published in Les Editions de Physique (1983).

VII. Properties of $(TMTSF)_2X$ Compounds

The organic charge transfer salts based upon the TMTSF (tetramethyltetraselenafulvalene) molecule were first synthesized[1] in 1979. The salts crystallize according to the chemical formula $(TMTSF)_2X$ where X represents any one of a large number of inorganic anions, including PF_6, AsF_6, SbF_6, TaF_6, NO_3, BF_4, ReO_4, BrO_4, IO_4, FSO_3, and ClO_4. A typical procedure for synthesis of these salts[2] begins with a dilute (~0.01M) solution of TMTSF in CH_2Cl_2, containing 0.1M of the tetraalkylammonium or phosphonium salt of the appropriate anion as the electrolyte. The solution is oxidized onto a platinum electrode at a constant current of 5 to 10μA in an inert atmosphere. This current is sufficiently low to ensure that the crystallization rate is determined by diffusion rather than active transport. After a few weeks, the black crystals which form on the electrode may be collected and washed in CH_2Cl_2.

The crystal structure is shown in Fig. 30. It is triclinic with a $P\bar{1}$ (C_i^1) space group.[2] The anion positions are centers of inversion symmetry, but no other symmetry operations apply to the crystal lattice. There are two TMTSF molecules per unit cell, which are slightly dimerized at room temperature. In the PF_6 salt, the dimerization gives rise to interplanar distances of 3.63 Å and 3.66 Å. Each TMTSF molecule is nearly planar, with the two halves of the molecule enclosing an angle of 178.8°. The TMTSF molecules stack almost perpendicular to the fiber axis, deviating from perpendicularity

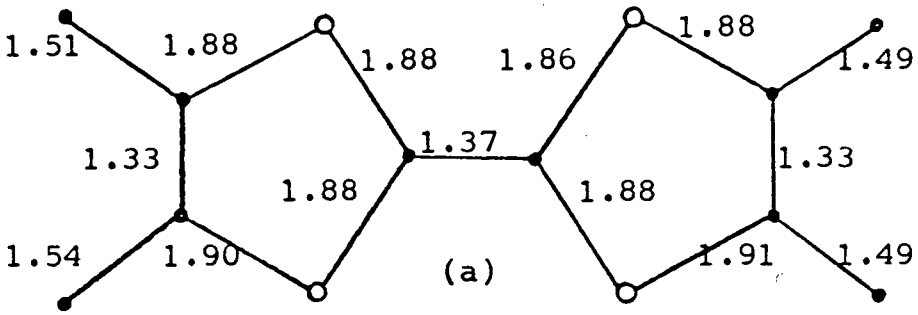

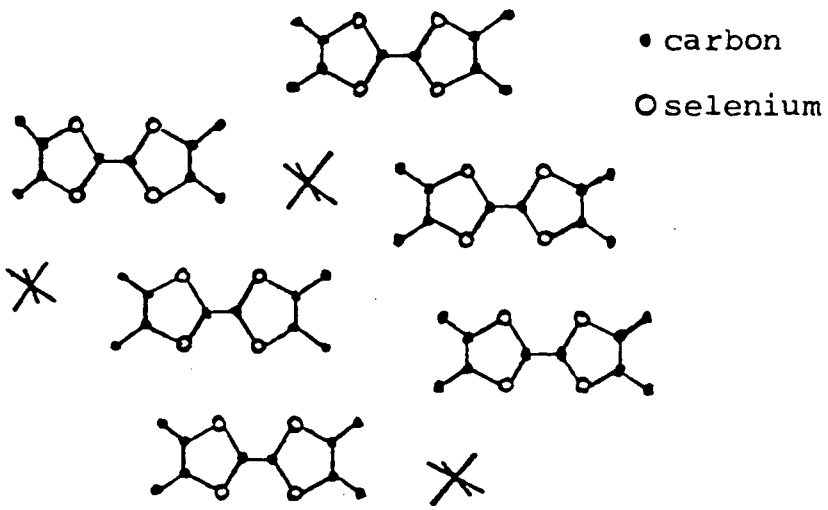

(b)

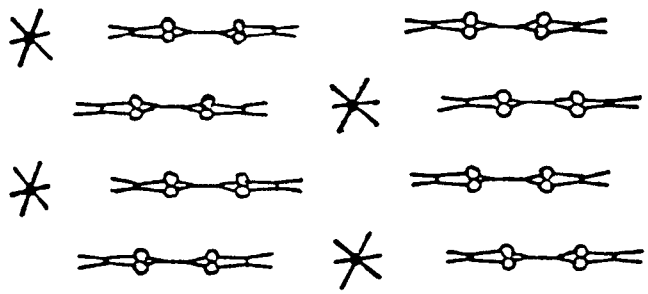

(c)

Fig. 30. (a) TMTSF molecule, (b) view along the fiber axis of the $(TMTSF)_2PF_6$ crystal, after ref. 2, (c) side view of the TMTSF stacks, after ref. 2.

by 1.1°. The stack units repeat by inversion with overlap displacements alternating along the fiber axis. The lattice parameters are a = 7.297(1) Å, b = 7.711(1) Å, c = 13.522(2) Å, and α = 83.39(1)°, β = 86.27(1)°, and γ = 71.01(1)°.

The anion accepts an electron from the TMTSF molecules, leaving half a hole on each TMTSF molecule, and a quarter-filled conduction band. The anion does not directly participate in the electrical conduction, although anion ordering transitions in some of these crystals can cause a semiconducting gap to open at the Fermi surface of the material. In general, the salts with centrosymmetric anions have properties which differ somewhat from salts with non-centrosymmetric anions.

a. Centrosymmetric anions

PF_6, AsF_6, SbF_6, TaF_6: The first organic material discovered to exhibit superconductivity was $(TMTSF)_2PF_6$. It becomes superconducting below ~1K, with the application of $\geq$6.5 kbars of pressure.[3] Both the PF_6 salt and the AsF_6 salt undergo metal-insulator (MI) transitions[6] at ambient pressure, however, at ~12K.[1] The absence of a $2k_F$ superlattice below the MI transition rules out a CDW origin for the formation of the energy gap at the Fermi surface.[4] The magnetic nature of the transition is indicated by the disappearance of the ESR signal,[5] the anisotropic lattice susceptibility below the transition,[6] and a spin-flop transition at ~4.5kG.[7] It is therefore concluded that the conduction electrons drive a SDW transition, making these materials itinerant antiferromagnets. The

anisotropy of the susceptibility indicates that the b-axis is the easy axis and the c-axis is the hard axis[6] (the a-axis is the fiber axis). In the SDW state the unit cell is doubled.[8] The resistance of the PF_6 salt does not show activated behavior characteristic of an energy gap in the SDW state,[9] but activation energies of 20 to 30K are measured in the resistivity,[10] and the susceptibility[8] of the AsF_6 salt.

The conductivity of the PF_6 salt in the SDW state increases at frequencies above ~1GHz.[11,12] This increase is interpretted as the response of the pinned SDW to the ac field, in much the same way as the CDW's in $NbSe_3$ lead to increased conductivity at the pinning frequency. However, no threshold depinning field is found in the dc conductivity, and the nonlinear IV characteristics which have been measured are probably due to hot electron effects,[13] rather than sliding SDW's, as initially proposed.[11] There is a very large magnetoresistance for magnetic fields parallel to the c*-axis at 4.2K.[9] In the regime of nonlinear conductivity, the magnetoresistance does not change.[14] This is evidence that the carriers responsible for the nonohmic conductivity are similar to the thermally excited carriers responsible for the ohmic conductivity, rather than carriers condensed in the SDW.

The centrosymmetric anion SbF_6 and the planar anion NO_3 also undergo MI transitions,[1] accompanied by vanishing ESR lines.[5] This implies that these materials also undergo SDW transitions.

The anisotropy in the conductivity of the PF_6 salt, which is fairly constant above 50K, decreases markedly below 50K.[15] Below 35K there is a large drop in the thermal conductivity, but this can be eliminated by applying a 50kG magnetic field.[16] At liquid helium temperatures, the mobility along the a-axis is very large, $\geq 10^4$ cm^2/Vs.[13,14]

Under pressure and for magnetic fields larger than 65kG at 1.1K, the PF_6 salt exhibits Schubnikov-de Haas oscillations which correspond to small, closed orbits in the ab plane with ~1 percent of the area of the cross section of the Brillouin zone.[17] The sudden onset of oscillations above this field implies that another phase transition occurs in high magnetic fields.

b. Noncentrosymmetric anions

ReO_4, BF_4, NO_3, ClO_4, FSO_3: The TMTSF salts with noncentrosymmetric anions in many cases also undergo MI transitions, but these are usually more abrupt and occur at higher temperatures than the SDW transitions previously considered. X-ray diffraction measurements[18] show that these MI transitions are driven by ordering of the anions. Because the anion position is an inversion center of the crystal, there will be at least two energetically degenerate orientations of the noncentrosymmetric anions. When the anions order with alternating orientations along the fiber axis, they create a periodic potential in the crystal which may have the correct periodicity to open a gap at the Fermi surface, in a manner analogous to a CDW transition discussed previously.

In the ReO_4 salt, the anions order with a modulation wavevector of (π/a, π/b, π/c) at 180K,[18] which gives rise to a large gap (~200K) at the Fermi surface. At 39K, the BF_4 salt also undergoes a MI transition, and because the ESR signal is present above and below the transition, it is believed that this is also an order-disorder (OD) transition.[5] An OD transition occurs in the NO_3 salt at 41K with a modulation wavevector of (π/a, 0, 0).[18] This is not an optimal wavevector for opening a gap at the Fermi surface, and so only a small anomaly is measured in the dc conductivity at this temperature.[1] The ClO_4 salt undergoes an OD transition at 24K if the crystals are cooled from 30K sufficiently slowly (0.1K/min.)[19-21] Rapid cooling, or quenching, at ~10K/min. is sufficient to freeze in the anion disorder and prevent the 24K OD transition. In this case, the ClO_4 salt undergoes a SDW transition at ~3.5K. The superconducting transition in slowly cooled samples of the ClO_4 salt occurs at 1.2K at ambient pressure. Quenched samples, on the other hand, have depressed superconducting transition temperatures, and for sufficiently fast quenching the superconducting transition can be entirely suppressed.[21] The FSO_3 salt undergoes a sharp MI transition at 87K, which is presumably an OD transition.[22]

Resistance and thermopower measurements of the ClO_4 salt as a function of temperature and magnetic field show that the transport mechanism changes below ~30K.[23] The ClO_4 salt also exhibits a sudden onset of Schubnikov-de Haas oscillations at magnetic fields above ~60kG at ambient pressure.[24]

The application of pressure decreases the transition temperatures of the OD[25] and SDW[3,10] transitions in the TMTSF salts. A pressure of ~10kbar is sufficient to suppress all of the MI transitions.

The transfer integrals and bandwidths are approximately the same for all of the TMTSF salts. They can be estimated from a variety of measurements, including the IR plasma frequencies, the conductivity anisotropy, the magnetoresistance anisotropy, and the superconducting critical field anisotropy. These measurements give consistent results for transfer integrals of magnitudes $t_a \cong 2000K$, $t_b \cong 150K$, and $t_c \cong 10K$. Bandstructure calculations[26] give an open Fermi surface in the TMTSF salts, and are in good agreement with these estimates of the transfer integrals.

Salts with both centrosymmetric and noncentrosymmetric anions become superconducting. The PF_6 salt was the first organic compound found to exhibit superconductivity.[3] Evidences for type II superconductivity in this material include a zero resistance state which could be suppressed by a transverse magnetic field of a few hundred gauss,[3] an anomaly in the specific heat of the correct magnitude for a 1K superconducting transition,[27] and a partial Meissner effect.[28,29] At 6.5 kbars of pressure, the PF_6 salt was found to undergo a SDW transition at ~6K, followed by a superconducting transition at ~1.1K.[30]

Under a pressure of 11kbars, superconductivity has also been observed in the AsF_6,[31] SbF_6,[32] TaF_6,[32] and ReO_4[25] salts.

The FSO_3 salt becomes superconducting with a transition temperature of >2K under pressures $\geq$5kbars.[22] The ClO_4 salt is unusual in that it becomes superconducting at ambient pressure (with a transition temperature of 1.2K).[33] The NO_3 salt, on the other hand, has not been observed to become superconducting under pressure down to 50mK.[34]

Small amounts of radiation-induced defects have a strong effect upon the phase transitions. A defect concentration of ~100 ppm is sufficient to suppress the superconducting transition to <20mK for the PF_6 salt,[35] and the ClO_4 salt.[36] A defect concentration of ~1000 ppm is sufficient to suppress the SDW transition in the PF_6 salt.[35]

Many sudden and unreproducible drops in the conductivity of TMTSF fibers usually occur when the fibers are cooled. These resistance jumps were at first attributed to microcracks in the crystals caused by stress.[14] However, when the fibers are warmed back to room temperature, their original resistance at room temperature is recovered. This suggests[37] that the resistance jumps are caused by mechanical deformation which releases strain from thermal contraction rather than from microcracks. As the number of resistance jumps increases (and the residual resistivity ratio decreases), the sharpness of the superconducting transition is reduced.

The superconducting critical fields are highly anisotropic.[36] For the ClO_4 salt, $H_{c2}^{a} \cong 11kG$, $H_{c2}^{b*} \cong 4kG$, and $H_{c2}^{c*} \cong 300G$. For the PF_6 salt, $H_{c2}^{a} \cong 5kG$, $H_{c2}^{b*} \cong 2kG$, and $H_{c2}^{c*} \cong 200G$. The

critical fields along the b* and c* axes for the AsF_6 salt are about an order of magnitude larger than for the PF_6 salt.[8]

The density of states at the Fermi surface in the PF_6 salt has been investigated by tunneling experiments.[27] A super Schottky tunnel junction was formed by evaporating n/GaSb onto a $(TMTSF)_2PF_6$ fiber. At a temperature of 50mK and a pressure of 11 kbars, an energy gap of 3.6 meV was measured from the dynamic resistance, dV/dI, of the junction. A similar measurement on the ClO_4 salt at ambient pressure gave an energy gap of 3 to 4 meV. The amplitude of the zero bias tunnel resistance (which is not directly related to the size of the energy gap) decreased with increasing temperature or with the application of a magnetic field. Tunneling characteristics in the dynamic resistance, however, persisted to temperatures as high as 15K. On one occasion the resistance of the tunnel junction went to zero at 12K.[38]

In addition to the infrared measurements we have made, other infrared measurements have been made on a number of the TMTSF salts. At temperatures below the OD transition in the ReO_4 salt, many new optical phonons appear in the IR spectrum through the Brillouin zone folding mechanism discussed in the chapter on CDW's.[39] The anion order induces the formation of a commensurate CDW in the crystal, which gives rise to coupled CDW-optical phonon modes with large oscillator strengths. However, no additional optical phonons appeared in the IR spectrum of the PF_6 salt below the 12K SDW transition. This is evidence that the SDW transition in the PF_6 salt is not accompanied by the formation of a CDW as well.

The polarized reflectance spectrum of the PF_6 salt has been extensively studied.[40,41] A reflectance edge is seen in the infrared for radiation polarized both parallel and perpendicular to the fibers. It is highly unusual for a quasi-one-dimensional organic conductor to exhibit a transverse reflectance edge, and this is another indication of the higher effective dimensionality in this material at low temperatures. At 25K for radiation polarized parallel to the fibers, there is a reflectance edge at ~7000 cm^{-1}. For light polarized perpendicular to the fibers, along the b*-axis, the reflectance edge occurs at ~1000 cm^{-1}. A careful analysis[42] of this data estimates the bandwidth anisotropy to be ~10. There is an extremely large bandwidth of ~1.2eV along the a-axis,[40] while the bandwidth along the b*-axis is estimated to be only ~0.14 eV.[42]

A Kramers-Kronig analysis of the reflectance of the PF_6 salt was performed to obtain the optical constants.[41] There is no evidence in the conductivity at frequencies as low as 10 cm^{-1} for the large dc conductivity of this material. This suggests that the optical relaxation frequency is much smaller than the relaxation frequency appropriate for the dc transport properties. There is a large peak in the conductivity between 200 and 500 cm^{-1}, which has not been satisfactorily explained.

The IR reflectance of the AsF_6 and ReO_4 salts have also been measured.[41] The AsF_6 salt has a reflectance edge similar to that of the PF_6 salt for radiation polarized parallel to the b*-axis. Because of the larger size of the crystals, it was also possible to

measure the IR reflectance for radiation polarized parallel to the c-axis, but there is no reflectance edge in this direction. A Kramers-Kronig analysis of the reflectance of the ReO_4 salt reveals the existence of a semiconducting energy gap in the conductivity below the OD transition. Above the transition, the energy gap is partially filled, leaving a pseudogap in the conductivity at room temperature.

Infrared reflectance measurements have also been made on the ClO_4 salt. For radiation polarized parallel to the fiber axis, there is a reflectance edge at ~7000 cm^{-1}.[43] For radiation polarized parallel to the b*-axis, there is a reflectance edge at ~1000 cm^{-1}, with the reflectance rising to 55 percent at 500 cm^{-1}.[41] A Drude model gives a good fit to the reflectance for radiation polarized parallel to the fibers at frequencies between 5000 and 10,000 cm^{-1}.[43] Typical parameters obtained from the Drude fit to the infrared reflectance at 30K are $\varepsilon = 2.46$, $\omega_p = 1.26$eV, $\tau = 7.83 \times 10^{-15}$s, $\sigma_{opt}(0) = 2540\ (\Omega cm)^{-1}$, $m^* = 1.25\ m_o$, and $4t = 1.03$ eV. $\sigma_{opt}(0)$ is the dc conductivity extrapolated from the Drude fit, and is much smaller than the actual dc conductivity, which again suggests that the optical relaxation frequency is much shorter than the dc relaxation frequency. 4t is the calculated value for the bandwidth. A summary of some of the properties of the TMTSF salts is given in Table 4.

Two widely different models have been proposed to explain the transport properties of the TMTSF salts below ~40K. As discussed previously, one model attempts to interpret the experimental data in terms of fluctuational superconductivity at high temperatures.[8] In

Table 4. Properties of TMTSF salts[8,22,52]

Anion	T_o(K)	Transition	Anion symmetry	P_c(kbar)
PF_6	12	SDW	Octahedral	8
AsF_6	12	SDW	Octahedral	9.5
SbF_6	17	SDW	Octahedral	11
TaF_6	---	---	Octahedral	10
ClO_4	24 3.5	OD SDW	Tetrahedral	.001
ReO_4	180	OD	Tetrahedral	9.5
BF_4	39	OD(?)	Tetrahedral	---
BrO_4	220	OD(?)	Tetrahedral	---
IO_4	semiconductor	---	Tetrahedral	---
NO_3	12	SDW	Planar	No sc
FSO_3	87	OD	Asymmetric	5

T_o: Temperature of the SDW or OD transition.

P_c: Pressure under which the salt will become superconducting at a sufficiently low temperature (which is ~1K for all of the salts in this table except FSO_3, which has a superconducting transition at >2K).

this model, superconducting fluctuation effects are supposed to exist at temperatures as high as 40K. They suppress the three-dimensional mean field transition temperature for superconductivity from ~10K to ~1K.

An alternate, and more conventional model interprets the experimental data in terms of single-particle transport processes of highly mobile carriers.[36] All fluctuation effects found in this model are assumed to be negligible. We now present the arguments found in the literature for these models, some of which we do not find justified.

c. Arguments in favor of fluctuational superconductivity

The conductivity of the TMTSF salts at liquid helium temperatures can be an order of magnitude larger than the conductivity of any other organic material. This is considered to be evidence for a new form of electrical transport, i.e., fluctuational superconductivity, in the TMTSF salts. In addition, the conductivity does not saturate to a fairly constant value at liquid helium temperatures, as it does in most other metals as a result of impurities when a single-particle transport mechanism is important.[8,34,44]

The extremely large magnetoresistance in the TMTSF salts finds a natural explanation in terms of destruction of fluctuating Cooper pairs. The extreme sensitivity of the conductivity to radiation-induced defects is difficult to explain in a single-particle picture of electrical transport but if the defects are magnetic then they can act as orbital pair-breakers of fluctuating Cooper pairs.[8,34,44]

The large drop in the thermal conductivity at temperatures below 50K can be restored by a magnetic field applied parallel to the fiber axis. Carriers involved in superconducting fluctuations do not contribute to the thermal conductivity, but if they are destroyed by a magnetic field then the thermal conductivity will be restored, in agreement with experiment.[8,16,34]

To explain the carrier concentration and measured conductivity at liquid helium temperatures in a single-particle model, mean free paths of ~700 intermolecular spacings are required, and mobilities in excess of 10^3 cm^2/Vs are necessary. Such large mobilities and long mean free paths require a degree of purity and perfection which are unlikely in organic conductors.[44]

The infrared data for the PF_6 salt exhibit a pseudogap in the conductivity below ~50 cm^{-1} (6.3 meV),[6] in agreement with the tunneling data. This gap is much too large to be associated with the 1K superconducting energy gap, and in addition, the gap is measured at temperatures well above 1K. It cannot be associated with a SDW, because a magnetic field tends to destroy the measured gap in the tunneling experiment rather than stabilize it. Also, if a SDW pseudogap exists at temperatures of ~30K, the resistivity should begin to increase with decreasing temperature as the SDW state becomes more stable, in contrast to the measurements. The zero tunnel junction resistance measured in one sample at 12K can be explained by a theory of fluctuational superconductivity.[8,34,45-47]

d. Arguments in favor of single-particle transport

On the other hand, the measured anisotropy of the superconducting critical field in the ClO_4 salt is 28:15:1 for $H_{c2}^{a}:H_{c2}^{b*}:H_{c2}^{c*}$. From the calculated values of the transfer integrals, the anisotropy is expected to be approximately 200:20:1 if the same mechanism is involved in limiting the critical field for all three directions. The critical field along the a-axis is much smaller than is expected, and therefore it must be limited by something other than orbital pair-breaking. The obvious alternative is a Pauli limiting effect due to spin pair-breaking. The Pauli critical field is directly related to the superconducting transition temperature and the size of the superconducting energy gap. The measured critical field is in good agreement with the 1K transition temperature. The large gap measured in the tunneling experiment, however, implies a Pauli limit which is twenty times larger than the measured critical field and therefore the tunneling gap must not be related to superconductivity.[36,48,49]

An electron-phonon coupling term quadratic in the phonon operators can account well for the temperature and pressure dependence of the resistivity to below 20K.[49,50] A phonon-drag theory in a model of single-particle transport may successfully account for the small optical relaxation frequency obtained from the IR measurement.[49,51]

If superconducting fluctuations are significant, then the conductivity measured as a function of current or electric field should show increasing resistivity at higher currents and fields as a result of momentum depairing. This is not found experimentally.[48]

Superconducting fluctuations should not cause a decrease in the thermal conductivity, but rather an increase, because the quasi-particles have reduced scattering rates as the temperature decreases. This has been found to be true in filaments of lead. Therefore, the measured decrease in the thermal conductivity with decreasing temperature in the TMTSF salts provides evidence against the model of fluctuational superconductivity.[48]

The thermopower drops toward zero with decreasing temperature, but then becomes negative below 7.5K. The change in sign of the thermopower cannot be explained by superconducting fluctuations, and demonstrates that a different transport mechanism is giving rise to the temperature dependence of the thermopower.[23]

If the scattering rate at the Fermi surface is anisotropic, then the large magnetoresistance can be explained by the single-particle transport model. The dc conductivity is dominated by carriers in regions of the Fermi surface with long lifetimes, but in a magnetic field these carriers are swept into other regions with a high scattering rate and the conductivity is thereby reduced.[48] An increased scattering rate caused by radiation-induced defects is also sufficient to explain the change in conductivity by a single-particle transport mechanism.[35]

The pseudogap measured in the infrared data[41] for the PF_6 salt is actually ~200 cm^{-1} (25 meV), not ~50 cm^{-1}, and therefore is much too large to be associated with the gap measured in the tunneling

experiment (3-4 meV). In addition, the pseudogap in the IR data exists up to 300K, which is well above the temperatures at which superconducting fluctuations are hypothesized to be important.

The energy gap measured by the tunneling experiment could arise naturally from the band structure or a SDW state, or could result from superconducting amorphous gallium or antimony at the interface of the junction. Although large changes are measured in the resistivity and thermal conductivity for magnetic fields at 2kG, no change was observed in the tunneling gap size in fields of up to 25kG,[36,48] even though the zero bias tunneling resistance decreased in a magnetic field.

References

1. K. Bechgaard, C. S. Jacobsen, K. Mortensen, H. J. Pedersen, N. Thorup, Sol. St. Comm. 33, 1119 (1980).
2. N. Thorup, G. Rindorf, H. Soling, K. Bechgaard, Acta Cryst. B37, 1236 (1981).
3. D. Jérome, A. Mazaud, M. Ribault, K. Bechgaard, J. Phys. Lett. (Paris) 41, L95 (1980).
4. J. P. Pouget, Chemica Scripta 17, 85 (1981).
5. J. C. Scott, H. J. Pedersen, K. Bechgaard, Phys. Rev. B24, 475 (1981).
6. K. Mortensen, Y. Tomkiewicz, K. Bechgaard, Phys. Rev. B25, 3319 (1982).
7. K. Mortensen, Y. Tomkiewicz, T. D. Shultz, E. M. Engler, Phys. Rev. Lett. 46, 1234 (1981).
8. D. Jérome, H. J. Schulz, Adv. In Phys. 43, 443 (1982).
9. C. S. Jacobsen, K. Mortensen, M. Weger, K. Bechgaard, Sol. St. Comm. 38, 423 (1981).
10. R. Brusetti, M. Ribault, D. Jérome, K. Bechgaard, J. Phys. (Paris) 43, 801 (1982).
11. W. M. Walsh, Jr., F. Wudl, G. A. Thomas, D. Nalewajek, J. J Hauser, P. A. Lee, T. Poehler, Phys. Rev. Lett. 45 No. 10, 829 (1980).
12. A. Zettl, G. Grüner, E. M. Engler, preprint.
13. P. M. Chaikin, G. Grüner, E. M. Engler, R. L. Greene, Phys. Rev. Lett. 45, 1874 (1980).

14. P. M. Chaikin, P. Haen, E. M. Engler, R. L. Greene, Phys. Rev. B24 No. 12, 7155 (1981).

15. H. J. Schulz, D. Jérome, A. Mazaud, M. Ribault, K. Bechgaard, J. Phys. (Paris) 42, 991 (1981).

16. D. Djurek, M. Prester, D. Jérome, K. Bechgaard, J. Phys. C15, L669 (1982).

17. J. F. Kwak, J. E. Schirber, R. L. Greene, E M. Engler, Phys. Rev. Lett. 46, 1296 (1981).

18. J. P. Pouget, R. Moret, R. Comès, K. Bechgaard, J. M. Fabre, L. Giral, Mol. Crys. Liq. Crys. 79, 129 (1982).

19. P. Garoche, R. Brusetti, K. Bechgaard, Phys. Rev. Lett. 49 No. 18, 1346 (1982).

20. T. Takahashi, D. Jérome, K. Bechgaard, J. Phys. Lett. (Paris) 43, L565 (1982).

21. H. Schwenk, K. Andres, F. Wudl, Phys. Rev. B27 No. 9, 5846 (1983).

22. R. C. Lacoe, S. A. Wolf, P. M. Chaikin, F. Wudl, E. Aharon-Shalom, Phys. Rev. B27 No. 3, 1947 (1983).

23. M.-Y. Choi, P. M. Chaikin, R. L. Greene, to be published in Les Editions de Physique (1983).

24. J. F. Kwak, J. E. Schirber, R. L. Greene, E M. Engler, Mol. Crys. Liq. Crys. 79, 111 (1982).

25. S. S. P. Parkin, D. Jérome, K. Bechgaard, Mol. Crys. Liq. Crys. 79, 213 (1982).

26. P. M. Grant, to be published in Les Editions de Physique (1983).

27. P. Garoche, R. Brusetti, D. Jérome, K. Bechgaard, J. Phys. Lett. (Paris) 43, L147 (1982).

28. M. Ribault, G. Benedek, D. Jérome, K. Bechgaard, J. Phys. Lett. (Paris) 41, L397 (1980).

29. K. Andres, F. Wudl, D. B. McWhan, G. A. Thomas, D. Nalewajek, A. L. Stevens, Phys. Rev. Lett. 45, 1449 (1980).

30. R. L. Greene, E. M. Engler, Phys. Rev. Lett. 45 No. 19, 1587 (1980).

31. M. Ribault, J. P. Pouget, D. Jérome, K. Bechgaard, J. Phys. Lett. (Paris) 41, L607 (1980).

32. S. S. P. Parkin, M. Ribault, D. Jérome, K. Bechgaard, J. Phys. C14, L445 (1981).

33. K. Bechgaard, K. Carneiro, M. Olsen, F. B. Rasmussen, Phys. Rev. Lett. 46, 852 (1981).

34. D. Jérome, Mol. Crys. Liq. Crys. 79, 155 (1982).

35. M.-Y. Choi, P. M. Chaikin, S. Z. Huang, P. Haen, E. M. Engler, R. L. Greene, Phys. Rev. B25 No. 10, 6208 (1982).

36. R. L. Greene, P. Haen, S. Z. Huang, E. M. Engler, M.-Y. Choi, P. M. Chaikin, Mol. Crys. Liq. Crys. 79, 183 (1982).

37. T. Ishiguro, K. Murata, K. Kajimura, N. Kinoshita, H. Tokumoto, M. Tokumoto, T. Ukachi, H. Anzai, G. Saito, preprint.

38. A. Fournel, C. More, G. Roger, J. P. Sorbier, J. M. Delrieu, D. Jérome, M. Ribault, K. Bechgaard, J. Phys. Lett. (Paris) 42, L445 (1981).

39. R. Bozio, C. Pecile, K. Bechgaard, F. Wudl, D. Nalewajek, Sol. St. Comm. 41 No. 12, 905 (1982).

40. C. S. Jacobsen, D. B. Tanner, K. Bechgaard, Phys. Rev. Lett. 46 No. 17, 1142 (1981).

41. C. S. Jacobsen, D. B. Tanner, K. Bechgaard, Mol. Crys. Liq. Crys. 79, 25 (1982).

42. J. F. Kwak, Phys. Rev. B26 No. 8, 4789 (1982).

43. K. Kikuchi, I. Ikemoto, K. Yakushi, H. Kuroda, K. Kobayashi, Sol. St. Comm. 42 No. 6, 433 (1982).

44. H. J. Schulz, D. Jérome, A. Mazaud, M. Ribault, K. Bechgaard, J. Phys. (Paris) 42, 991 (1981).

45. C. More, G. Roger, J. P. Sorbier, D. Jerome, M. Ribault, K. Bechgaard, J. Phys. Lett. (Paris) 42, L313 (1981).

46. A. Fournel, C. More, G. Roger, J. P. Sorbier, J. M. Delrieu, D. Jérome, M. Ribault, K. Bechgaard, J. M. Fabre, L. Giral, Mol. Crys. Liq. Crys. 79, 261 (1982).

47. H. J. Schulz, Mol. Crys. Liq. Crys. 79, 199 (1982).

48. P. M. Chaikin, M.-Y. Choi, R. L. Greene, to be published in Les Editions de Phys. (1983).

49. R. L. Greene, H. Gutfreund, M. Weger, preprint.

50. H. Gutfreund, M. Weger, Phys. Rev. B16, 1753 (1977).

51. S. Marianer, M. Kaveh, M. Weger, Phys. Rev. B25, 5197 (1982).

52. S. S. P. Parkin, M. Ribault, D. Jérome, K. Bechgaard, J. Phys. C14, 5305 (1981).

VIII. Measurements and analysis of infrared properties of $(TMTSF)_2ClO_4$

Our FIR measurements on $(TMTSF)_2ClO_4$ have been made with crystals supplied by R. L. Greene of IBM Research, San Jose. Typical dimensions of the crystal fibers were 0.1 mm x 1 mm x 10 mm. The samples used for reflectance measurements were composed of 10 to 30 parallel fibers with a total surface area of 0.5 to 1 cm^2. The fibers were attached to a sheet of black epoxy for heat sinking. The sample temperature could be regulated from 1.5K to ~100K. The apparatus shown in Fig. 3 was used for reflectance measurements. Absolute normalizations of the reflectance spectra were obtained by measuring the reflectance of the sample after it was covered with evaporated gold.

Polarized reflectance measurements from 5 to 340 cm^{-1} at 2K and 60K are shown in Figs. 31 and 32, respectively. The measurements for radiation polarized parallel to the fibers were made on the third thermal cycle (between room temperature and liquid helium temperature) of the sample. The measurements for radiation polarized perpendicular to the fibers were made on the sixth thermal cycle of the sample.

The reflectance at 2K for radiation polarized parallel to the fibers has a broad minimum between 10 and 150 cm^{-1}, with a peak in the reflectance occurring between 25 and 30 cm^{-1}. At frequencies above 150 cm^{-1} the reflectance is $\geq$95 percent to the limit of our measurements at 340 cm^{-1}. Because the reflectance at the higher frequencies is so large, we are confident that the normalization of

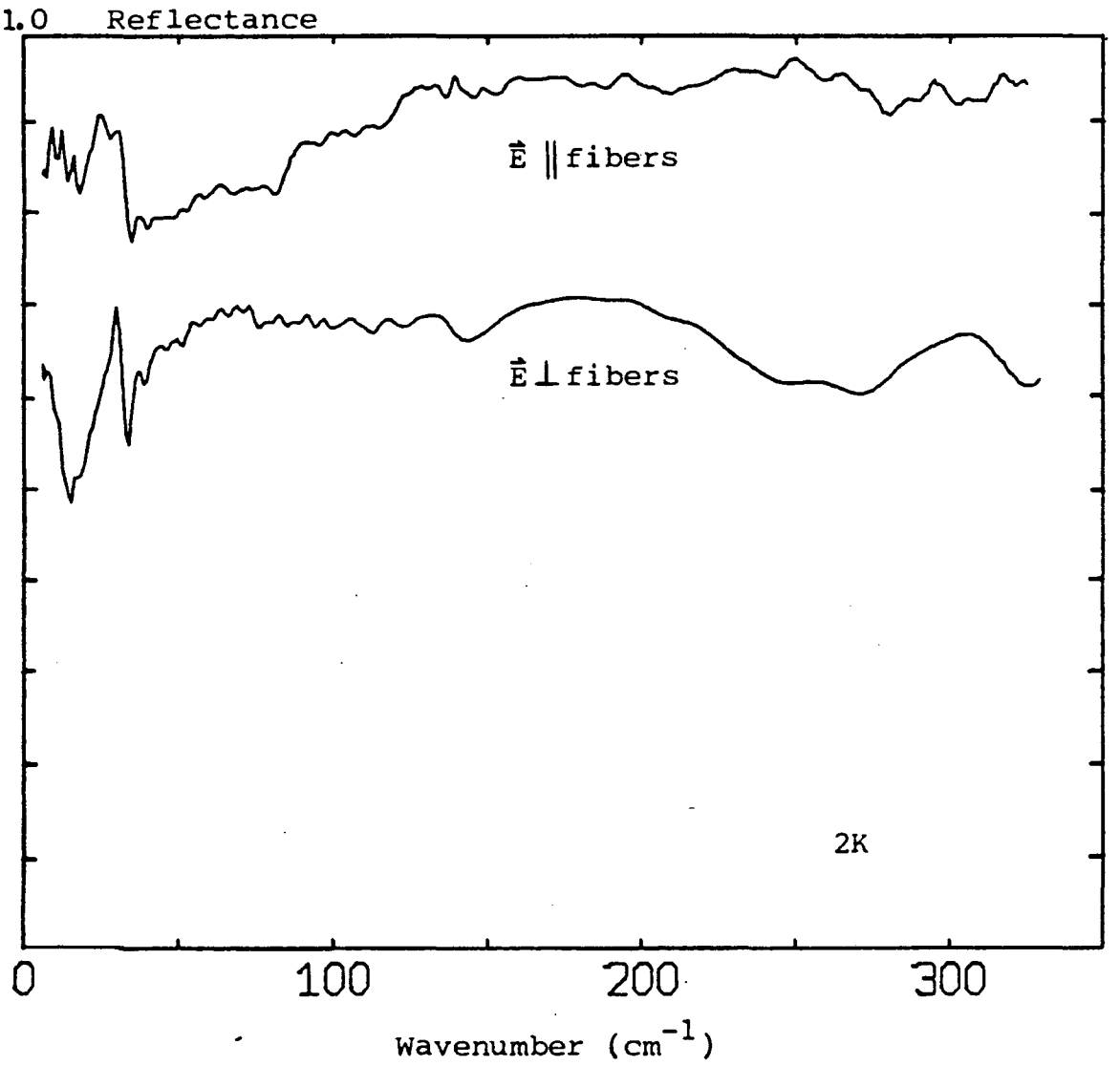

Fig. 31. Normalized reflectance of $(TMTSF)_2ClO_4$ at 2K.

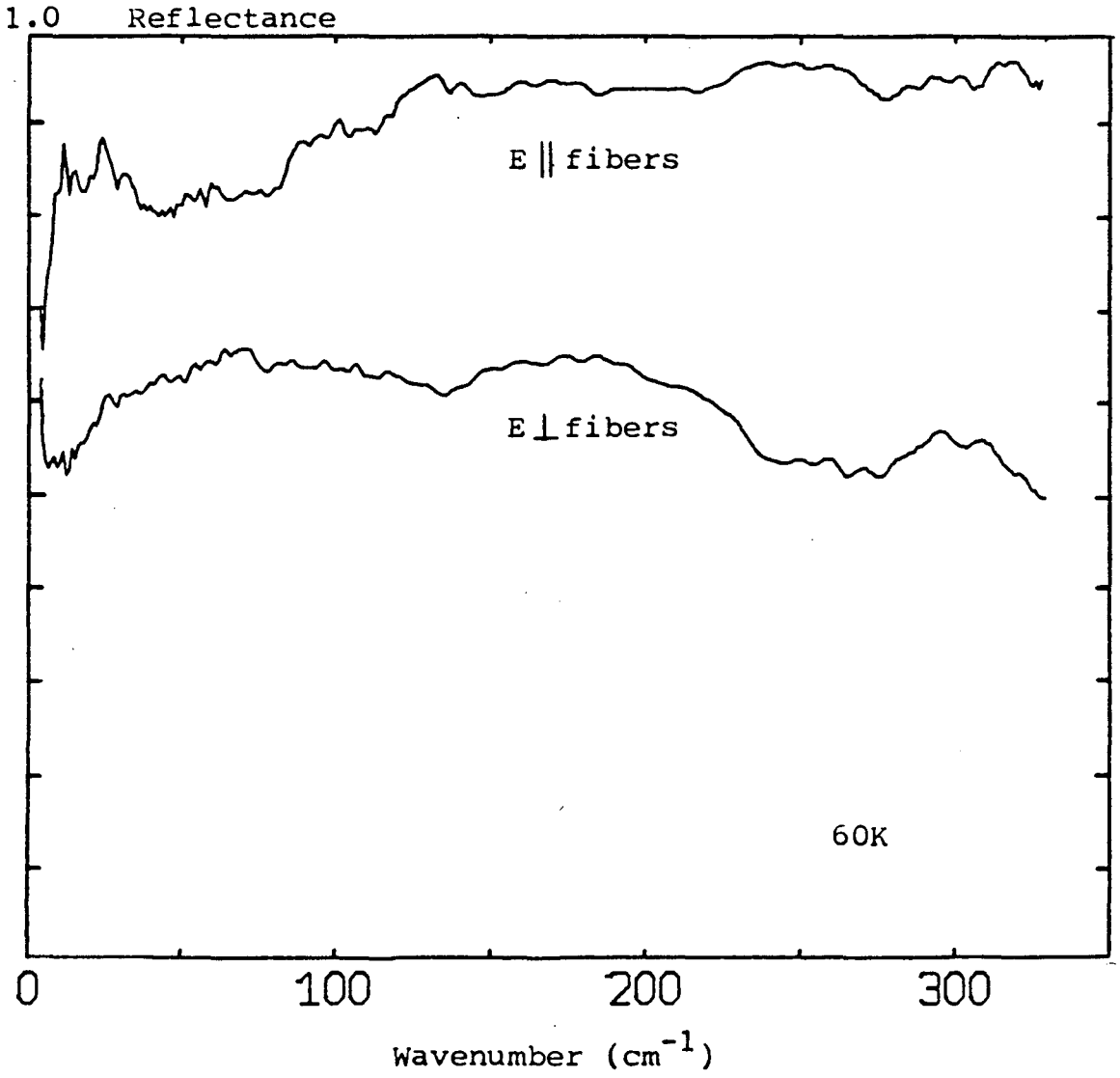

Fig. 32. Normalized reflectance of $(TMTSF)_2ClO_4$ at 60K.

the data by the reflectance of the gold-coated sample has corrected for diffuse scattering from the sample surface which tends to reduce the measured reflectance. However, the measured reflectance at the lower frequencies is generally smaller than is expected for a highly conducting material like $(TMTSF)_2ClO_4$. This may be a result of thermal cycling (which will be discussed later) or it may indicate another type of normalization error in the data. Because the sample of $(TMTSF)_2ClO_4$ fibers was not large enough to fill the entire light pipe of the reflectance apparatus, we reduced the diameter of the light pipe opening at the sample by a factor of three. It is possible that the long wavelength radiation was sufficiently diffracted by the opening of the light pipe, that a small fraction of the radiation was incident on and absorbed by the black epoxy substrate around the edges of the fibers, rather than on the fibers themselves. This hypothesis could account for the small reflectance of the sample of $(TMTSF)_2ClO_4$ fibers on the epxoy substrate at the lower frequencies.

The reflectance at 60K for radiation polarized parallel to the fibers is very similar to the reflectance at 2K. There is still a broad minimum in the reflectance between 10 and 150 cm^{-1}. The peak in the reflectance between 25 and 30 cm^{-1}, however, has largely disappeared. The sharp drop in the reflectance below 10 cm^{-1} may also be an indication of a normalization error at low frequencies.

Further information can be obtained from the reflectance data by means of a Kramers-Kronig analysis. Figures 33 and 34 show $\sigma_1(\omega)$ at

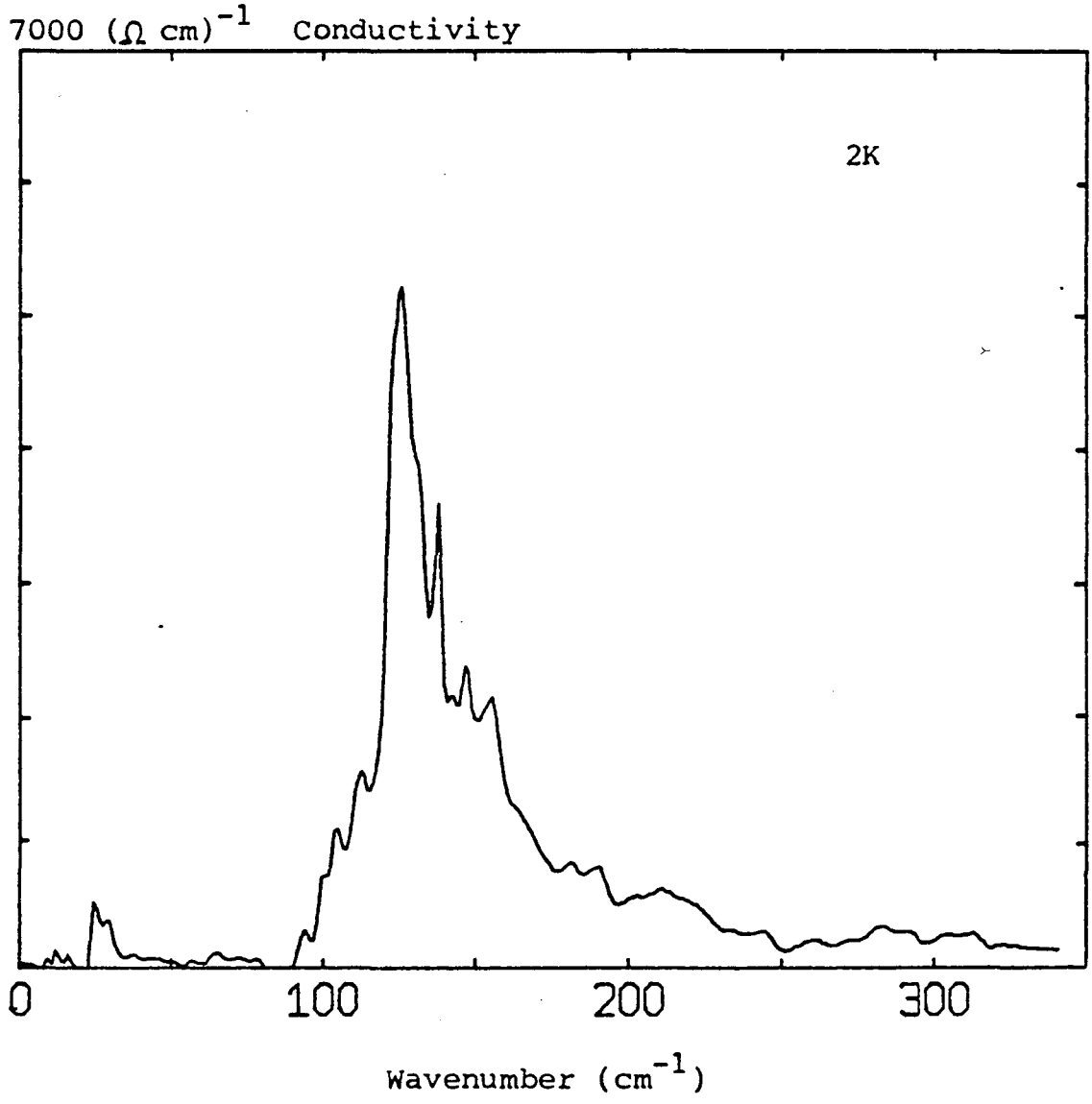

Fig. 33. $\sigma_1(\omega)$ computed from a Kramers-Kronig analysis of the reflectance of $(TMTSF)_2ClO_4$ at 2K with the adjustable parameter equal to 2000 cm^{-1}.

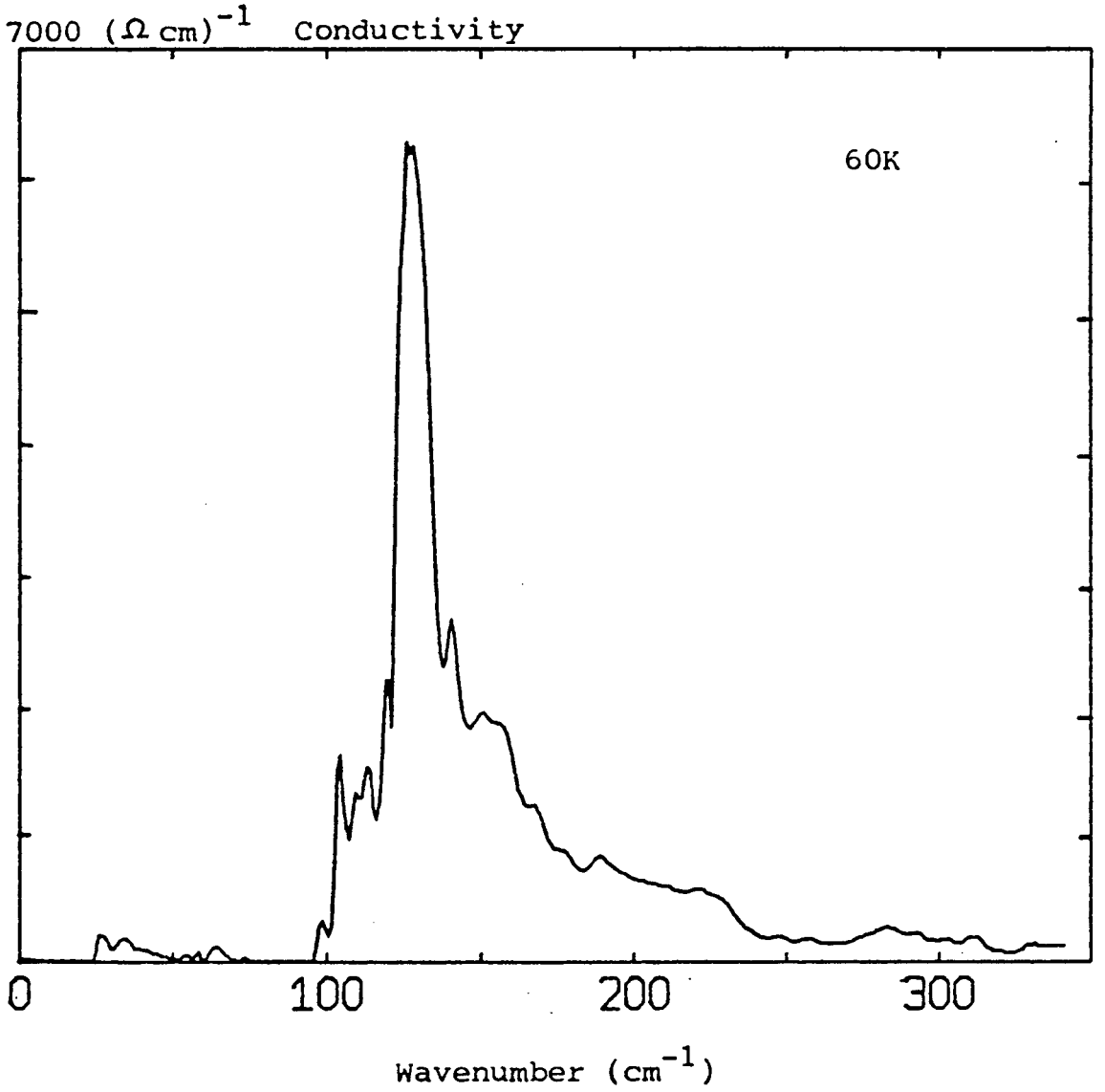

Fig. 34. $\sigma_1(\omega)$ computed from a Kramers-Kronig analysis of the reflectance of $(TMTSF)_2ClO_4$ at 60K with the adjustable parameter equal to 2000 cm^{-1}.

2K and 60K calculated using a cutoff frequency for the adjustable parameter of 2000 cm^{-1}. Figures 35 and 36 show $\sigma_1(\omega)$ for a cutoff frequency of 1000 cm^{-1}. In all cases in this chapter, the high frequency extrapolation of the reflectance used in the Kramers-Kronig analysis is of the ω^{-s}, ω^{-4} type described in Appendix A. Unfortunately, the adjustable parameter has a sizable effect in the computation of the optical constants at low frequencies. Accurate reflectance measurements to near IR frequencies will be required to obtain more accurate estimates of the optical constants at frequencies <100 cm^{-1}. However, there is a large peak in the conductivity at ~100 to 150 cm^{-1}, independent of the various extrapolations we have tried in the Kramers-Kronig transform. The peak in the reflectance between 25 and 30 cm^{-1} results from a peak in the conductivity at 25 cm^{-1}. The maximum conductivity and the total oscillator strength of this peak is much smaller than of the peak in the conductivity above 100 cm^{-1}. The extrapolation with the 2000 cm^{-1} cutoff indicates a pseudogap in the conductivity below 100 cm^{-1} (12 meV). The extrapolation with the 1000 cm^{-1} cutoff exhibits a similar pseudogap. In this case, however, the conductivity begins to increase at frequencies above ~30 cm^{-1} (3.7 meV).

The extrapolation with a 2000 cm^{-1} cutoff frequency is probably more reasonable than the extrapolation with the 1000 cm^{-1} cutoff frequency. First of all, the integrated oscillator strength is much larger for the 2000 cm^{-1} cutoff, which is more consistent with the large carrier concentration. Secondly, the conductivity at the higher

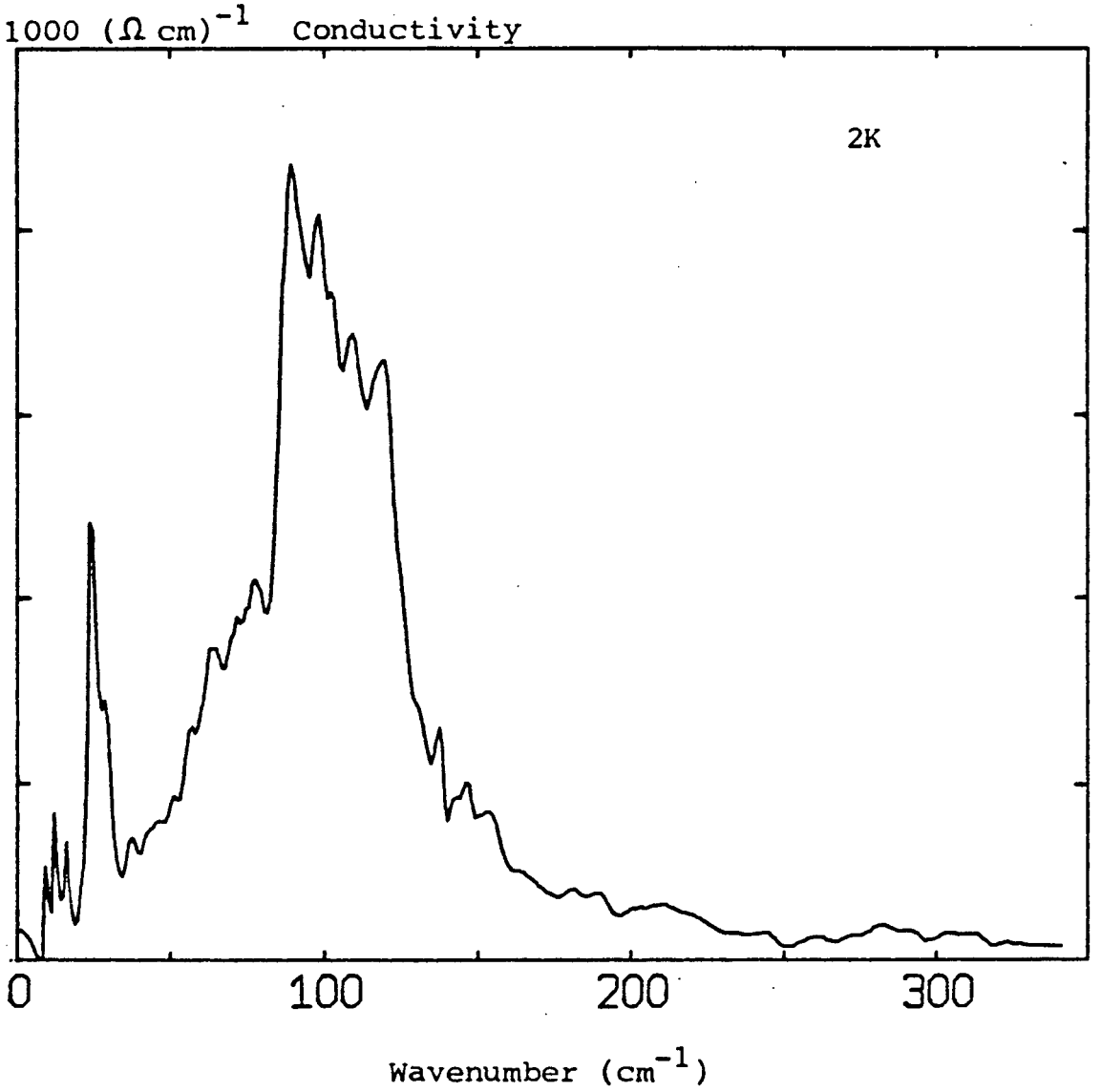

Fig. 35. $\sigma_1(\omega)$ computed from a Kramers-Kronig analysis of the reflectance of $(TMTSF)_2ClO_4$ at 2K for radiation polarized parallel to the fiber axis, with the adjustable parameter equal to 1000 cm^{-1}.

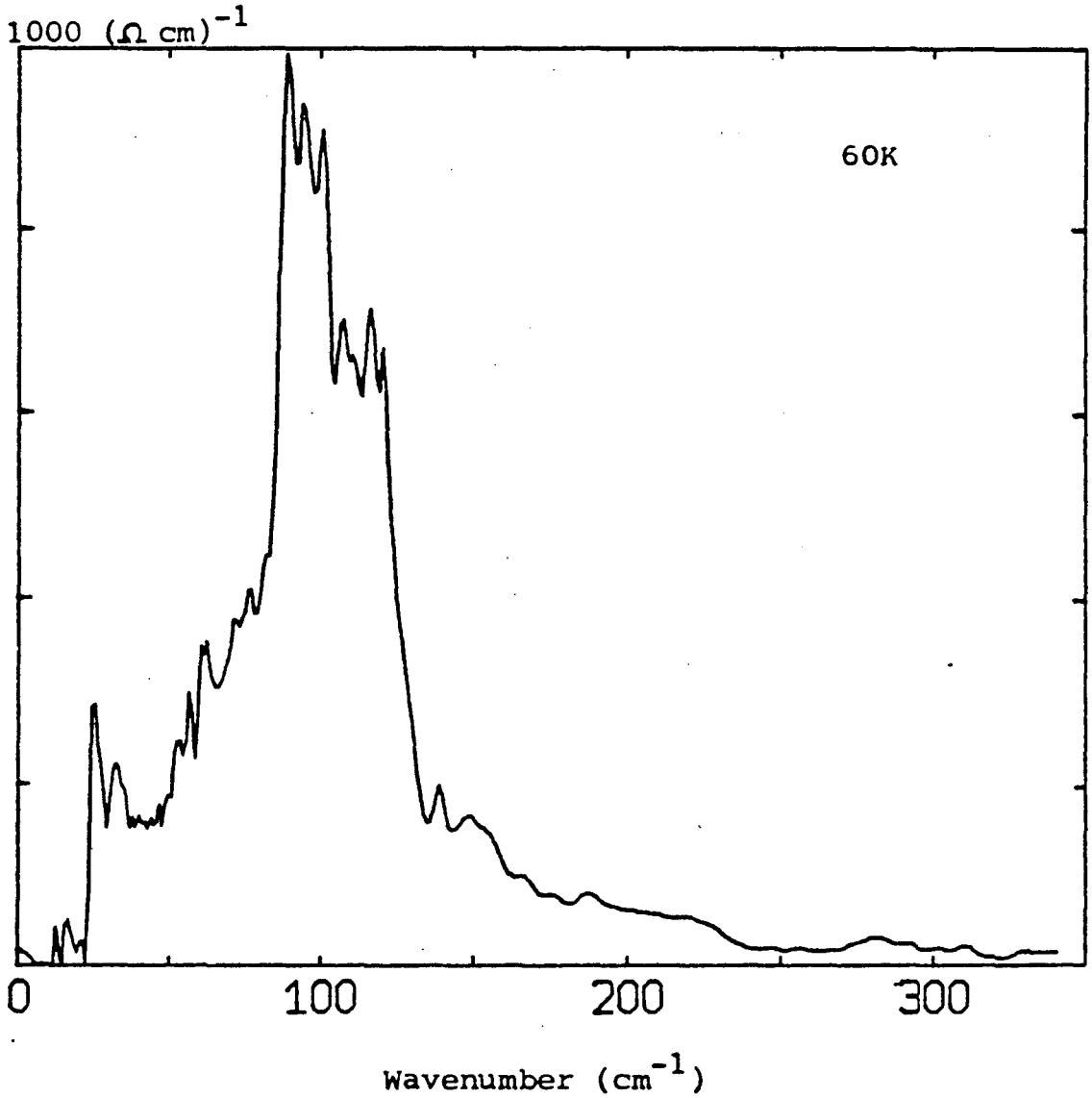

Fig. 36. $\sigma_1(\omega)$ computed from a Kramers-Kronig analysis of the reflectance of $(TMTSF)_2ClO_4$ at 60K for radiation polarized parallel to the fiber axis, with the adjustable parameter equal to 1000 cm^{-1}.

frequencies is larger with the 2000 cm^{-1} cutoff, which is in better agreement with a Drude fit[1] to the reflectance measured above 5000 cm^{-1}.

The real part of the dielectric function at 2K and 60K is shown in Figs. 37 and 38 using a cutoff frequency for the adjustable parameter of 2000 cm^{-1}. The peaks in $\sigma_1(\omega)$ give rise to large dispersions in the dielectric function. At the lowest frequencies, the dielectric function is becoming strongly negative, as is expected for a metal.

If the measured reflectance has been incorrectly normalized at the lower frequencies, there will be a corresponding error in the computation of the optical constants. If we assume that there is a linear error in the normalization of the reflectance at frequencies below 100 cm^{-1} and that the reflectance at 25 cm^{-1} is actually ~98 percent, then the corrected reflectance at 2K and 60K is shown in Figs. 39 and 40. The optical constants obtained from the Kramers-Kronig analysis of the modified reflectances with the cutoff frequency for the adjustable parameter equal to 2000 cm^{-1} are shown in Figs. 39-42. In this case, the maximum conductivity of the 25 cm^{-1} peak is larger than for the unmodified data, but the total oscillator strength is still smaller than in the peak in the conductivity above 100 cm^{-1}.

The conductivity calculated from the measured reflectance of the PF_6 salt is very similar to our results for the ClO_4 salt.[2] In particular, the broad dip in the FIR reflectance of the PF_6 salt at

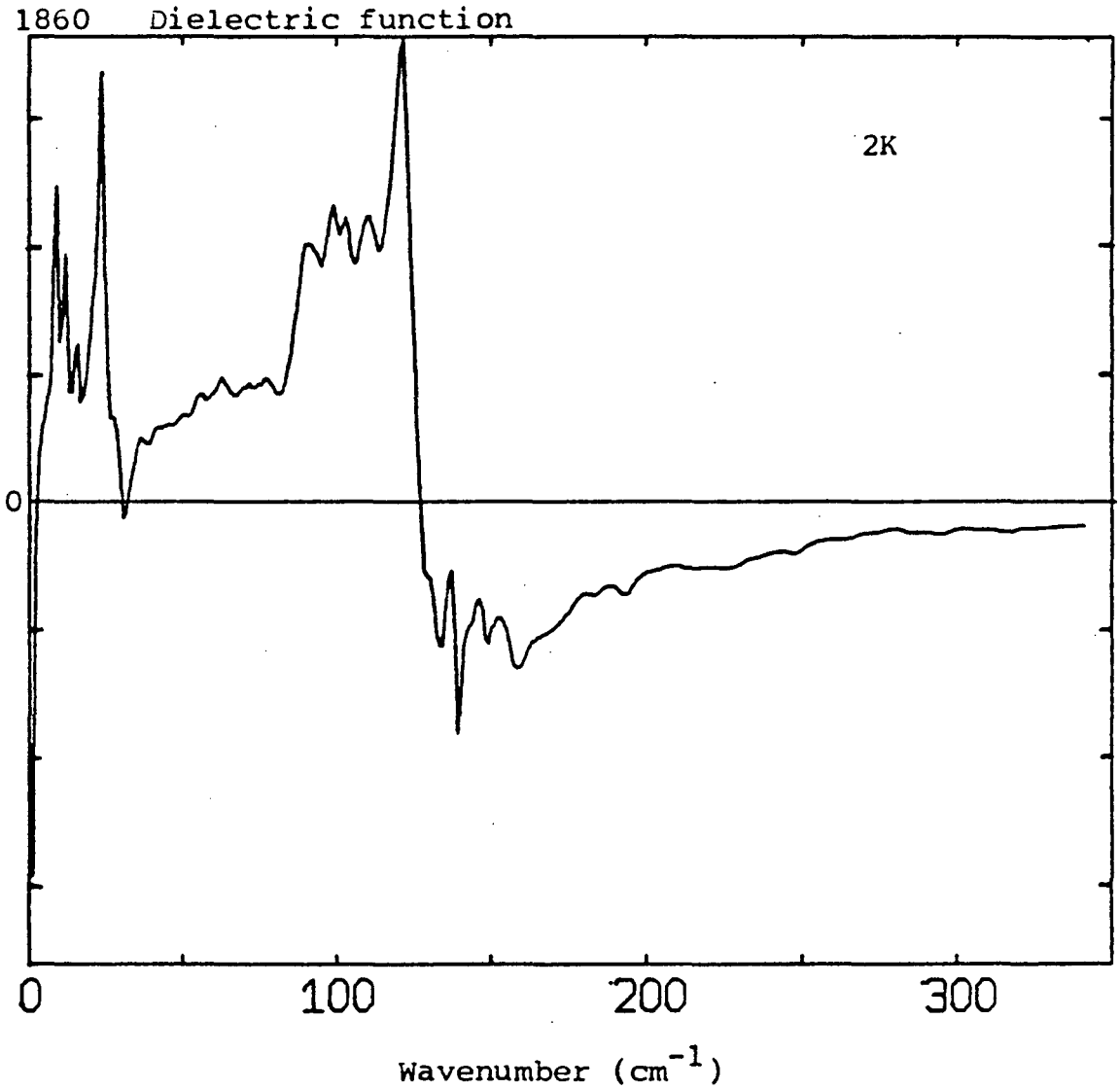

Fig. 37. $\epsilon_1(\omega)$ from a Kramers-Kronig analysis of the reflectance of $(TMTSF)_2ClO_4$ at 2K with an adjustable parameter equal to 2000 cm^{-1}.

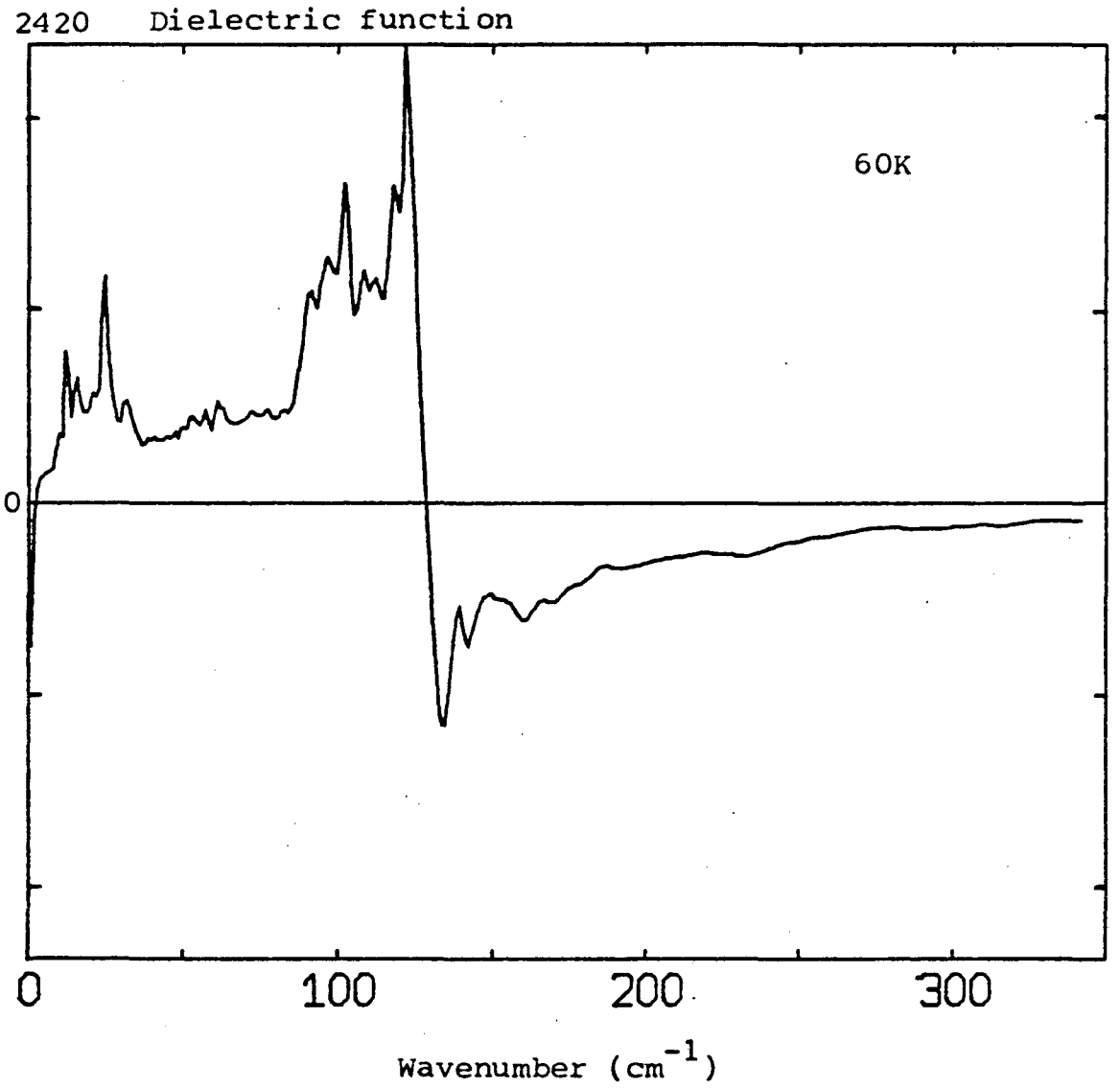

Fig. 38. $\epsilon_1(\omega)$ from a Kramers-Kronig analysis of the reflectance of $(TMTSF)_2ClO_4$ at 60K with an adjustable parameter equal to 2000 cm^{-1}.

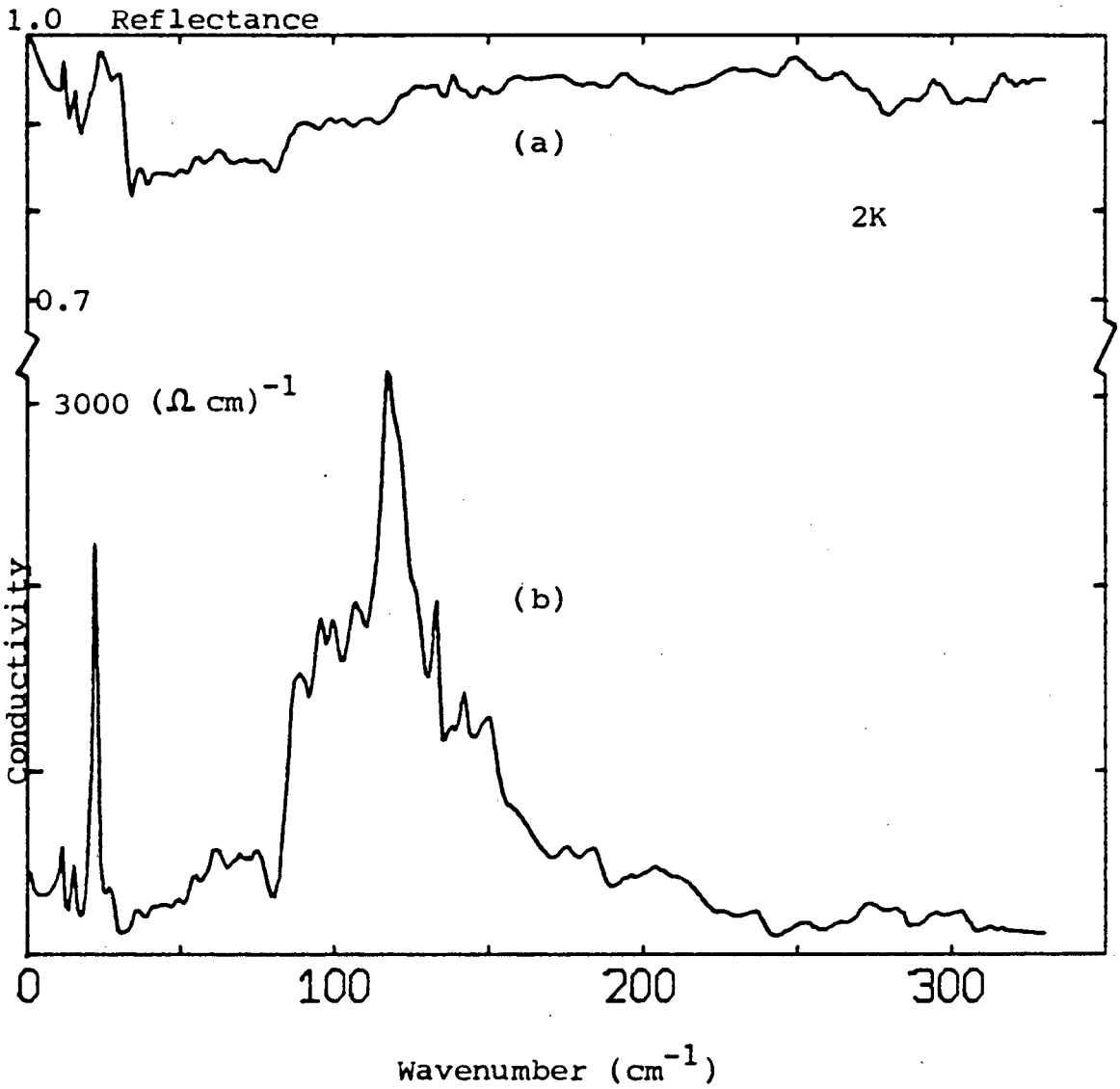

Fig. 39. (a) Modified reflectance at 2K of $(TMTSF)_2ClO_4$ to remove a possible normalization error at low frequencies. (b) $\sigma_1(\omega)$ calculated from this reflectance using an adjustable parameter equal to 2000 cm^{-1}.

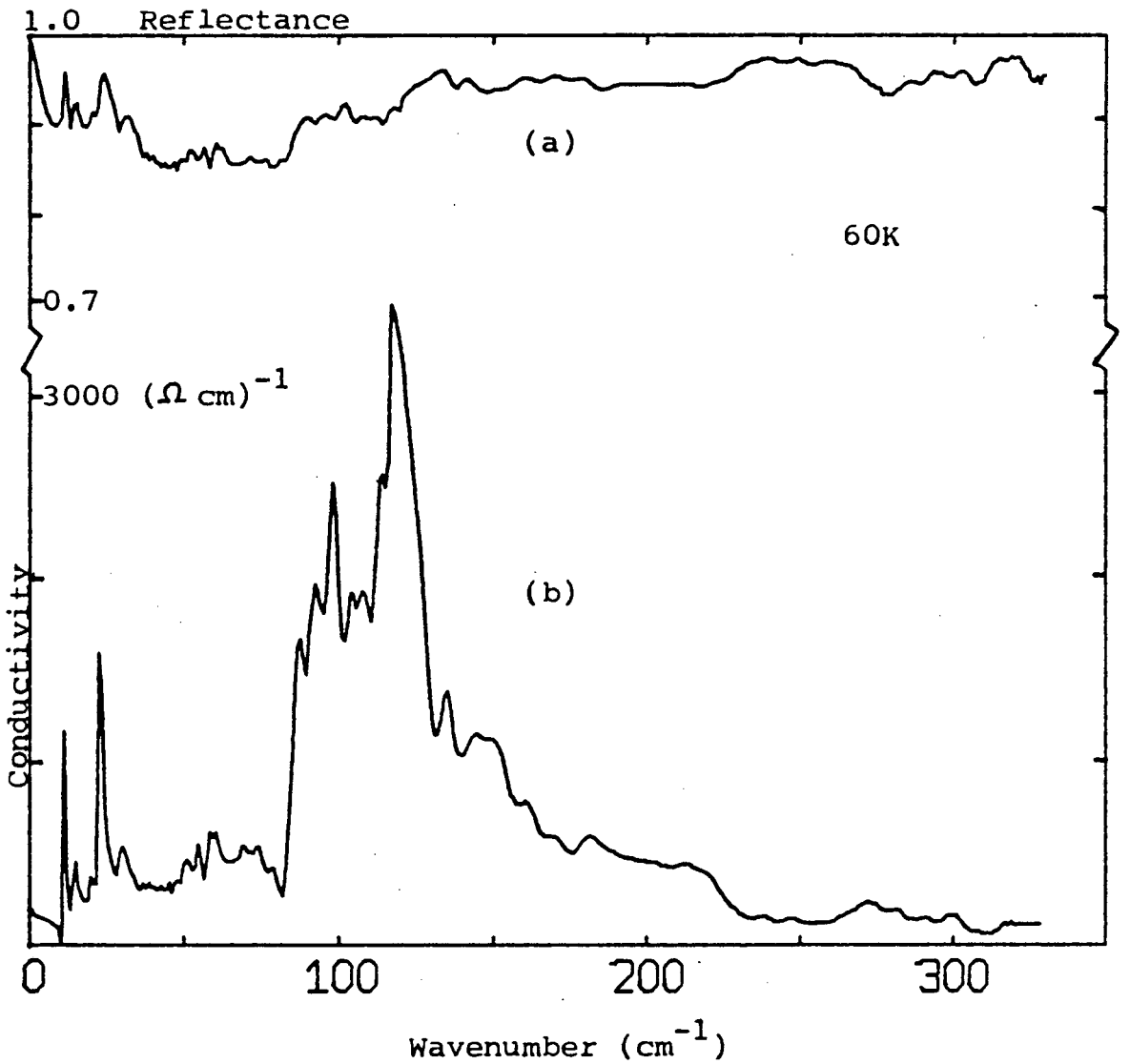

Fig. 40. (a) Modified reflectance at 60K of $(TMTSF)_2ClO_4$ to remove a possible normalization error at low frequencies. (b) $\sigma_1(\omega)$ calculated from this reflectance using an adjustable parameter equal to 2000 cm^{-1}.

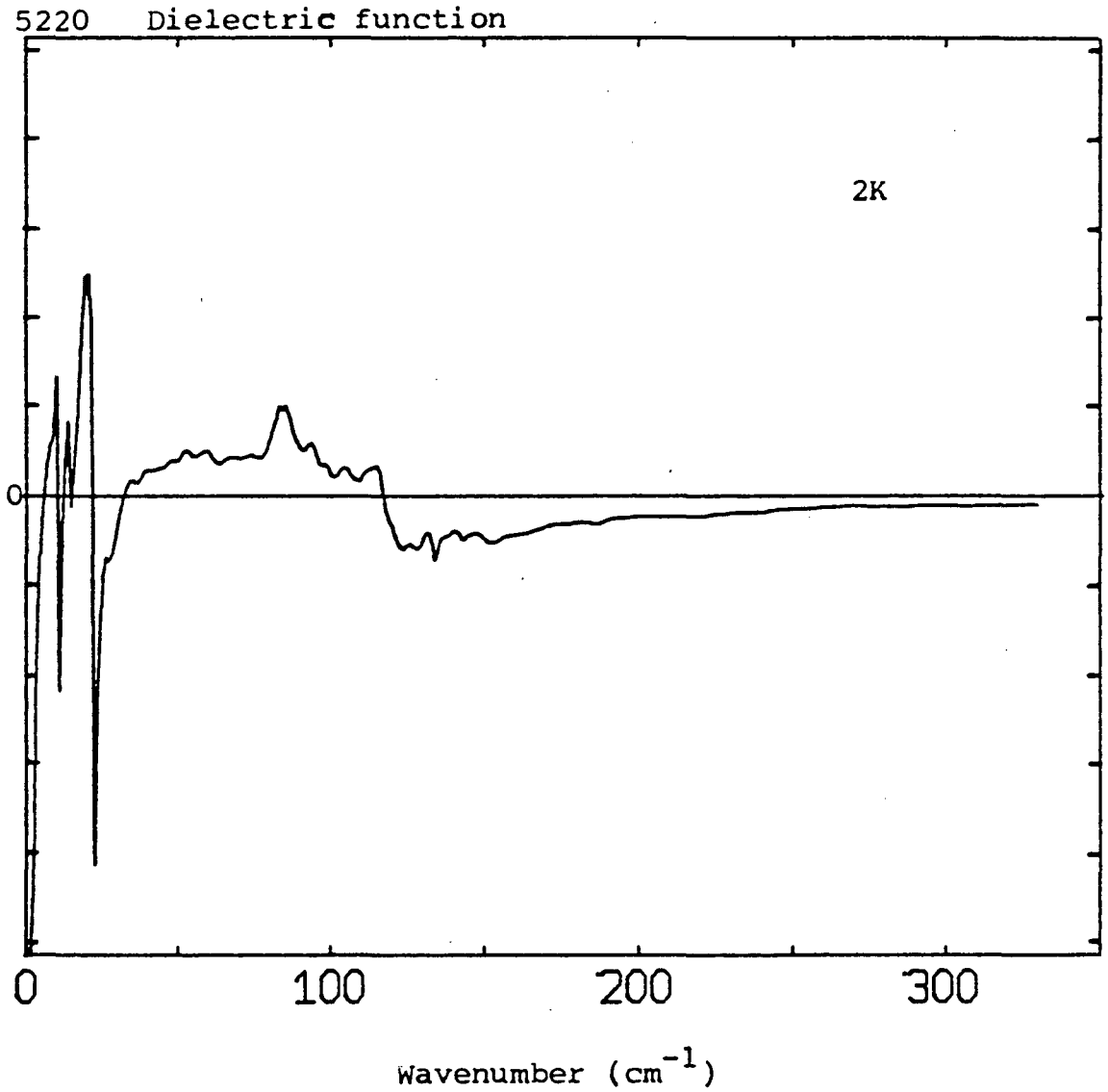

Fig. 41. $\epsilon_1(\omega)$ from a Kramers-Kronig analysis of the reflectance in Fig. 39 of $(TMTSF)_2ClO_4$ with an adjustable parameter equal to 2000 cm^{-1}.

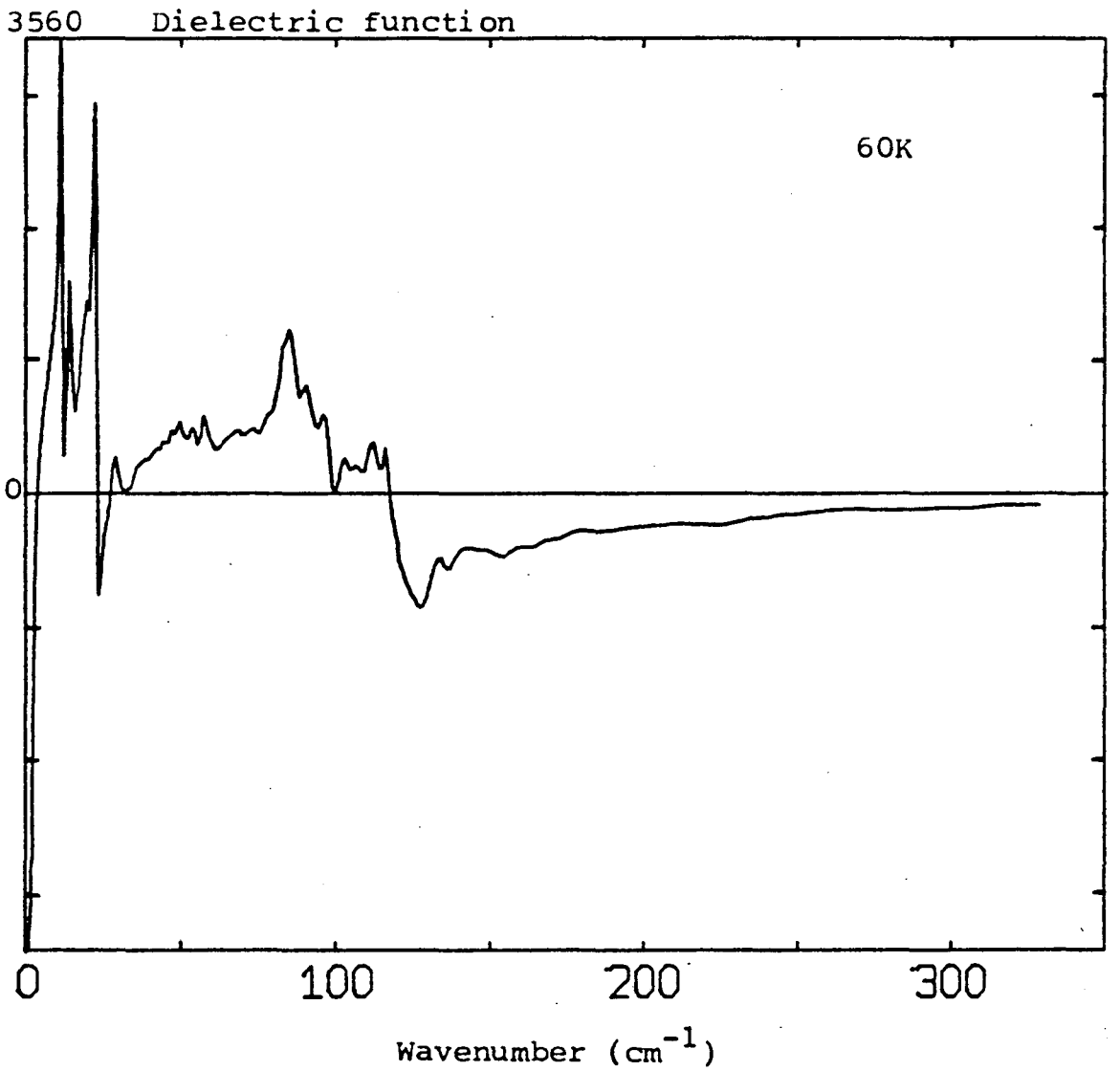

Fig. 42. $\epsilon_1(\omega)$ from a Kramers-Kronig analysis of the reflectance in Fig. 40 of $(TMTSF)_2ClO_4$ with an adjustable parameter equal to 2000 cm^{-1}.

low temperatures results from a large peak in the conductivity, which occurs between 200 and 400 cm^{-1}.

The reflectance for radiation polarized perpendicular to the fibers is considerably smaller than for the parallel polarization. This is expected from the smaller conductivity along the perpendicular axes. Because of the fiber morphology, we believe that the incident light is polarized parallel to the c*-axis for most of the fibers in the sample mosaic when the light is polarized perpendicular to the fibers. It is, however, surprising that the reflectance does not approach unity more quickly at the lower frequencies. This may result from a normalization error in the same way as discussed for the reflectance of light polarized parallel to the fibers.

There is a sharp peak in the reflectance at 29 cm^{-1} for light polarized perpendicular to the fibers at 2K. This peak disappears by 60K. A Kramers-Kronig analysis of the 2K and 60K reflectance, using a cutoff frequency for the adjustable parameter of 500 cm^{-1}, gives the conductivity as shown in Figs. 43 and 44.

Our first reflectance measurements[3] made with unpolarized light below 40 cm^{-1} revealed a second peak in the reflectance at 7 cm^{-1}. Because the reflectance of this sample was dominated in this frequency range by scattering effects of the sample mosaic, the data are shown in Fig. 45 as reflectance ratios. The 7 cm^{-1} peak cannot be clearly identified in the polarized reflectance data, although the rising reflectance below 10 cm^{-1} for light polarized perpendicular to the fibers may be associated with this feature.

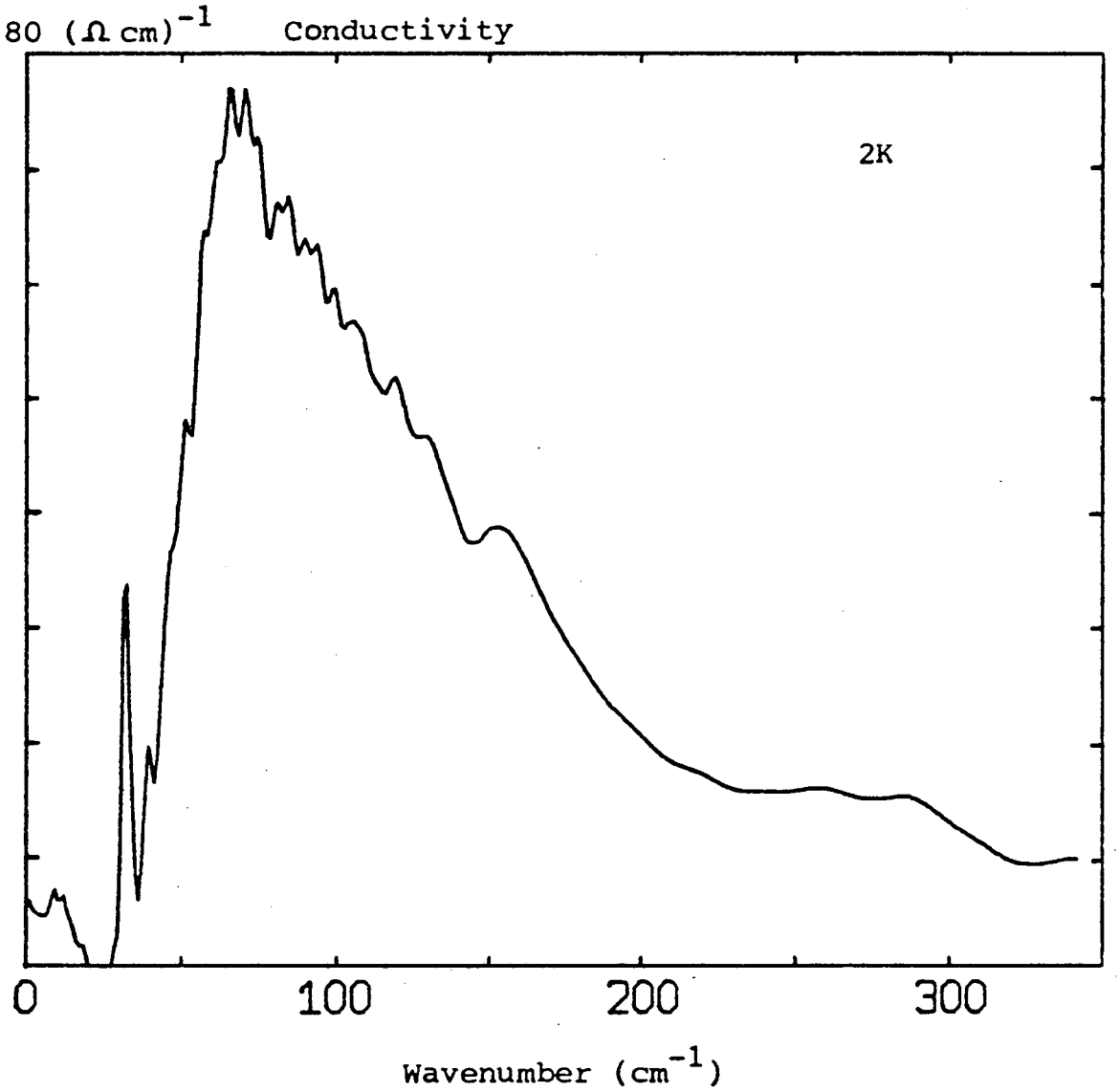

Fig. 43. $\sigma_1(\omega)$ at 2K of $(TMTSF)_2ClO_4$ for radiation polarized perpendicular to the fibers.

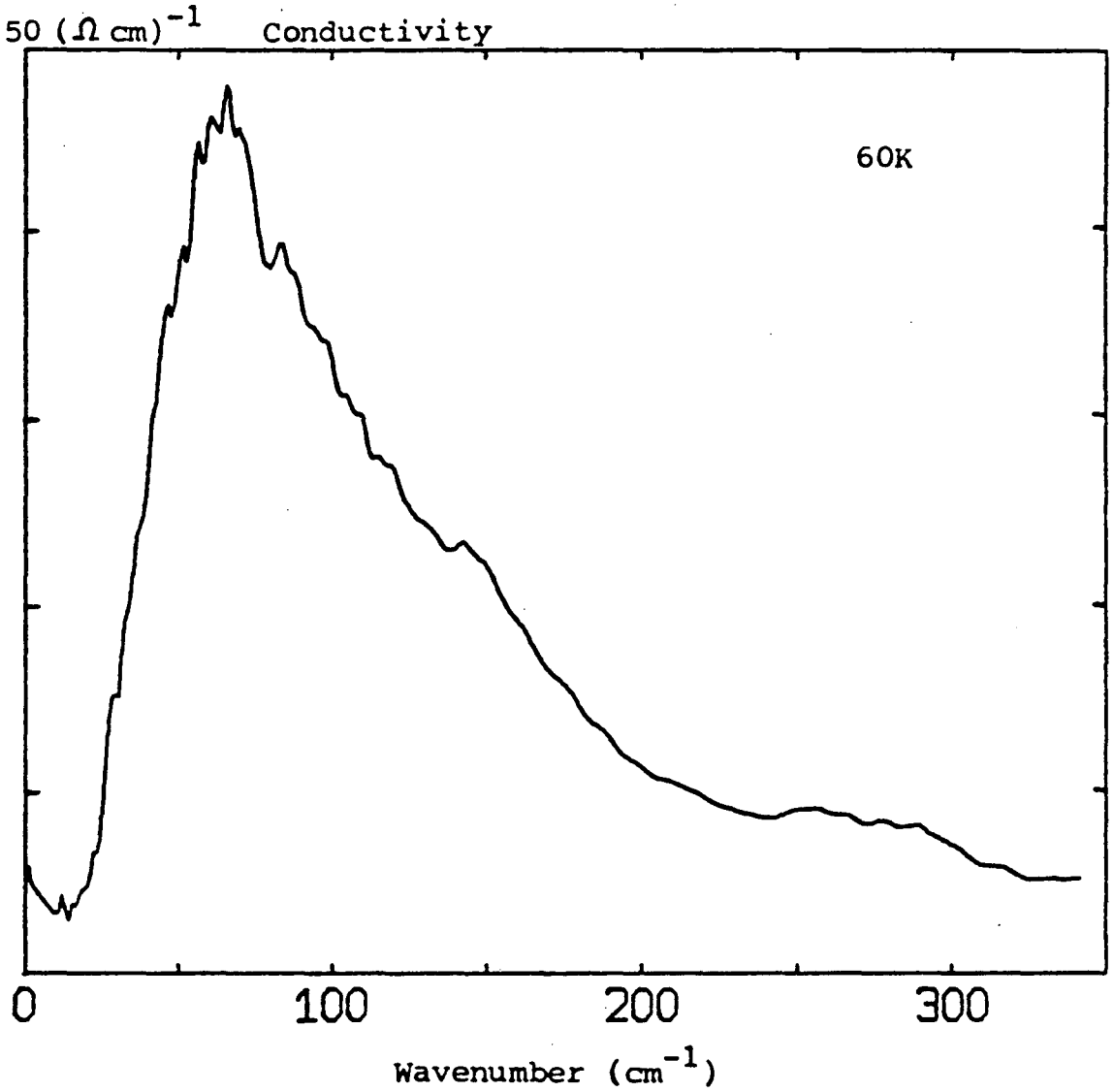

Fig. 44. $\sigma_1(\omega)$ at 60K of $(TMTSF)_2ClO_4$ for radiation polarized perpendicular to the fibers.

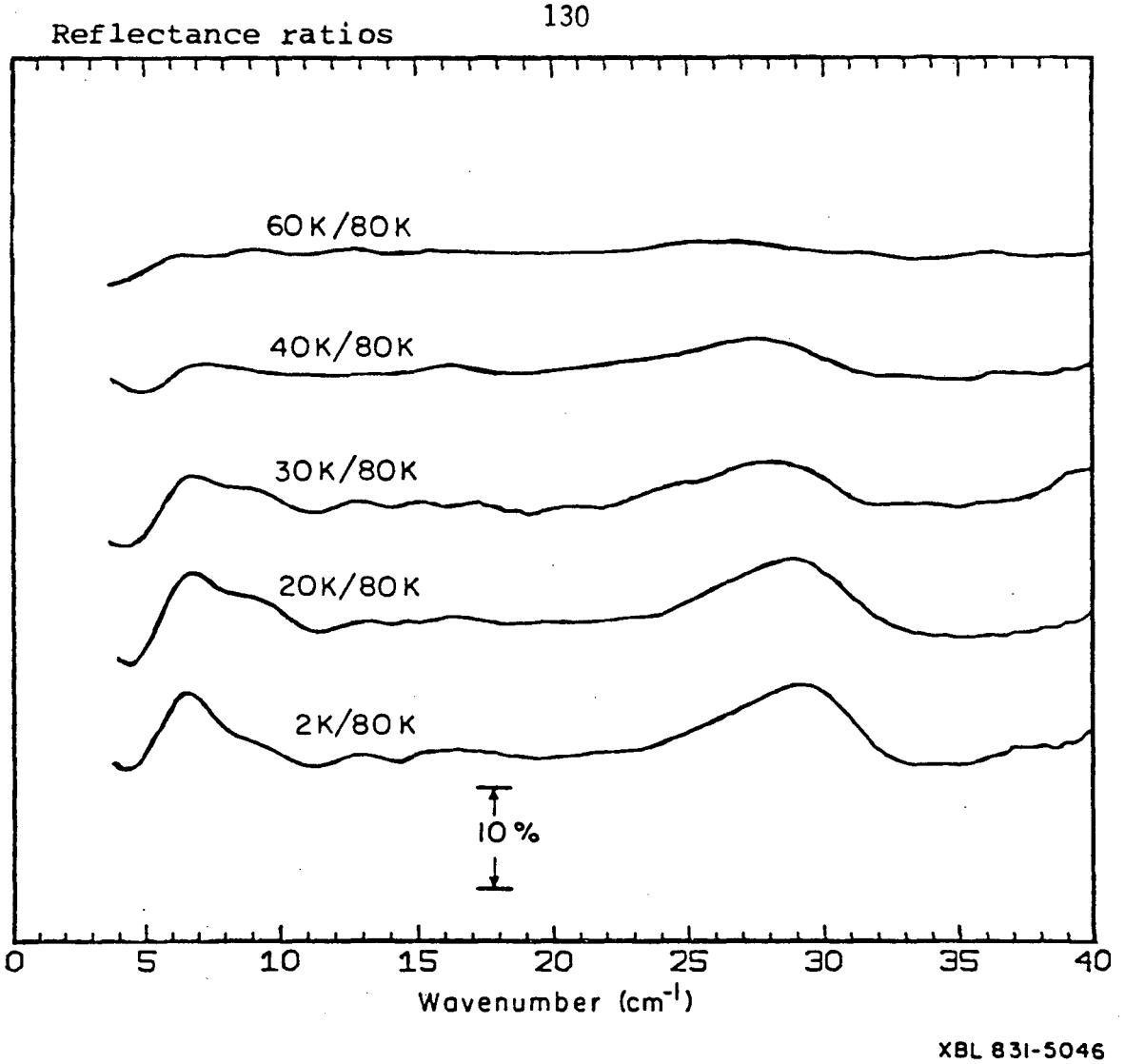

Fig. 45. Ratios of unpolarized reflectance spectra of $(TMTSF)_2ClO_4$ as a function of temperature.

The tunneling measurements on $(TMTSF)_2ClO_4$ indicated a pseudogap of 3 to 4 meV, which was interpreted as evidence for fluctuational superconductivity.[4] Because the peak in the FIR reflectance at 29 cm^{-1} (3.6 meV) occurs within this frequency range, we have studied this feature carefully in several ways. Measurements of the amplitude of the peak as a function of temperature were made for the second thermal cycle of the sample, for radiation polarized parallel to the fibers. When the sample was annealed at 0.1K/min. from 30K, there was a rapid increase in the peak height at the 24K OD transition, as shown in Fig. 46. After measuring the amplitude of the 29 cm^{-1} peak at 2K for the annealed sample, the sample was warmed to 60K, and then quenched at $\geq$10K/min. to <2K to suppress the OD transition. The amplitude of the 29 cm^{-1} feature measured after quenching the sample to <2K, however, was only slightly smaller than the amplitude of the peak measured at <2K after annealing the sample.

The effect on the 29 cm^{-1} feature of cycling the sample between room temperature and liquid helium temperature was also studied. As shown in Fig. 47, there are substantial changes in the overall reflectance and in the shape of the feature at 29 cm^{-1} with thermal cycling of the sample. However, the sharp edge in the reflectance at 30 cm^{-1} is not suppressed by as many as seven thermal cycles of the sample. A Kramers-Kronig analysis of these reflectance changes indicates that the peak in the conductivity at 25 cm^{-1} is decreasing in magnitude with thermal cycling.

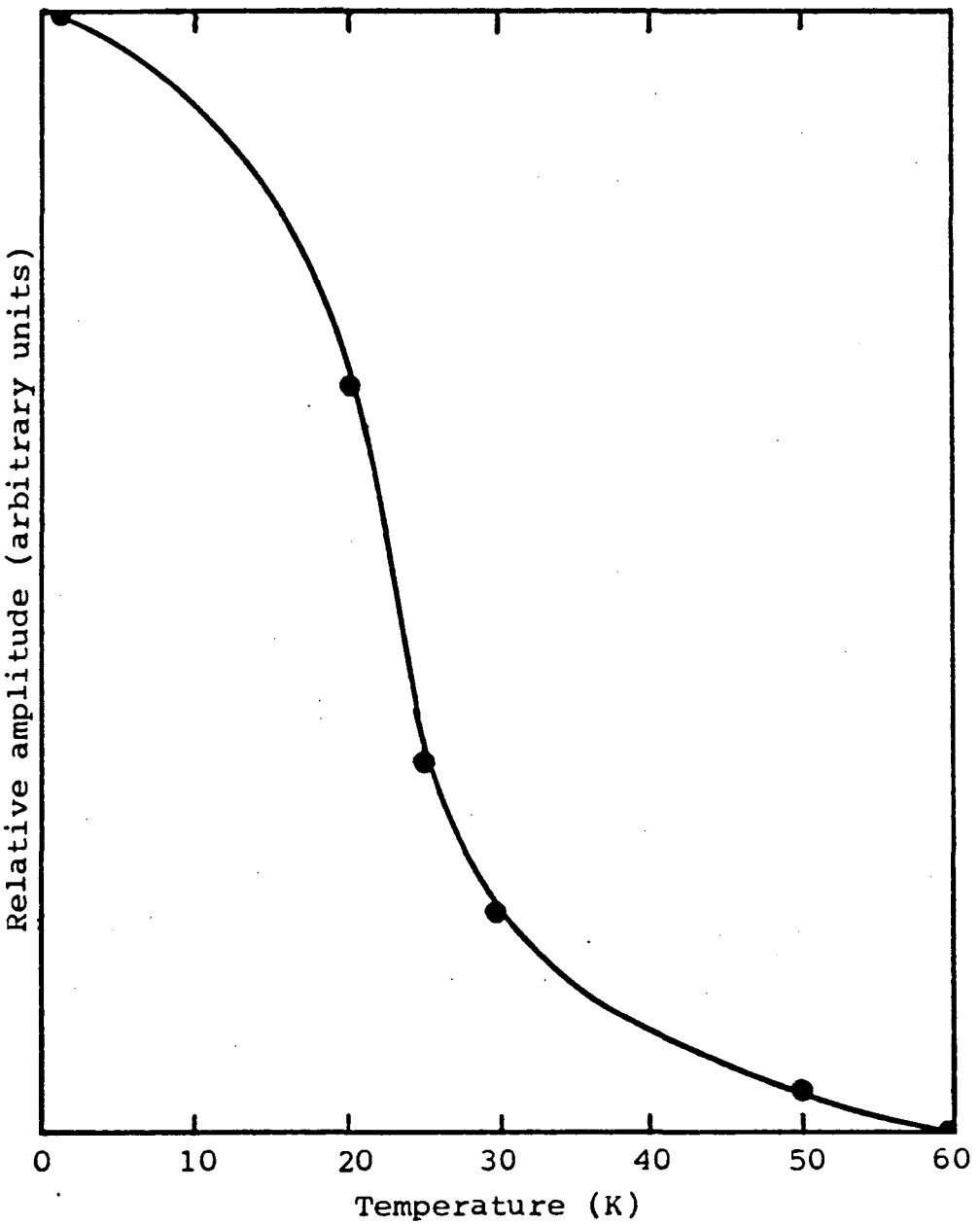

Fig. 46. Relative amplitude of the 29 cm^{-1} peak as a function of temperature when the $(TMTSF)_2ClO_4$ fibers are annealed at 0.1K/min.

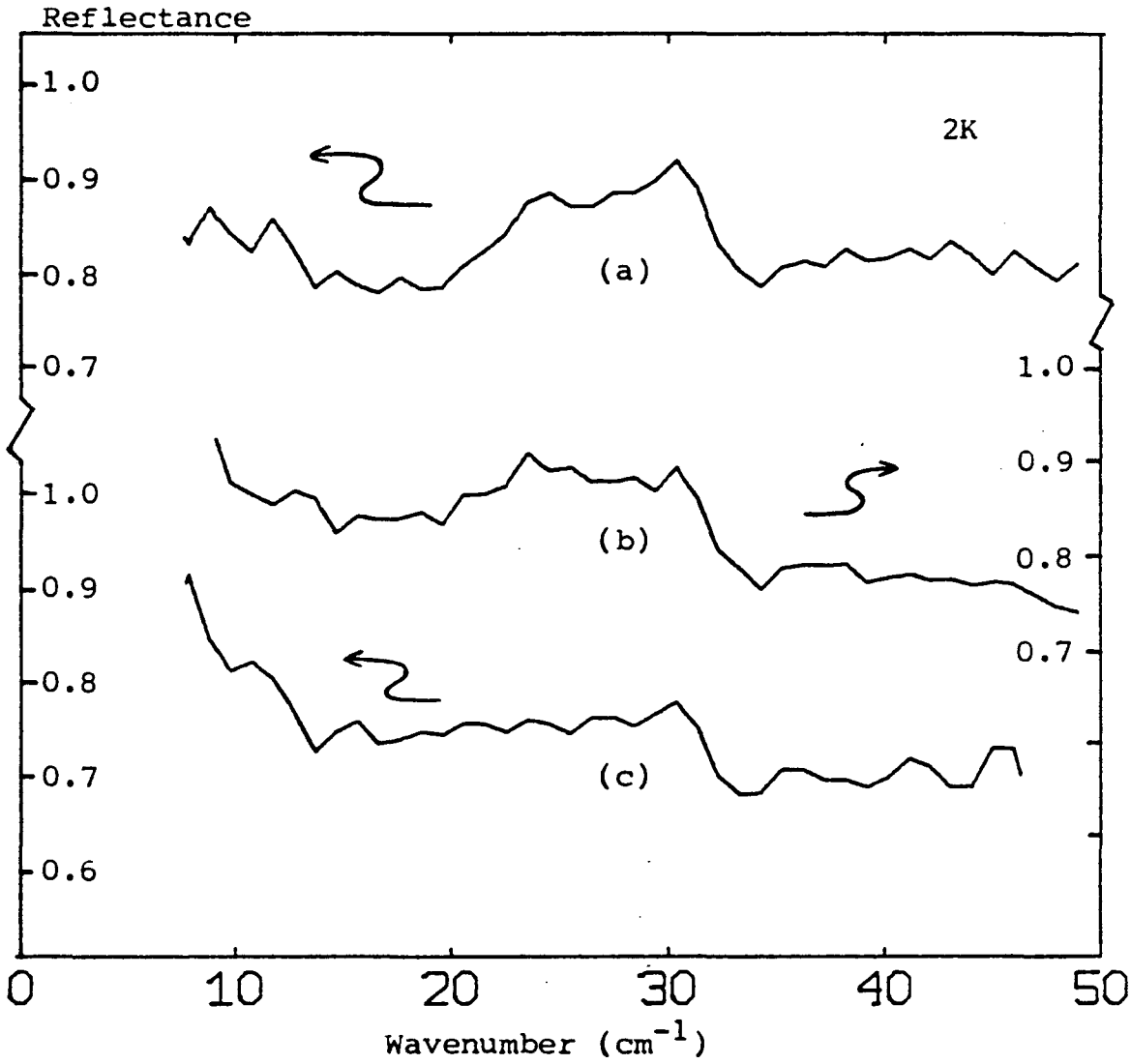

Fig. 47. Effects of thermal cycling upon the feature at 29 cm^{-1} in the reflectance spectrum of $(TMTSF)_2ClO_4$. (a) Second thermal cycle, (b) third thermal cycle, and (c) seventh thermal cycle.

We have also studied the effects of x-ray induced defects upon the 29 cm^{-1} feature. Measurements were made of the reflectance of crystals with no induced defects, crystals with ~100 ppm defects, and crystals with ~1000 ppm defects, on their first thermal cycle. For crystals with no induced defects, the 29 cm^{-1} feature had a peak height of 8 percent at 2K (see Fig. 48). With ~100 pm defects, the peak height was 3 percent, and with ~1000 ppm defects the peak was unobservable above the noise level of 1 percent. These measurements were made using samples composed of crystals from different batches, which might have a small effect upon the peak height of the 29 cm^{-1} feature, independent of the effects of radiation damage.

Transmittance measurements were made on a second sample mosaic in which the fibers were attached with vacuum grease to a copper grid polarizer on a mylar substrate. The fibers were oriented perpendicular to the polarizer so that a crossed-grid arrangement was produced. In this way a large fraction of the light polarized perpendicular to the fibers was prevented from reaching the detector by the copper grid polarizer, thereby increasing the ratio of the light polarized parallel to the fibers to the light polarized perpendicular to the fibers in the detected signal. The fibers were placed in contact with each other to minimize light leakage. The grid constant of the copper polarizer was 3.8μm and the mylar substrate had a thickness of 4μm. Both of these dimensions are much less than the wavelengths of the FIR radiation involved. Fiber dimensions, on the other hand, as well as random inter-fiber spacings were comparable to FIR wavelengths, so structure

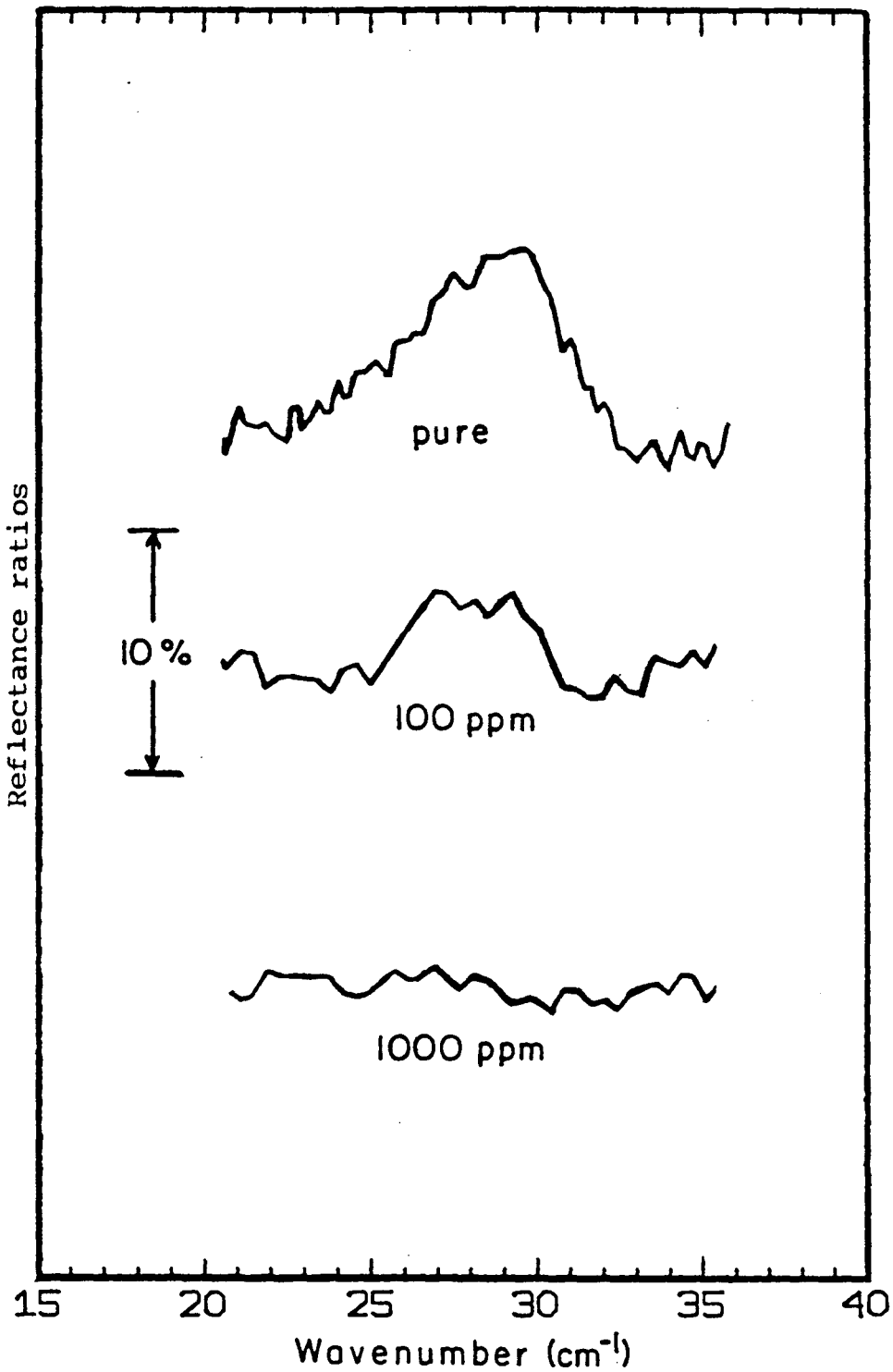

Fig. 48. Effect of x-ray induced defects on the 29 cm^{-1} feature in the reflectance of $(TMTSF)_2ClO_4$. These are ratios of spectra measured at 2K and 80K.

was observed in the spectra from interference effects which could be removed by computing ratios of spectra measured at different temperatures or magnetic fields. Transmittance measurements as a function of temperature were made using the apparatus shown in Fig. 1. Transmittance measurements as a function of applied magnetic field were made using the apparatus shown in Fig. 2. In this apparatus, the sample temperature could also be varied from 2K to ~100K. A carbon resistor attached to the brass light pipe surrounding the sample monitored the sample temperature. Exchange gas was used to obtain temperatures below 20K and to increase the thermal contact between the sample and the thermometer. The magnetic field was oriented perpendicular to the broadest face of the crystal fibers, which was assumed to be parallel to the c*-axis for most of the fibers in the mosaic.

The 29 cm^{-1} feature was present as a peak in the spectrum of the light transmitted through the sample. At 2K the peak height was 12 percent. Because the feature appeared as a peak in the spectrum rather than a dip, this was not simply a transmittance spectrum of bulk material. Instead, the light transmitted through the sample must have been primarily diffracted around the fiber edges. The transmittance of the sample in an applied magnetic field was also studied, but no magnetic effects were found for the 29 cm^{-1} feature. Its transmittance was first measured at high temperatures (above 40K). It was then cooled to liquid helium temperatures, and its transmittance measured again, thereby verifying the presence of the 29 cm^{-1} feature in the

low temperature spectrum. With the sample still at this temperature, magnetic fields of 2 to 40kG were applied parallel to the c*-axis of the fibers, and its transmittance was re-measured. Finally, its transmittance was measured in zero magnetic field, after warming it above 40K. The results of one such experiment are shown in Fig. 49. In this case, the sample was cooled at 0.3K/min from 40K to 15K, before cooling more quickly to 2.3K. To the limit set by the noise level (~1 percent) there is no change in the 29 cm^{-1} feature in an applied field of 10kG. A similar null result was found for applied fields of 2, 10 and 40kG with the sample at 4.2K after quenching from 77K in about one minute.

We can compare our results to other results which have been reported. The peaks in reflectance at 7 and 29 cm^{-1} have also been measured in other experiments.[5] However, in these measurements, the amplitude of the peaks was found to be larger for light polarized parallel to the fibers than perpendicular to the fibers, in contrast to our measurements. In addition, a large difference was found in the amplitude of the 29 cm^{-1} peak between annealing and quenching the sample. We measured only a small difference, but this might be due to the effects of thermally cycling the sample. The 29 cm^{-1} feature was found to shift abruptly by 2 cm^{-1} to lower frequencies upon warming the sample through the 24K OD transition, rather than rapidly but continuously decreasing in amplitude, as in our measurements. This difference may again result from the effects of thermally cycling the sample. Unfortunately, none of our reflectance measurements were made

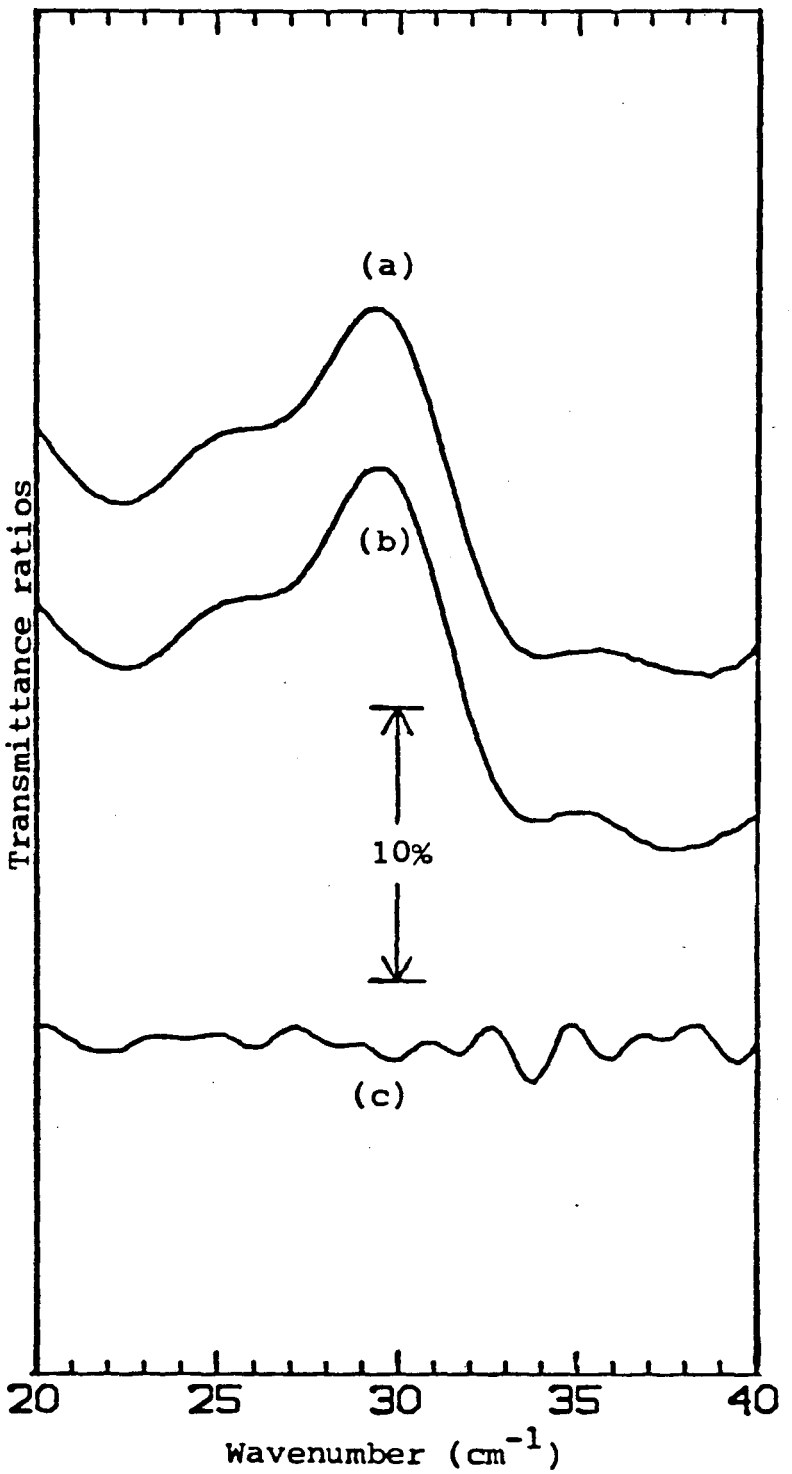

Fig. 49. Effect of a magnetic field on the 29 cm^{-1} feature in $(TMTSF)_2ClO_4$. (a) Ratio of 80K to 2K spectra in no field, (b) ratio of 80K spectrum in no field to 2K spectrum in a 10kG field, (c) ratio of 2K spectrum in no field to 2K spectrum in 10kG field

on the first thermal cycle of the sample. Repeated thermal cycling of the sample was found to have a large effect upon the reflectance of the 29 cm^{-1} feature, similar to our results.

At frequencies above 30 cm^{-1}, the reflectance for light polarized parallel to the fibers was not found to increase,[5] in contrast to our measurements and those reported for the PF_6 salt.[2] A Kramers-Kronig analysis of their reflectance measurements gave two sharp peaks in the conductivity corresponding to the peaks in the reflectance at 7 and 29 cm^{-1} and a continuous increase in the conductivity for frequencies above 30 cm^{-1}. We obtain a continuous increase in the conductivity above 30 cm^{-1} only when we use a high frequency reflectance extrapolation in the Kramers-Kronig transform which is probably not justified.

Magnetic field measurements for both the reflectance[5] and the transmittance[6] of the feature at 29 cm^{-1} were reported. These indicated that a magnetic field of 2kG was sufficient to greatly suppress the amplitude of the feature, in contrast to our measurements in which no magnetic field dependence was found.

There are many similarities and differences between our measurements and the others reported in this section. The difficulties in accurately normalizing measurements made upon sample mosaics may explain some of the differences. Thermal cycling of the sample probably also plays an important role, causing significant changes in the FIR properties of $(TMTSF)_2ClO_4$ below 50 cm^{-1}. The source of the samples is another difference, but this is probably not important

in the FIR measurements. In the magnetic field measurements, the sample cooling rates and sample operating temperatures were also slightly different, and may be important in explaining the differences between the measurements.

The interpretation of our FIR measurements is difficult. Although the Kramers-Kronig analysis of the reflectance may indicate a pseudogap in the conductivity below 30 cm^{-1} (4meV) at 2K and 60K, it cannot be used to support a theory of fluctuational superconductivity. Superconducting fluctuations are supposed to vanish by ~40K. However, the Kramers-Kronig analysis indicates little change in the conductivity up to 60K. The large peak in the conductivity at $\geq$100 cm^{-1}, which causes the reflectance to increase to >95 percent in this frequency range, is quite unusual. A similar peak in the conductivity of the PF_6 salt was reported but not explained.[2] If the results of the ClO_4 salt and the PF_6 salt are related, then the peak in the conductivity is not associated with anion ordering. SDW transitions do occur in both materials, and should give rise to an energy gap. However, for a SDW transition at ~5.5K in the ClO_4 salt, the mean field energy gap equation predicts an energy gap of only 13 cm^{-1}. Moreover, the pseudogap and conductivity peak are present in the ClO_4 salt at least to 60K, and in the PF_6 salt to room temperature, well above the SDW transition temperatures.

We believe that the features in the reflectance at 7 and 29 cm^{-1} result from coupling between optical phonons and the carriers. Such coupling is possible in materials with CDW's, as discussed for

$NbSe_3$. The ordering of anions below the OD transition induces a CDW in the carrier density. The ReO_4 salt, which undergoes an OD transition at 180K, exhibits many strong phase phonons below this temperature in its infrared spectrum. More significantly, the effects of anion ordering are present at temperatures above the OD transition, as evidenced by the vibrational structure in the spectrum of the ReO_4 salt at room temperature.

Thus, it seems likely that the peaks in the reflectance at 7 and 29 cm^{-1} are phase phonons which obtain IR oscillator strength by means of the OD transition at 24K. This explains the strong increase in the peak intensity when cooling through the ordering temperature. If defects induced by radiation cause a sufficient amount of disorder to suppress the OD transition, then the peak intensity of the 29 cm^{-1} feature would be reduced, as observed. Also, repeated thermal cycles of samples probably create many mechanical deformations in the fibers.[7] Such deformations may partially suppress the anion ordering, which would explain the decrease in the peak height of the 29 cm^{-1} feature with thermal cycling of the sample.

Of course, in our reflectance measurements we were able to measure the 29 cm^{-1} peak in the reflectance regardless of the rate at which the sample was cooled. On the second thermal cycle, the amplitude of the peak was slightly smaller when the sample was quenched, but it was definitely present. Quenching, however, is found to stabilize the SDW state and presumably suppresses the ordered state.[8] If we interpret the 29 cm^{-1} feature as a phase phonon caused by anion ordering, then

we are led to the conclusion that quenching does not totally destroy the anion order. Indeed, magnetoresistance measurements have suggested that quenched samples are inhomogeneous mixtures of ordered and SDW states.[7]

The very low frequency of the features at 7 and 29 cm^{-1} is unusual for phase phonons in organic charge transfer salts. Their frequency is probably too low to be due to intramolecular vibrations. A group theory analysis of the phonon symmetry in the TMTSF molecule and chain structure indicates that there are three librational modes which can couple to the electrons in first-order (see Appendix B), and may therefore become IR-active.

It is difficult to explain a magnetic field dependence of the 29 cm^{-1} feature, if there is one. Further measurements are necessary to clarify this point.

References

1. K. Kikuchi, I. Ikemoto, K. Yakushi, H. Kuroda, K. Kobayashi, Sol. St. Comm. 42, No. 6, 433 (1982).

2. C. S. Jacobsen, D. B. Tanner, K. Bechgaard, Mol. Crys. Liq. Crys. 79, 25 (1982).

3. R. L. Greene, W. A. Challener, P. L. Richards, Bull. Am. Phys. Soc. 27, No. 3, 641 (1982).

4. D. Jérome, H. J. Schulz, Adv. in Phys. 43, 443 (1982).

5. H. K. Ng, T. Timusk, K. Bechgaard, to be published in Les Editions de Physique (1983).

6. H. K. Ng, T. Timusk, J. M. Delrieu, D. Jérome, K. Bechgaard, J. M. Fabre, J. Phys. Lett. 43, L513 (1982).

7. T. Ishiguro, K. Murata, K. Kajimura, N. Kinoshita, H. Tokumoto, M. Tokumoto, T. Ukachi, H. Anzai, G. Saito, preprint.

8. P. Garoche, R. Brusetti, K. Bechgaard, Phys. Rev. Lett. 49, No. 18, 1346 (1982).

IX. Conclusion

We have made FIR measurements upon the quasi-one-dimensional materials $NbSe_3$ and $(TMTSF)_2ClO_4$. For $NbSe_3$, we have used our measurements to estimate carrier concentrations, electron-phonon coupling constants, and the size of a CDW energy gap. We have made the first observation of a Fano antiresonance of a coupled electron-optical phonon mode above a CDW energy gap for an inorganic CDW material. We have used our measurements to distinguish between the classical and tunneling models of CDW transport, finding that our data support the latter model.

Our FIR results for $NbSe_3$ suggest that similar measurements on the CDW material TaS_3 would also be interesting. This material has a larger CDW energy gap and becomes semiconducting below its transition temperature. It also exhibits electrical transport by sliding CDW's and would therefore be another opportunity for using FIR measurements to distinguish between the models of CDW transport.

It would also be very interesting to study the low temperature Raman spectrum of $NbSe_3$. If our identification of the phonons in the FIR spectrum as phase phonons is correct, then each phase phonon should be associated with an amplitude phonon which is Raman-active. A comparison of the phase phonon and amplitude phonon frequencies can be used as an independent check of our estimates of electron-phonon coupling constants.

We have shown for $(TMTSF)_2ClO_4$ that the FIR conductivity is inconsistent with an interpretation in terms of fluctuational

superconductivity. There are many aspects of the FIR data of $(TMTSF)_2ClO_4$ which are not understood at present, however. Future research should resolve the question of the magnetic nature of the 29 cm^{-1} feature. Studies of the FIR spectra of $(TMTSF)_2PF_6$ and $(TMTSF)_2ReO_4$ below 50 cm^{-1} may also be able to provide more information about the 29 cm^{-1} feature in the ClO_4 salt. The ReO_4 salt undergoes an OD transition, while the PF_6 salt undergoes a SDW transition. Further work is also necessary to understand the origin of the large peak in the conductivity at frequencies above 100 cm^{-1} in the ClO_4 and the PF_6 salts.

Appendix A: The dielectric function

The dielectric function of a solid relates the polarization induced in the solid, $\vec{P}(\omega,\vec{k})$ to the externally applied electric field, $\vec{E}(\omega,\vec{k})$. In general, the dielectric function is a tensor, and the governing relation is

$$(\tilde{\epsilon} - 1)\,\vec{E} = 4\pi\vec{P} \quad . \tag{1}$$

For isotropic solids, the dielectric function is a scalar, and this equation reduces to

$$\epsilon = 1 - 4\pi P/E. \tag{2}$$

The interaction of IR radiation with solids is determined by the long wavelength limit ($\vec{k} = 0$) of the dielectric function, because the wavelength of the IR radiation is so large that the incident light samples ~10^3 to 10^7 unit cells of the crystal. The wavevector of IR photons is only ~10^{-3} to 10^{-7} that of the wavevector at the edge of the Brillouin zone in a crystal, and thus the momentum transfer to elementary excitations in the solid from IR photons is generally negligible.

In this section we discuss the method of obtaining the dielectric function from optical measurements by use of the Kramers-Kronig relations, and how the dielectric function may be analyzed by the use of simple physical models, like the Drude and Lorentz models, to provide more detailed information about the crystal.

The reflectance and transmittance for radiation at a boundary between two media with differing polarizabilities is well known.[1] When the radiation is incident normally upon a surface with dielectric constant ϵ and permittivity $\mu = 1$ from a vacuum, the reflectance is related to the complex index of refraction by the equation

$$R = \frac{(n-1)^2 + K^2}{(n+1)^2 + K^2} \tag{3}$$

where the index of refraction is $N = n + iK$. The dielectric function and the index of refraction are related by the equations

$$\epsilon = (n^2 - K^2) + i(2nK) \tag{4}$$

$$n^2 = \frac{1}{2}\epsilon_1 + \frac{1}{2}\sqrt{\epsilon_1^2 + \epsilon_2^2} \tag{5}$$

$$K^2 = -\frac{1}{2}\epsilon_1 + \frac{1}{2}\sqrt{\epsilon_1^2 + \epsilon_2^2}\,. \tag{6}$$

By use of Eqs. (3) - (6), it is possible to investigate systematically the relationship between the complex dielectric function and the single-surface reflectance, as shown in Figs. 50-52. For a given value of the reflectance, there is a minimum and maximum value possible for ϵ_1, and a maximum value possible for ϵ_2. The minimum value possible for ϵ_2 is always zero for any value of the reflectance. If the reflectance of a material is known, limits can be immediately placed upon the dielectric function without recourse to a

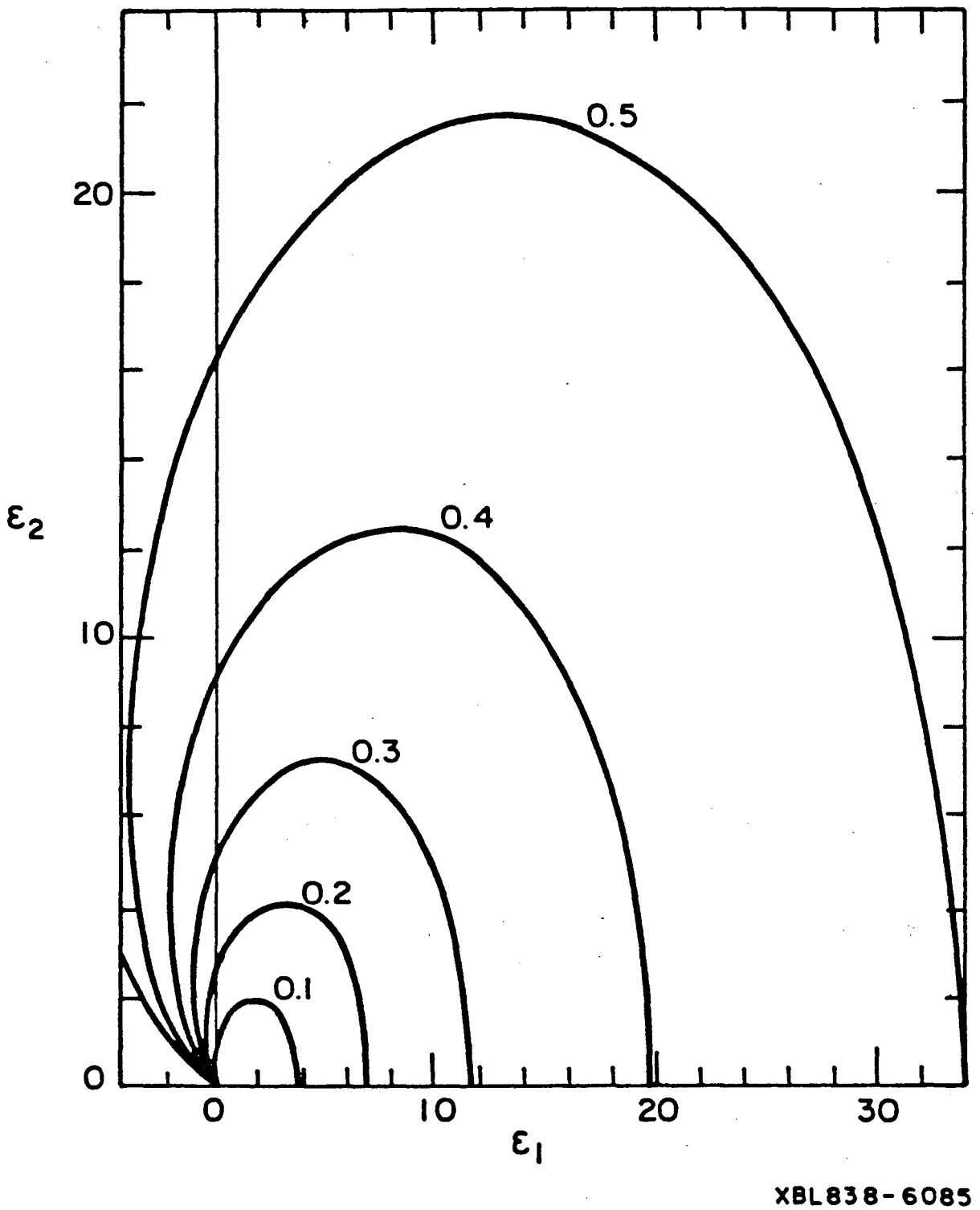

Fig. 50. Reflectance contours on a map of the real and imaginary parts of the dielectric function.

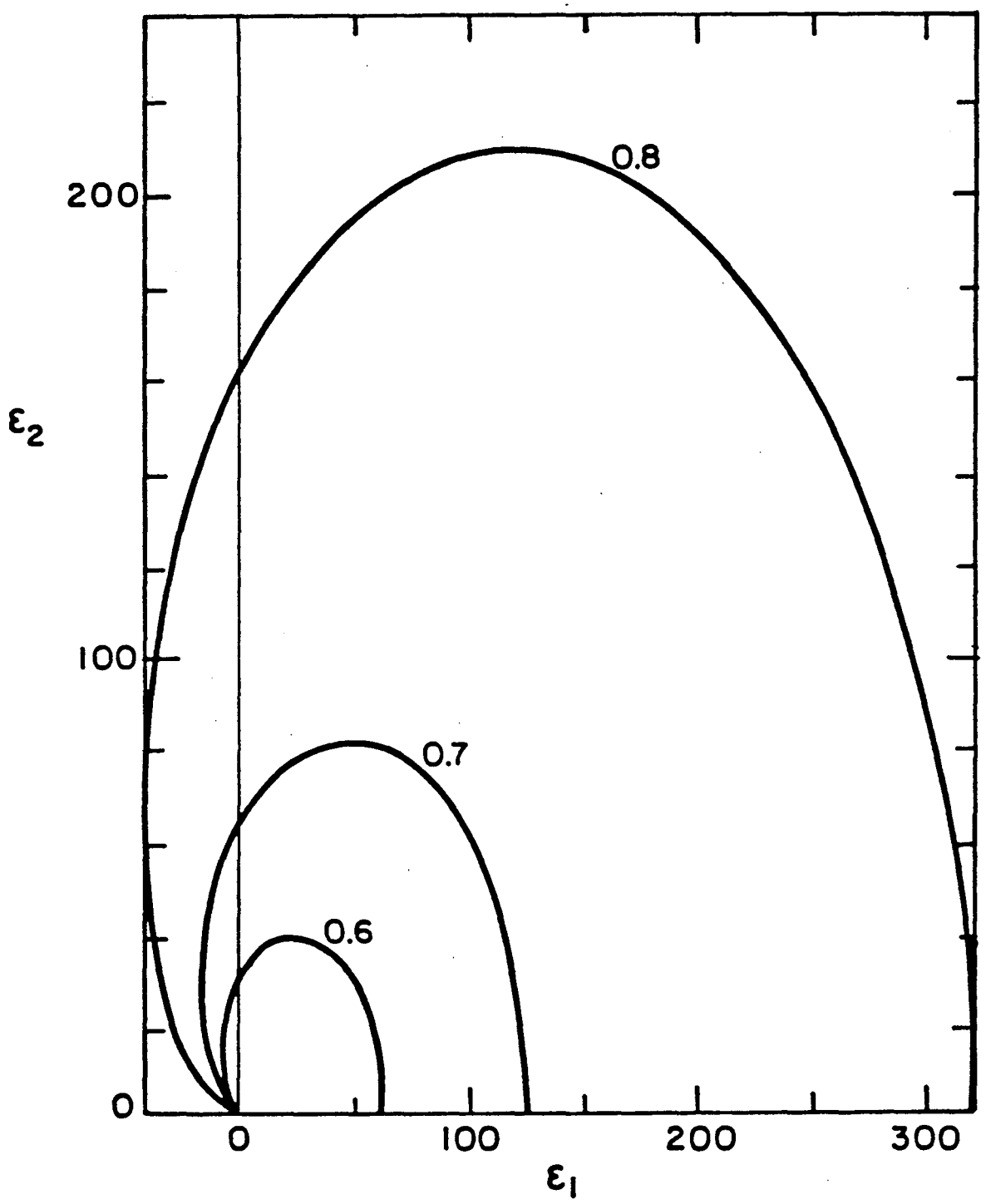

XBL 838-6086

Fig. 51. Reflectance contours on a map of the real and imaginary parts of the dielectric function.

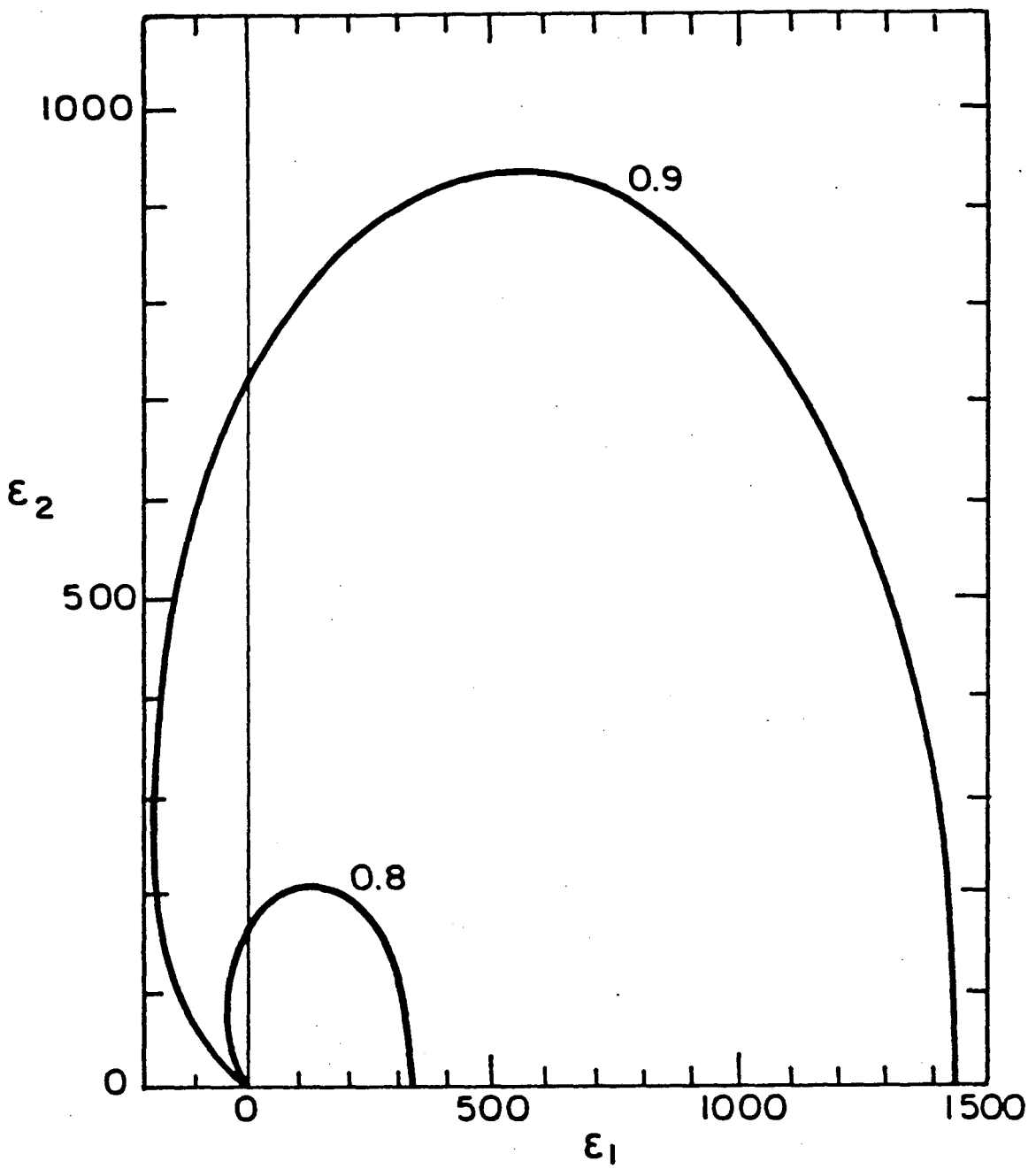

Fig. 52. Reflectance contours on a map of the real and imaginary parts of the dielectric function.

more complicated analysis. This assumes, of course, that the material is thick enough that the single-surface reflectance equations apply.

The amplitude of the electric field upon reflection from a single-surface can be expressed in terms of the total reflectance and the angle of phase shift. It can also be expressed in terms of the complex index of refraction. The relations are

$$r = \sqrt{R}\, e^{i\theta} = \frac{n - 1 + iK}{n + 1 + iK} \quad . \tag{7}$$

This equation leads to the following four important relations:

$$n = \frac{1 - R}{1 + R - 2\sqrt{R}\cos(\theta)} \tag{8}$$

$$K = \frac{2\ R\ \sin(\theta)}{1 + R - 2\sqrt{R}\cos(\theta)} \tag{9}$$

$$\varepsilon_1 = \frac{(1-R)^2 - 4\ R\ \sin^2(\theta)}{[1 + R - 2\sqrt{R}\ \cos(\theta)]^2} \tag{10}$$

$$\varepsilon_2 = \frac{4\sqrt{R}\ (1-R)\ \sin(\theta)}{[1 + R - 2\sqrt{R}\cos(\theta)]^2} \quad . \tag{11}$$

The equations which relate the complex dielectric function to the complex conductivity are also important. The Maxwell equation $c\ \mathrm{curl}(\vec{H}) = -i\omega\varepsilon(\omega)\vec{E}$ can also be written as $c\ \mathrm{curl}(\vec{H}) = 4\pi\sigma(\omega)\vec{E} - i\omega\vec{E}$. Defining $\sigma = \sigma_1 - i\sigma_2$, we get

$$\varepsilon_2 = \left(\frac{4\pi}{\omega}\right)\sigma_1 \tag{12}$$

and

$$\varepsilon_1 = 1 + \left(\frac{4\pi}{\omega}\right)\sigma_2 \quad . \tag{13}$$

It is often desirable to display the optical constants of a material in terms of σ_1 and ε_1, rather than ε_1 and ε_2, although the information is equivalent.

The Kramers-Kronig relations are a useful set of dispersion relations for obtaining values for the dielectric function from experimentally measured reflectances of solids, and for obtaining general sum rules for the optical constants of solids. In any linear system obeying causality, the dispersive process will be related to the absorptive process through a Kramers-Kronig relation. The Kramers-Kronig relations for the dielectric function are:[2]

$$\varepsilon_1 - 1 = \frac{2}{\pi} P \int_0^\infty \frac{\omega' \varepsilon_2(\omega')}{\omega'^2 - \omega^2} d\omega' \tag{14}$$

and

$$\varepsilon_2 = \frac{4\pi\sigma_{dc}}{\omega} - \frac{2\omega}{\pi} P \int_0^\infty \frac{\varepsilon_1(\omega') - 1}{\omega'^2 - \omega^2} d\omega' \quad . \tag{15}$$

The Kramers-Kronig relations relating the reflectance to the angle of phase shift upon reflection are:

$$\theta(\omega) = \frac{\omega}{\pi} \int_0^\infty \frac{\ln R(\omega') - \ln R(\omega)}{\omega'^2 - \omega^2} d\omega' \tag{16}$$

and

$$\ln\left[\frac{R(\omega)}{R(\nu)}\right] = \frac{2}{\pi} \int_0^\infty \omega' \theta(\omega') \left[\frac{1}{\omega'^2 - \omega^2} - \frac{1}{\omega'^2 - \nu^2}\right] d\omega' \quad . \tag{17}$$

Eq. (17) can be simplified for metals, because the reflectance is unity at zero frequency,

$$\ln R(\omega) = \frac{2}{\pi} \int_0^\infty \theta(\omega') \frac{\omega^2}{\omega'(\omega'^2 - \omega^2)} d\omega' \quad . \tag{18}$$

A sum rule for the conductivity or oscillator strength of solids can be derived from these results. At sufficiently high frequencies, all of the electrons in a solid will respond to an electric field as free electrons with a dielectric function of

$$\epsilon_1 \cong 1 - \frac{\omega_p^2}{\omega^2} \tag{19}$$

where

$$\omega_p^2 = \frac{4\pi n e^2}{m} \quad . \tag{20}$$

Combining Eqs. (12), (14), and (19) gives the sum rule,

$$\int_0^\infty \sigma_1(\omega) d\omega = \frac{\omega_p^2}{8} \quad . \tag{21}$$

The total area under the conductivity vs. frequency curve is constant and determined by the plasma frequency, ω_p. This sum rule was originally applied[3] to the analysis of the frequency dependence of the conductivity of superconductors.

Although the Kramers-Kronig relations are a powerful tool for obtaining the dielectric function from the reflectance, they must be used carefully, because exact results are not possible when the reflectance data exist over only a finite frequency range. Extrapolations are necessary to make use of the Kramers-Kronig relations, and these will introduce error into the calculations.

The most serious errors result from using poor extrapolations for the reflectance above the highest measured frequency of the data, ω_b. Two different extrapolations are commonly employed.[2,4] The exponential extrapolation is given by

$$R(\omega) = R_b \exp[A(\omega_b - \omega)] \qquad (\omega_c > \omega > \omega_b) \quad , \tag{22}$$

where R_b is the reflectance measured at ω_b. The constant A is usually chosen to make the derivative of the extrapolated reflectance equal to the derivative of the measured reflectance at ω_b. The integration must be truncated at some upper frequency ω_c or the integral will diverge. This frequency is an adjustable parameter chosen to make the calculated dielectric function as close as possible to an independent measurement of the dielectric function at one frequency.

Another type of extrapolation is given by the equations

$$R(\omega) = R_b \left(\frac{\omega_b}{\omega}\right)^s \qquad (\omega_c > \omega > \omega_b) \tag{23}$$

and

$$R(\omega) = R_c \left(\frac{\omega_c}{\omega}\right)^4 \qquad (\omega > \omega_c) \quad . \tag{24}$$

In this case, the high frequency extrapolation is divided into two regions. In the low frequency region, the reflectance is assumed to vary as ω^{-s} to simulate interband transitions. In the high frequency region, the reflectance is allowed to vary as ω^{-4}, which is the asymptotic limit for free electrons. By requiring continuity in the reflectance between these two regions, and continuity with the measured reflectance at ω_b, the parameters R_b and R_c are specified. The parameter s is chosen to make the derivatives of the reflectance equal at ω_c. This leaves ω_c as an adjustable parameter, which is again chosen to give agreement with the dielectric function measured independently at one frequency. It should be noted that while both of these extrapolations are useful, neither can be truly justified a priori.

An extrapolation procedure must also be used between zero frequency and the lowest frequency at which data has been measured, ω_a. This extrapolation is only over a finite frequency range and therefore has a smaller effect upon the Kramers-Kronig analysis. For metals, one method which is sometimes employed is to extrapolate the reflectance linearly from ω_a to unit reflectance at zero frequency. Occasionally sizable errors can result from this method.

A better low frequency extrapolation procedure makes use of the Hagen-Rubens relation[5] for the reflectance of metals at low frequencies,

$$R(\omega) = 1 - \alpha\omega^{1/2} \tag{25}$$

where

$$\alpha^2 = 2/(\pi\sigma_{dc}) \quad . \tag{26}$$

If the dc conductivity of the material is known, then α may be calculated so that the low frequency reflectance extrapolation is determined without adjustable parameters. However, this equation does not guarantee continuity in the reflectance or the first derivative of the reflectance with the measured data at ω_a. We can assure continuity by expanding the low frequency reflectance to higher order terms in the frequency, and by adjusting the coefficients of these terms to make the extrapolated reflectance fit smoothly with the data. There is no unique expansion for all metals at low frequencies, but for Drude metals the next two terms in the expansion are proportional to $\omega^{3/2}$ and $\omega^{5/2}$. This reflectance expansion provides a convenient method for assuring continuity with the measured data and for including the information about the dc conductivity into the Kramers-Kronig analysis.

We now consider several of the common models applied to the analysis of the dielectric functions of solids, including models applied to carriers condensed into CDW's.

1) Drude model:

The Drude model for metals considers free carriers with a phenomenological effective mass m* and a phenomenological relaxation or scattering time τ. For this model, the dielectric function is given by the equations[6]

$$\epsilon_1(\omega) = \epsilon_\infty - \frac{\omega_p^2\tau^2}{1 + (\omega\tau)^2} \tag{27}$$

and

$$\epsilon_2(\omega) = \frac{\omega_p^2\tau}{\omega[1 + (\omega\tau)^2]} \quad . \tag{28}$$

This model has been used to analyze the reflectances of many metals, including the organic quasi-one-dimensional metals. By fitting a Drude reflectance to an experimentally measured reflectance, estimates of several physical quantities, including the plasma frequency, the relaxation time, and the background dielectric constant, ϵ_∞, can be obtained. The extrapolated value for the dc conductivity from the Drude function fit is given by:

$$\sigma_{opt}(\omega\rightarrow 0) = \frac{\omega_p^2\tau}{4\pi} \tag{29}$$

which can be compared to the experimentally measured value for the dc conductivity. The reflectance edge for a Drude metal occurs at the frequency where $\epsilon_1(\omega)$ is zero, which is

$$\omega_o = \sqrt{\frac{\omega_p^2}{\epsilon_\infty} - \frac{1}{\tau^2}} \quad . \tag{30}$$

The plasma frequency obtained from the Drude fit, together with the carrier concentration, can be used in Eq. (28) to obtain a value for the carrier effective mass. The effective mass can in turn be used in the tight-binding model to estimate bandwidths and transfer integrals. The bandwidth in one-dimension is given by[7]

$$4t = \frac{2\hbar^2}{m^* d} \tag{31}$$

where d is the distance between neighboring tight-binding sites, for example the intermolecular stacking distance in the quasi-one-dimensional organic compounds, and t is the transfer or overlap integral, i.e. the energy for the carrier to transfer from one site to the next.

2) Lorentz oscillator model:

The Lorentz model describes harmonically bound, damped charges. It can be used for modelling phonons in the absence of electron-phonon interactions. The dielectric function for a Lorentz oscillator is

$$\varepsilon_1(\omega) = 1 + \frac{\omega_p^2(\omega_0^2-\omega^2)\tau^4}{\tau^4(\omega_0^2-\omega^2)^2 + (\omega\tau)^2} \tag{32}$$

and

$$\varepsilon_2(\omega) = \frac{\omega_p^2\omega\tau^3}{\tau^4(\omega_0^2-\omega^2)^2 + (\omega\tau)^2} \quad . \tag{33}$$

In these equations, ω_p^2 is a measure of the oscillator strength in the mode, ω_0 is the resonant frequency of the mode, and τ is a phenomenological relaxation time for the mode.

In the classical model of CDW transport,[8] the frequency dependence of the conductivity of the CDW pinned mode is modelled by a Lorentz oscillator. The oscillator strength in the mode is given by

$$\omega_p^2 = \frac{4\pi n_c e^2}{M_F} \tag{34}$$

where M_F is the effective mass of the CDW per carrier condensed in the CDW, and n_c is the concentration of carriers condensed in the CDW. The total oscillator strength of the carriers condensed in the CDW, however, is given by

$$\Omega_p^2 = \frac{4\pi n_c e^2}{m^*} \tag{35}$$

and hence the fraction of the oscillator strength of the condensed carriers which appears in the CDW pinned mode is just m^*/M_F, in the classical model of CDW transport.

3) Photon assisted tunneling:

In the tunneling model of CDW transport,[9] the frequency dependence of the conductivity of the CDW pinned mode is calculated by means of the theory of photon-assisted tunneling in superconductor-insulator-superconductor (SIS) tunnel junctions.[10] This theory predicts a direct scaling between the frequency and field dependence of the conductivity,

$$\sigma(\frac{\omega}{\omega_T}) = \sigma_{dc} \ (\frac{E}{E_T}) \tag{36}$$

where E_T is the threshold field required to depin the CDW's, and ω_T is the threshold frequency, which is related to the pinning energy gap by the equation $\varepsilon_g = \hbar\omega_T$. The frequency dependence of the conductivity of the condensed carriers predicted by the tunneling model is given by the equation

$$\sigma_1(\omega) = \sigma_\infty(1 - \frac{\omega_T}{\omega}) \ \exp(\frac{-\omega_T}{\omega}) \quad . \tag{37}$$

4) CDW energy gap, single-particle continuum, and phase phonons:

The oscillator strength of the carriers condensed in a CDW can appear in an interband contribution above the CDW energy gap and in coupled CDW carrier-optical phonon modes called phase phonons, as well as the CDW pinned mode.[11,12] When all of the oscillator strength of the condensed carriers appears in the single-particle continuum above the energy gap, the frequency dependence of the conductivity and the dielectric function is

$$\sigma_1(\omega) = \begin{cases} 0 & (\omega < 2\ \Delta) \qquad (38) \\ \dfrac{\omega_p^2(2\Delta)^2}{8\omega^2} \ \dfrac{1}{\sqrt{\omega^2-(2\Delta)^2}} & (\omega > 2\Delta) \qquad (39) \end{cases} ,$$

and

$$\epsilon_1(\omega) = \begin{cases} 1 - \dfrac{\omega_p^2}{\omega^2} + \dfrac{\omega_p^2(2\Delta)^2}{\omega^3\sqrt{(2\Delta)^2-\omega^2}} \sin^{-1}\left(\dfrac{\omega}{2\Delta}\right) & (\omega < 2\Delta) \qquad (40) \\ 1 - \dfrac{\omega_p^2}{\omega^2} + \dfrac{\omega_p^2(2\Delta)^2}{2\omega^3\sqrt{\omega^2-(2\Delta)^2}} \ln\left[\dfrac{1 - \sqrt{1-(2\Delta)^2/\omega^2}}{1 + \sqrt{1-(2\Delta)^2/\omega^2}}\right] & (\omega > 2\Delta) \quad . \qquad (41) \end{cases}$$

When the oscillator strength of the condensed carriers appears in phase phonons in addition to the single-particle continuum, the equations are more complicated. Defining

$$f\left(\frac{\omega}{2\Delta}\right) = \begin{cases} \dfrac{(2\Delta)^2}{\omega^2 y'} \sin^{-1}\left(\dfrac{\omega}{2\Delta}\right) & (\omega < 2\Delta) \qquad (42) \\ \dfrac{(2\Delta)^2}{2\omega^2 y}\left[\pi i + \ln\left(\dfrac{1-y}{1+y}\right)\right] & (\omega > 2\Delta) \qquad (43) \end{cases}$$

$$y = \sqrt{1 - \left(\frac{2\Delta}{\omega}\right)^2} \qquad \text{and} \qquad y' = \sqrt{\left(\frac{2\Delta}{\omega}\right)^2 - 1} \qquad (44)$$

the complex conductivity is given by

$$\sigma(\omega) = \frac{\omega_p^2}{i4\pi\omega}\left\{\frac{f\left(\frac{\omega}{2\Delta}\right)}{1+\lambda\left(\frac{\omega}{2\Delta}\right)^2\left[\frac{1}{\frac{1}{D_0}+1-\frac{V}{\Delta}}\right]f\left(\frac{\omega}{2\Delta}\right)} - 1\right\} \qquad (45)$$

where

$$D_0 = \frac{1}{\lambda}\sum_n \frac{\lambda_n\omega_n^2}{\omega^2-\omega_n^2 + i\omega\omega_{rn}} \qquad (46)$$

and $\lambda = \sum_n \lambda_n$. The λ_n are the dimensionless electron-phonon coupling constants, the ω_n are the resonant frequencies of the bare phonons, and the ω_{rn} are the relaxation frequencies of the bare phonons. The potential V represents the mganitude of an external periodic potential with the wavelength of the CDW. There is no such external potential in $NbSe_3$, and so V is zero when using these equations to model the conductivity of $NbSe_3$. In the organic charge transfer salts, the presence of a donor or acceptor chain (e.g. the anion chains in the TMTSF salts) can give rise to a periodic potential in the lattice, which can be modelled by giving a finite value to V.

The oscillator strength in the CDW pinned mode can be included in this model by treating it as a low frequency phase phonon. When V = 0 in these equations, the peak conductivity of the lowest frequency phase phonon (i.e. the CDW pinned mode) is at zero frequency, rather than at a finite pinning frequency. This is an inadequacy of treating the pinned mode as a phase phonon in these equations. For modeling the conductivity in the FIR of $NbSe_3$, these equations are entirely adequate, though, because the difference between the pinning frequency and dc is negligible at FIR frequencies. The conductivity of the pinned mode at high frequencies relaxes approximately as $(\omega\tau)^{-2}$, as expected for a pinned mode which can be modelled by a Lorentzian oscillator. The fraction of the oscillator strength in the pinned mode is determined by the electron-phonon coupling constant, λ, the bare frequency of the acoustic phonon at $2k_F$, ω_0, and the size of the CDW energy gap, 2Δ, according to the relation

$$\frac{m^*}{M_F} = \frac{1}{1 + \frac{(2\Delta)^2}{\lambda \omega_Q^2}} . \qquad (47)$$

References

1. J. D. Jackson, Classical Electrodynamics (John Wiley and Sons, Inc., NY, 1975) 280-2.
2. F. Wooten, Optical Properties of Solids (Academic Press, NY, 1972) Chp. 6.
3. M. Tinkham, R. A. Ferrell, Phys. Rev. Lett. 2, 331 (1959).
4. F. Stern, Sol. St. Phys. 15, 299 (1963).
5. E. Hagen, H. Rubens, Ann. Physik 11, 873 (1903).
6. J. M. Ziman, Principles of the Theory of Solids (Cambridge Univ. Press, Cambridge, 1972) 280-1.
7. C. Kittel, Introduction to Solid State Physics (John Wiley and Sons, Inc., NY, 1976) 260-3.
8. G. Grüner, Mol. Crys. Liq. Crys. 81, 735 (1982).
9. J. Bardeen, Mol. Crys. Liq. Crys. 81, 1 (1982).
10. J. R. Tucker, IEEE J. Qu. Elec. QE-15 No. 11, 1234 (1979).
11 P. A. Lee, T. M. Rice, P. W. Anderson, Sol. St. Comm. 14, 703 (1974).
12. M. J. Rice, Phys. Rev. Lett. 37 No. 1, 36 (1976).

Appendix B. Group Theory

In this section we present the group theoretical analysis of the phonon modes in $NbSe_3$ and $(TMTSF)_2ClO_4$ and discuss the symmetry requirements for first-order coupling between phonons and conduction electrons in a metal.

A. $NbSe_3$

In the undistorted state, $NbSe_3$ has a space group symmetry of C_{2h}^2 ($P2_1/m$). This includes a two-fold screw axis along the fiber axis, a mirror plane perpendicular to the fiber axis, and two centers of inversion symmetry in the unit cell. The corresponding point group is C_{2h} with a character table given below.

C_{2h}		E	C_2	σ_h	i
x^2,y^2,z^2,xy	A_g	1	1	1	1
z	A_u	1	1	-1	-1
xy,yz	B_g	1	-1	-1	1
x,y	B_u	1	-1	1	-1

A straightforward procedure can be used to determine the optical activity of the phonons.[1] If there are n atoms in the unit cell, then there are 3n degrees of freedom which can be defined either by the 3n normal coordinates Q_1, Q_2, ... Q_{3n} or by the 3n Cartesian

coordinates $x_1,y_1,z_1,\ldots,x_n,y_n,z_n$. The coordinates x_r,y_r,z_r of the r'th particle are chosen as the displaced position of the particle with respect to its equilibrium position, with the axes $\hat{x}$, $\hat{y}$, $\hat{z}$ chosen parallel to a defined $\hat{X}$, $\hat{Y}$, $\hat{Z}$ system. The 3n normal mode coordinates define a representation Γ of the point group. Because the normal mode coordinates are simply linear functions of the 3n Cartesian coordinates, the Cartesian coordinates also define an equivalent representation Γ' of the point group. The character of any operation R in the two representations is the same. It is simplest, however, to calculate the characters of the symmetry operations for the reducible representation Γ' defined by the Cartesian coordinates.

When the symmetry operation R takes a particle k into the position of a nonequivalent particle 1, the general relation is

$$R \cdot x_k = a \cdot x_1 + b \cdot y_1 + c \cdot z_1. \tag{1}$$

There are no on-diagonal elements in this transformation and thus the character is zero. If R takes particle k into an equivalent site, however, the transformation relations are

$$R \cdot x_k = x_k \cos\phi_R - y_k \sin\phi_R \tag{2}$$

$$R \cdot y_k = x_k \sin\phi_R + y_k \cos\phi_R \tag{3}$$

and

$$R \cdot z_k = \pm z_k . \tag{4}$$

The ± sign in the last equation is determined by the type of rotation, + for a proper rotation, and - for an improper rotation. ϕ_R is the angle of rotation associated with R. For this case, there are on-diagonal elements in the transformation matrix, and so the character is

$$\chi = \pm 1 + 2\cos\phi_r . \tag{5}$$

If N particles are rotated into equivalent positions by R then the total character associated with R in Γ and Γ' is

$$\chi(R) = N(\pm 1 + 2\cos\phi_R) \quad . \tag{6}$$

In a similar way, the character associated with normal mode coordinates of translations of the entire point system are found by

$$R \cdot X = X \cos\phi_R - Y \sin\phi_R \tag{7}$$

$$R \cdot Y = X \sin\phi_R + Y \cos\phi_R \tag{8}$$

$$R \cdot Z = \pm Z, \tag{9}$$

to be

$$\chi_T(R) = \pm 1 + 2\cos\phi_R. \tag{10}$$

For rotations, the character is given by

$$\chi_R(R) = 1 \pm 2\cos\phi_R. \tag{11}$$

The next step is to apply each symmetry operation to the $NbSe_3$ unit cell (see Fig. 53) and determine how many atoms are moved to equivalent positions. When the C_2 (rotation by π) and the i (inversion) operators are applied, none of the atoms in the unit cell return to equivalent positions. The σ_h (reflection) operator, however, returns all 24 atoms to equivalent positions. Applying Eqs. (6), (10), and (11), we find the following character table.

R	N	ϕ_R	$\chi(R)$	$\chi_T(R)$	$\chi_R(R)$
E	24	0	72	3	3
C_2	0	π	0	-1	-1
σ_h	24	0	24	1	-1
$i=C_2\ \sigma_h$	0	π	0	-3	3

The character table for the C_{2h} point group is now used to divide these reducible representations into their irreducible representations, by means of the formula

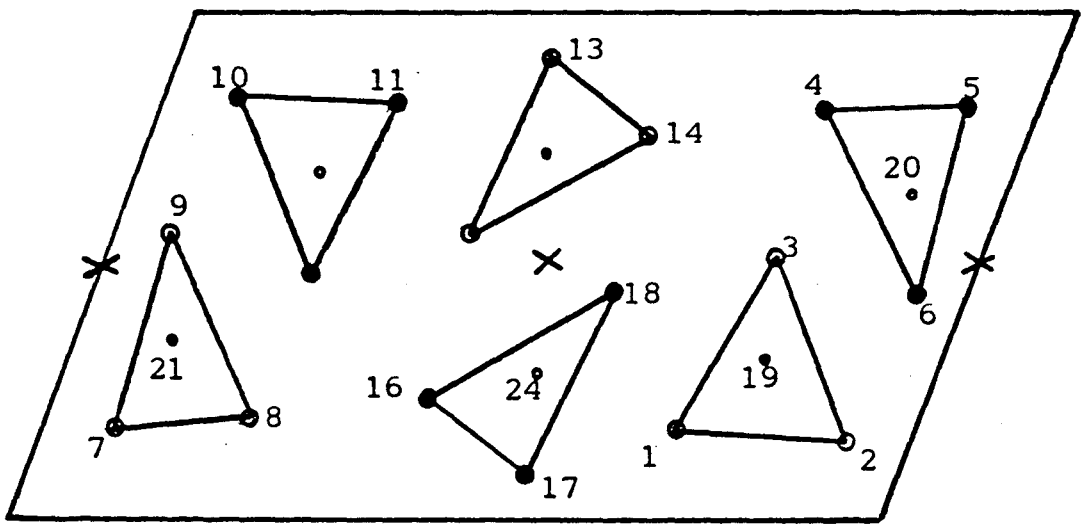

Fig. 53. Unit cell of $NbSe_3$ crystal with the atom sites numbered for the group theory analysis. The x's mark centers of inversion symmetry.

$$n_i = \frac{1}{G} \sum_i h\chi(R)\chi_i(R) \quad . \tag{12}$$

Here G is the order of the group, $\chi_i(R)$ is the character of the i^{th} irreducible representation of the group, and h is the order of the class R in the point group. The results are

$$\Gamma = 24\ A_g + 12\ A_u + 12\ B_g + 24\ B_u, \tag{13}$$

and

$$\Gamma_T = A_u + 2\ B_u \tag{14}$$

$$\Gamma_R = A_g + 2\ B_g. \tag{15}$$

The symmetry of each normal coordinate determines its potential for IR or Raman activity. Those coordinates with the symmetry of the dipole operator (x, y, or z) will be IR-active. Those which transform like x^2, y^2, z^2, xy, xz, or yz will be Raman-active. In crystals which include inversion symmetry, like $NbSe_3$, IR and Raman activity are always mutually exclusive. It can be seen from the character table of the C_{2h} point group, that the A_g and B_g modes are potentially Raman-active, while the A_u and B_u modes are potentially IR-active. One A_u mode and two B_u modes are associated with translations (acoustic phonons) and are not IR-active optical modes. This leaves 36 Raman-active modes and 33 IR-active modes in the undistorted $NbSe_3$ crystal.

The polarization activity of these modes is also immediately determined from the character table. The 11 A_u optical modes transform like the z coordinate, and are therefore IR-active for light polarized parallel to the z-axis, i.e. the fiber axis in $NbSe_3$. The 22 B_u modes which are IR-active transform like x and/or y, and are therefore active for light polarized transverse to the fiber axis.

Polarization information can also be obtained from the normal mode coordinates of the phonon modes, if these are known. However, calculation of the normal mode coodinates for a crystal requires detailed knowledge of the interatomic forces, and is in general very difficult. Much of the vibrational information can be obtained much more easily through calculation of the symmetry mode coordinates. The normal mode coordinates are obtained from linear combinations of the symmetry mode coordinates using the interatomic force constants.

A unit cell of $NbSe_3$ with the lattice sites numbered is shown in Fig. 53. A general expression for a normal mode coordinate is

$$R = a_1x_1 + b_1y_1 + c_1z_1 + \ldots + a_{24}x_{24} + b_{24}y_{24} + c_{24}z_{24}.$$

Applying the symmetry operations to the Cartesian coordinates gives the set of relations:

$$C_2 \cdot x_1 = -x_{11} \qquad C_2 \cdot y_1 = -y_{11} \qquad C_2 \cdot z_n = z_n$$

$$C_2 \cdot x_2 = -x_{10} \qquad C_2 \cdot y_2 = -y_{10}$$

$$C_2 \cdot x_3 = -x_{12} \qquad C_2 \cdot y_3 = -y_{12}$$

$$\vdots \qquad\qquad \vdots$$

and

$$\sigma_h \cdot x_n = x_n \qquad \sigma_h \cdot y_n = y_n \qquad \sigma_h \cdot z_n = -z_n .$$

The character of all symmetry operations of the A_g representation is one, so

$$C_2 \cdot R = 1 \cdot R$$

$$\sigma_h \cdot R = 1 \cdot R$$

$$i \cdot R = 1 \cdot R .$$

In order for $C_2 \cdot R = R$, however, we must have

$$a_1 = -a_{11} \qquad a_2 = -a_{10} \qquad a_3 = -a_{12} \qquad a_4 = -a_8 \qquad \ldots.$$

$$b_1 = -b_{11} \qquad b_2 = -b_{10} \qquad b_3 = -b_{12} \qquad b_4 = -b_8 \qquad \ldots.$$

$$c_1 = c_{11} \qquad c_2 = c_{10} \qquad c_3 = c_{12} \qquad c_4 = c_8 \qquad \ldots.$$

Similarly, for $\sigma_h \cdot R = R$, we must have

$$c_1 = -c_1 \qquad c_2 = -c_2 \qquad c_3 = -c_3 \qquad c_4 = -c_4 \qquad \ldots.$$

Therefore all the c's must be zero. Hence all phonons with A_g symmetry must vibrate in the xy plane, perpendicular to the fiber axis. No new information is obtained from the third relation, $i \cdot R = 1 \cdot R$.

The symmetry mode coordinates are

$$S_1 = x_1 - x_{11} \qquad S_2 = x_2 - x_{10} \qquad S_3 = x_3 - x_{12} \qquad S_4 = x_4 - x_8$$

$$S_5 = x_5 - x_9 \qquad S_6 = x_6 - x_7 \qquad S_7 = x_{13} - x_{17} \qquad S_8 = x_{14} - x_{16}$$

$$S_9 = x_{15} - x_{18} \qquad S_{10} = x_{19} - x_{22} \qquad S_{11} = x_{20} - x_{21} \qquad S_{12} = x_{23} - x_{24}$$

$$T_1 = y_1 - y_{11} \qquad T_2 = y_2 - y_{10} \qquad T_3 = y_3 - y_{12} \qquad T_4 = y_4 - y_8 \ \ldots.$$

In terms of these symmetry mode coodinates, the A_g normal mode coordinates can be written as

$$R = a_1 S_1 + a_2 S_2 + a_3 S_3 + a_4 S_4 + a_5 S_5 + a_6 S_6 + a_{13} S_7 + a_{14} S_8 + a_{15} S_9 +$$

$$a_{19} S_{10} + a_{20} S_{11} + a_{23} S_{12} + b_1 T_1 + b_2 T_2 + b_3 T_3 + \ldots.$$

For the other representations, we have

B_g:	A_u:	B_u:
$C_2 \cdot R = -R$	$C_2 \cdot R = -R$	$C_2 \cdot R = -R$
$\sigma_h \cdot R = -R$	$\sigma_h \cdot R = R$	$\sigma_h \cdot R = R$
$i \cdot R = R$	$i \cdot R = -R$	$i \cdot R = -R$.

Following the same procedure to obtain the symmetry mode coordinates for each representation, we find that the B_g and A_u modes correspond to vibrations entirely along the z-axis (the fiber axis), and the B_u modes correspond to vibrations in the xy plane (perpendicular to the fiber axis).

An alternate approach to determination of the phonon activity of a crystal structure, often found in the literature,[2] is the correlation method. In this method the symmetry of the individual lattice sites is considered, in addition to the symmetry of the unit cell as a whole. For $NbSe_3$, all 24 atoms in the unit cell are at sites of C_{1h} symmetry, but because of the inversion symmetry there are only twelve inequivalent sites.

The correlation method is so named, because it correlates the modes possible from the site symmetry with the modes of the point group of the crystal. This is done conveniently by use of the character tables. The C_{1h} character table and the appropriate part of the C_{2h} character table are shown below.

C_{1h}	E	σ_h
A'	1	1
A"	1	-1
χ_T	3	1

C_{2h}	E	σ_h
A_g	1	1
A_u	1	-1
B_g	1	-1
B_u	1	1

The irreducible representations for the modes at each site of C_{1h} symmetry are $\Gamma_T = 2A' + A''$. The correlation diagram is thus

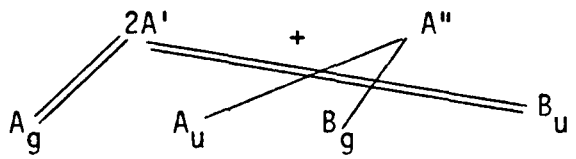

as determined by comparison with the character tables. The total representation for the $NbSe_3$ crystal is found by multiplying this result by the twelve inequivalent C_{1h} sites in the unit cell. This gives

$$\Gamma = 24A_g + 12A_u + 12B_g + 24B_u.$$

This is the same result as was obtained previously.

Group theory can also be used to predict which optical phonons will have the correct symmetry to interact in first-order with the conduction electrons in the crystal. Such an interaction can give rise to CDW-optical phonon coupled modes, for example, which are anomalously IR-active with oscillator strengths that are electronic in origin.[3]

The first-order, linear interaction term between the electrons and phonons may be written as[4]

$$\mathcal{H}_{linear} = \sum_{\gamma} C_{\gamma}^{+} C_{\gamma} \langle \gamma | Q_i \frac{\partial \mathcal{H}_{el}}{\partial Q_i} | \gamma \rangle \quad . \tag{16}$$

The C_{γ}^{+} and C_{γ} are the usual electronic creation and annihilation operators for the electronic orbital γ, Q_i is a dimensionless phonon normal mode coordinate, and $_{el}$ is the one-electron Hamiltonian,

$$\mathcal{H}_{el} = \sum_{\gamma} \epsilon_{\gamma} C_{\gamma}^{+} C_{\gamma} . \tag{17}$$

The Q_i transform according to the irreducible representation Γ_i of the vibrational mode i. The $\partial \mathcal{H}_{el}/\partial Q_i$ will transform similarly, as will the product $Q_i \, \partial \mathcal{H}_{el}/\partial Q_i$. If the irreducible representation for the transformation properties of the electronic state γ is defined as Γ_{γ}, then in order for the linear Hamiltonian (16) to be nonzero, the irreducible representation Γ_{γ} must be contained in the direct product of Γ_i and Γ_{γ},

$$\Gamma_{\gamma} \subset \Gamma_{\gamma} \times \Gamma_i \quad . \tag{18}$$

In particular, if all the irreducible representations of the crystal point group are one-dimensional (as in $NbSe_3$), then the only possibility for nonzero $\mathcal{H}_{linear}$ is when Γ_i is the totally symmetric A_g representation of the crystal point group.

B. $\underline{(TMTSF)_2ClO_4}$

The analysis of phonon modes in the organic molecular crystals by group theory is approached somewhat differently than for inorganic ionic/covalent crystals. In the organic linear chain compounds, the crystal vibrations may be classified as 1) longitudinal or transverse translations (acoustic modes), 2) intermolecular vibrations and librations (rigid vibrations and rotations of the molecular units), and 3) intramolecular vibrations (internal distortions in the length and/or angle of the bonds in the molecular units). Such a classification is possible because the intramolecular bonds are much stronger than the intermolecular bonds.

At room temperature, $(TMTSF)_2ClO_4$ crystallizes with very low (triclinic) symmetry with a space group[5] of $P\bar{1}$ (C_i^1). The inversion center occurs at the anion site, but is present on average only. There are two TMTSF molecules and one ClO_4 anion per unit cell, for a total of 57 atoms. Therefore, in addition to the three acoustic modes, there are 168 optical modes. The optical phonons can be grouped into intermolecular vibrations, intramolecular vibrations, and librations in the following way. First we consider the unit cell of two TMTSF units and one ClO_4 unit to be composed of rigid point bodies. In addition to the three acoustic modes of this system, there will be six optical modes, which correspond to intermolecular vibrations. Considering the spatial extent of the TMTSF units, we find six additional modes which are librations, because of the three rotational degrees of freedom of each unit. The ClO_4 anion will

have an additional 12 internal vibrational degrees of freedom, and these are expected[6] to occur at frequencies above 600 cm^{-1}. This gives a total of 24 optical phonon modes, leaving 144 optical phonons which are internal vibrations of the TMTSF units, or 72 per unit.

The intramolecular vibrations of the TMTSF molecule can be analyzed in the following manner. We begin with the assumption that the TMTSF molecule is planar (in reality there is a 1.2° deviation from planarity[7]) and that four of the methyl hydrogen atoms lie in the molecular plane (see Fig. 54a). The symmetry of this unit is D_{2h}, and the character table of the point group is

D_{2h}	E	C_{2z}	C_{2y}	C_{2x}	σz	σy	σx	i
A_g	1	1	1	1	1	1	1	1
B_{1g}	1	1	-1	-1	1	-1	-1	1
B_{2g}	1	-1	1	-1	-1	1	-1	1
B_{3g}	1	-1	-1	1	-1	-1	1	1
A_u	1	1	1	1	-1	-1	-1	-1
B_{1u}	1	1	-1	-1	-1	1	1	-1
B_{2u}	1	-1	1	-1	1	-1	1	-1
B_{3u}	1	-1	-1	1	1	1	-1	-1

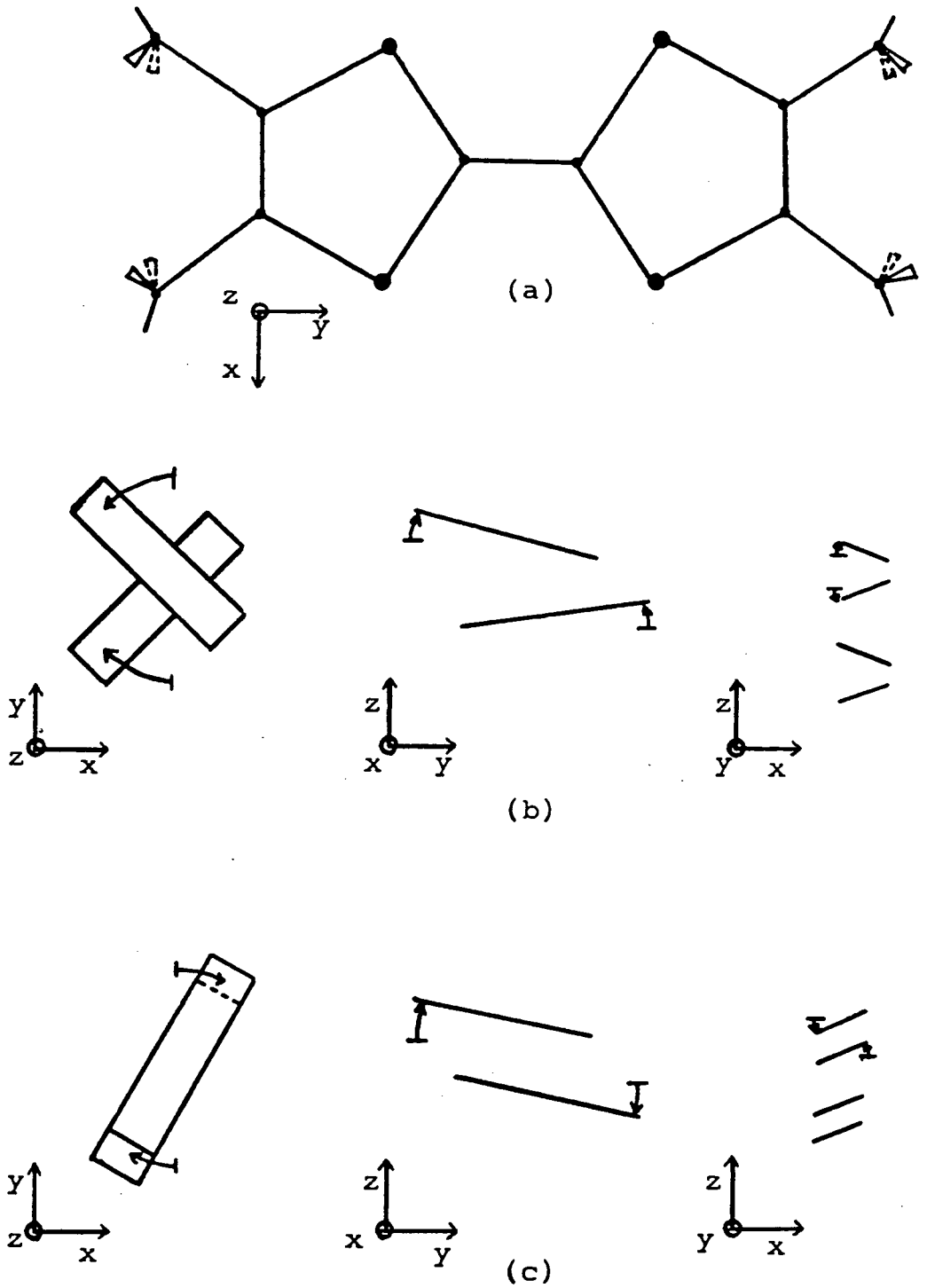

Fig. 54. (a) TMTSF molecule showing positions of methyl hydrogens used for group theory analysis, (b) librational modes which do not preserve symmetry, (c) rotational modes which do preserve symmetry.

	E	C_{2z}	C_{2y}	C_{2x}	σ_z	σ_y	σ_x	i
$\chi_R=1\pm2\cos\phi_R$	3	-1	-1	-1	-1	-1	-1	3
$\chi_T=\pm1+2\cos\phi_T$	3	-1	-1	-1	1	1	1	-3
N	20	0	0	4	20	4	0	0
$N\chi_T$	60	0	0	-4	20	4	0	0

Therefore, the representation of the acoustic modes is

$$\Gamma_T = B_{1u} + B_{2u} + B_{3u}$$

and of the librational modes is

$$\Gamma_R = B_{1g} + B_{2g} + B_{3g}$$

which leaves, for the 72 intramolecular vibrations, a representation of

$$\Gamma = 12A_g + 11B_{1g} + 7B_{2g} + 6B_{3g} + 7A_u + 7B_{1u} + 11B_{2u} + 11B_{3u}.$$

There are 12 modes with A_g symmetry which may potentially couple to the electrons and thereby give rise to anomalously IR-active modes.

The positions of the methyl hydrogen atoms are not known,[7] however, and some of the A_g modes deduced above are a result of degrees of freedom associated with these atoms. Because of the light

mass of the hydrogen atoms, we expect these modes to occur at relatively high frequencies. By repeating the same procedure for the TMTSF molecule just described, but neglecting the hydrogen atoms, we can determine how many of the A_g modes are associated with the hydrogen atoms. The resulting representation of the intramolecular vibrations is

$$\Gamma = 7A_g + 6B_{1g} + 3B_{2g} + 2B_{3g} + 3A_u + 3B_{1u} + 6B_{2u} + 6B_{3u}.$$

Thus, only seven of the twelve A_g modes are not associated with the degrees of freedom of the methyl hydrogens. This may be compared to the ten A_g modes determined for the TCNQ intramolecular vibrations,[8] which have vibrational frequencies between 100 and 3000 cm^{-1}.

It is also interesting to consider the symmetry of the librational modes, to see if first-order coupling with the conduction electrons is possible. The point group operations of a single TMTSF chain include i, C_{2x}, and σ_x. For the crystal as a whole, however, only the inversion symmetry operation is present. It can be seen from Fig. 54b that three librational modes destroy the inversion symmetry, and therefore cannot be totally symmetric A_g modes. No first-order coupling is possible between these librational modes and the conduction electrons.

On the other hand, the rotational modes shown in Fig. 54c do not destroy the inversion symmetry of the chain, and only one of the rotational modes destoys the rotational and reflection symmetries of the chain. A first-order coupling is possible between these modes and the conduction electrons.

References

1. S. Bhagavantum, T. Venkatarayudu, Theory of Groups and its Application to Physical Problems (Academic Press, NY, 1969).

2. J. A. Holy, K. C. Woo, M. V. Klein, F. C. Brown, Phys. Rev. B16, No. 8, 3628 (1977).

3. M. J. Rice, Phys. Rev. Lett. 37 No. 1, 36 (1976).

4. N. O. Lipari, C. B. Duke, L. Pietronero, J. Chem. Phys. 65 No. 3, 1165 (1976).

5. R. Moret, J. P. Pouget, R. Comes, K. Bechgaard, Phys. Rev. Lett. 49 No. 14, 1008 (1982).

6. G. N. Krynauw, C. J. H. Schutte, Spec. Acta 21, 1947 (1965).

7. N. Thorup, G. Rindorf, H. Soling, K. Bechgaard, Acta Cryst. B37, 1236 (1981).

8. N. O. Lipari, C. B. Duke, R. Bozio, A. Girlando, C. Pecile, A. Padva, Chem. Phys. Lett. 44 No. 2, 236 (1976).

Acknowledgments

The research described in this thesis has been done under the supervision of Professor Paul L. Richards. I am grateful for his many ideas for overcoming various difficulties in these experiments, his help in relating the analysis of the data to other general results of solid state physics, and his patience in proofreading and correcting the many versions of manuscripts and this thesis.

The samples used in this research were provided by P. Monceau, R. L. Greene, and N. P. Ong. I thank them also for many useful conversations. In addition, A.M. Portis, L. M. Falicov, T.H.M. Rasing, J. Bardeen, M. J. Rice, T. Timusk and I. Bozovic provided much helpful insight into the data analysis.

My time at Berkeley has been made more enjoyable in many ways through the interaction with other students in our research group. In particular, Bob Bailey's help with PDP 11/20 computer programming was appreciated. Mark Hueschen and Bob McMurray gave much helpful advice concerning the operation of the magnet rig and other things. Jim Bonomo, Shirley Chiang, and Steve McBride were also of great help on many occasions.

During part of this research I have been supported in part by a graduate fellowship from the National Science Foundation. This work was also supported by the Director, Office of Energy Research, Office of Basic Energy Sciences, Materials Sciences Division of the U.S. Department of Energy under Contract No. DE-AC03-76SF00098.

Finally, I especially thank my wife, Helen, for her long-suffering support during the final stages of this thesis. If there is anyone happier to see the end of this than I, it would surely be her.

TECHNICAL INFORMATION DEPARTMENT
LAWRENCE BERKELEY LABORATORY
UNIVERSITY OF CALIFORNIA
BERKELEY, CALIFORNIA 94720